

Localized CO₂ Corrosion in the Presence of Organic Acids

A thesis presented to
the faculty of
the Russ College of Engineering and Technology of Ohio University

In partial fulfillment
of the requirements for the degree
Master of Science

Vanessa Fajardo Niño de Rivera

March 2011

© 2011 Vanessa Fajardo Niño de Rivera. All Rights Reserved.

This thesis titled
Localized CO₂ Corrosion in the Presence of Organic Acids

by
VANESSA FAJARDO NIÑO DE RIVERA

has been approved for
the Department of Chemical and Biomolecular Engineering
and the Russ College of Engineering and Technology by

Srdjan Nešić

Professor of Chemical and Biomolecular Engineering

Dennis Irwin

Dean, Russ College of Engineering and Technology

ABSTRACT

FAJARDO NIÑO DE RIVERA, VANESSA, M.S., March 2011, Mechanical Engineering. Localized CO₂ Corrosion in the Presence of Organic Acids (115 pp.)

Director of Thesis: Srdjan Nešić

The organic acid content in oil wells plays a determining role in the severity of corrosion even when only small concentrations are present. Organic acids are weak Brønsted acids that exist mainly as undissociated molecular species. Like all weak acids, a certain moiety will dissociate to form hydrogen ions and an anionic conjugate base. Therefore, with these acids the corrosion rate is not influenced only by pH, but also by the concentration of the undissociated acids in the solution. The vast majority of the literature on the effect of organic acids on CO₂ corrosion of carbon steel focuses on acetic acid because this acid is the most abundant in the mixture of organic acids seen in the field. The purpose of this project was to understand and determine the mechanistic role of organic acids on the initiation of localized corrosion.

It was concluded that the presence of acetic acid may lead to damage of the protective iron carbonate scale formed on X65 carbon steel. This leads directly to a temporary increase in the corrosion rate. However, the final corrosion rate does not seem to be affected. This raises the possibility that there may be a different phase conferring protection on the steel surface. This phase (corrosion scale) was characterized using different analytical techniques (SEM, EDS, XRD, XPS and FIB/TEM/EDS) to provide a more complete understanding of the metal's surface. It was found that the protection

persisted as part of the FeCO_3 remained on the surface. No localized attack was found under the studied conditions.

In order to quantify iron carbonate dissolution, the electrochemical quartz crystal microbalance (EQCM) was used for the study of scale solubility in the presence of acetic acid. This confirmed that the presence of acetic acid was responsible for partial removal of the iron carbonate scale by selective dissolution, corroborating the characterization data obtained by surface analysis.

Approved: _____

Srdjan Nešić

Professor of Chemical and Biomolecular Engineering

DEDICATION

Dedicated to the memory of my parents Jorge Fajardo and Concepcion Niño de Rivera.

ACKNOWLEDGMENTS

I would like to express my sincere gratitude to my mentor and friend, Dr. Srdjan Nesic, for the guidance he gave me during the most difficult times of my studies. He never gave up on me and was a constant source of support. I would like to thank Bruce Brown, the project leader, Dr. David Young and Dr. Brian Kinsella, for their enormous contribution to the work. The laboratory technicians, Al Shubert, Danny Cain, John Goettge, Cody Shafer, Phil Bullington and Steve Upton also contributed to the success of the project. The administrative staff of the Institute for Corrosion and Multiphase Technology, Edie Chalfant, Debbie Bullington and Rebecca Gill, helped me fulfill numerous administrative requirements and make the Institute feel like home. I would like to thank the other members of the committee Dr. Hajrudin Pasic, Dr. David Ingram, Dr. David Young, Dr. Frank F. Kraft, for their support and patience during this project.

The different surface analysis techniques were done in the Department of Physics and Astronomy at Ohio University under the supervision and guidance of Dr. Ingram, Dr. Martin Kordesch and Dr. Aurangzeb Khan. The Department of Materials Science and Engineering in CASE Western Reserve University, under Dr. Amir Avishai's supervision, was also instrumental in allowing me to complete this project. In particular, Dr. Kordesch provided me with valuable feedback on the diffraction data analysis.

My family has played an important role in my life and my work. My siblings, Sarai, Mauricio, and Alejandra are the light of my way and inspired me to be the best. Georgina, Concepcion, Jorge and Mauricio's belief in me helped me bring this project to

completion. Finally, my husband Christian Canto, has made my life full of happiness. I love you Christian Canto.

TABLE OF CONTENTS

	Page
Abstract	3
Dedication	5
Acknowledgments	6
List of tables	10
List of figures	11
Chapter 1: Corrosion in oil and gas production system.....	16
1.1 Introduction	16
1.2 Fundamentals of CO ₂ corrosion	17
1.3 CO ₂ corrosion in the presence of organic acids	19
Chapter 2: Non-scale forming conditions in the presence of organic acids	21
2.1 Introduction	21
2.2 Objective	21
2.3 Experimental method	22
2.4 Results and discussion	26
2.4.1 Effect of the total molar concentration for different acids	26
2.4.2 Effect of same undissociated molar concentration at fixed pH	29
2.5 Summary	34
Chapter 3: Integrity of FeCO ₃ layer in the presence of acetic acid	35
3.1 Introduction to FeCO ₃ layer forming conditions	35
3.2 Experimental procedure	36
3.3 Results and discussion	40
3.3.1 Influence of acetic acid concentration	41
3.3.2 Effect of the flow velocity	49
3.3.3 Effect of the pH	52
3.4 Summary	54
Chapter 4: Characterization of the corrosion product layer	55
4.1 Objective	55
4.2 Experimental method	55

4.3	Results and discussion	56
4.4	Summary	69
Chapter 5: Study of the solubility of iron carbonate in the presence of acetic acid using the electrochemical quartz crystal microbalance		70
5.1	Introduction	70
5.2	Objective	71
5.3	Experimental method	71
5.4	Result and discussions	74
5.4.1	Iron carbonate precipitation	74
5.4.2	Iron carbonate dissolution by acetic acid	86
5.4.3	Iron carbonate dissolution by hydrochloric acid	97
5.5	Summary	100
Chapter 6: Conclusions and future work		101
6.1	Conclusions	101
6.2	Future work	102
References		103
APPENDIX I: Characterization of the X65 steel		109
APPENDIX II: Corrosion rate determination [46]		113
APPENDIX III: Surface analysis		115

LIST OF TABLES

	Page
Table 1. Chemical reactions and their equilibrium constants	18
Table 2. Experimental conditions (same total molar concentration at autogenous pH) ...	25
Table 3. Experimental conditions (same undissociated molar concentration at fixed pH)	25
Table 4. Amount of acid to be added in ppm to get 0.03M	26
Table 5. Distribution of species at 0.03M and autogenous pH	27
Table 6. pCO ₂ required to get 0.03M of carbonic acid (H ₂ CO ₃)	30
Table 7. Distribution of species at pH 4 and 0.003M of undissociated acid	30
Table 8. Experimental conditions – iron carbonate precipitation	38
Table 9. Physical and chemical properties of acetic acid [28, 29]	38
Table 10. Acetic acid concentration at pH 6.3 and 80°C	39
Table 11. Acetic acid concentration at different values of pH at 80°C	40
Table 12. Experimental conditions – iron carbonate precipitation	56
Table 13. d–Spacings with $\lambda= 1.54056\text{Å}$ (Source: ©2010 International Centre for Diffraction Data)	61
Table 14. Experimental conditions – Iron carbonate precipitation on polarized (-700mV) platinum coated quartz crystal at different pH values	73
Table 15. Experimental conditions – Iron carbonate dissolution on polarized (-700mV) platinum coated quartz crystal	73
Table 16. Experimental results of the iron carbonate precipitation on polarized (-700mV) platinum coated quartz crystal from Figure 37	75
Table 17. Binding energies for FeCO ₃ [36]	81
Table 18. Experimental conditions – Iron carbonate precipitation at pH 6.0	82
Table 19. Experimental results of the iron carbonate dissolution in the presence of different concentrations of acetic acid	88
Table 20. Chemical composition of X52[39], X65 and X70[40] pipeline steel	109
Table 21. Mechanical properties [41]	109
Table 22. Information provided from diverse analytical techniques	115

LIST OF FIGURES

	Page
Figure 1. Experimental cell design.	22
Figure 2. Schematic design for the new rotating cylinder electrode (RCE).	24
Figure 3. Effect of total molar concentration of different acids on the corrosion rate of X65 steel at autogenous pH after 5 hours of exposure (25°C, 1000rpm, 1 wt.% NaCl, and pCO ₂ =0.98bar).	28
Figure 4. Potentiodynamic sweeps X65 steel (25°C, 1000rpm, 1 wt.% NaCl, and pCO ₂ =0.98bar).	29
Figure 5. Potentiodynamic sweeps for X65 steel (pH 4, 25°C, 1000rpm, 1 wt.% NaCl, pCO ₂ =0.98bar, and [R-COOH] = 0.03M).	31
Figure 6. Potentiodynamic sweeps for X65steel (pH 4, 25°C, 1000rpm, 1 wt.% NaCl, pCO ₂ =0.98bar and [R-COOH] = 0.003M).	32
Figure 7. Potentiodynamic sweeps for X65 steel (pH 4, 25°C, 1000rpm, 1 wt.% NaCl and pCO ₂ =0.98bar).	33
Figure 8. Effect of different acids on the corrosion rate of X65 steel (pH 4, 25°C, 1000rpm, 1 wt.% NaCl, pCO ₂ =0.98bar, and [R-COOH] = 0.003M).	34
Figure 9. Experimental cell design – Iron carbonate layer formation.	36
Figure 10. The effect of 0.8mM of undissociated acetic acid on the corrosion rate and corrosion potential of X65 steel during 168 hours of exposure (3 wt.% NaCl, pH 6.3, pCO ₂ =0.53bar, static conditions and 80°C).	42
Figure 11. The effect of 1.6 mM of undissociated acetic acid on the corrosion rate and corrosion potential of X65 steel during 168 hours of exposure (3 wt.% NaCl, pH 6.3, pCO ₂ =0.53bar, static conditions and 80°C).	42
Figure 12. FeCO ₃ layer morphology of X65 steel (3 wt.% NaCl, pH 6.3, pCO ₂ =0.53bar, static conditions and 80°C). a) layer formed in pure CO ₂ after 96 h and b) layer after addition of 0.8mM of undissociated acetic acid, appearance at the end of the experiment.	44
Figure 13. FeCO ₃ layer morphology of X65 steel (3 wt.% NaCl, pH 6.3, pCO ₂ =0.53bar, static conditions and 80°C). a) layer formed in pure CO ₂ after 96 h and b) layer after	

addition of 1.6mM of undissociated acetic acid, appearance at the end of the experiment.	44
Figure 14. The effect of 1.6 mM of undissociated acetic acid on the corrosion rate and supersaturation during 168 hours of exposure (3% NaCl, pH 6.3, pCO ₂ =0.53bar, stagnant conditions and 80°C).	45
Figure 15. EDX analysis of the a) crystal and b) the exposed substrate after the addition of 1.6mM of undissociated acetic acid at pH 6.3, stagnant conditions and 80°C. Sample taken at the end of the experiment shown in Figure 11 above.....	46
Figure 16. XRD analysis of the layer formed on the steel at pH 6.3, static conditions and 80°C; a) layer formed in pure CO ₂ after 96 h, see Figure 13a above and b) layer after addition of 1.6mM of undissociated acetic acid, at the end of the experiment shown in Figure 13b above.....	48
Figure 17. The effect of flow rate on the corrosion rate and corrosion potential of X65 steel during 168 hours of exposure (3wt.% NaCl, 100 rpm, 0.8mM of undissociated acetic acid, pH 6.3, and 80°C).	50
Figure 18. FeCO ₃ layer morphology of X65 steel (3wt.% NaCl, pH 6.3, 80°C and 100 rpm). a) Layer formed in pure CO ₂ after 67 hours and b) layer after addition of 0.8mM of undissociated acetic acid, appearance at the end of the experiment shown in Figure 17 above.....	50
Figure 19. The effect of flow rate on the corrosion rate and corrosion potential of X65 steel during 168 hours of exposure (3wt.% NaCl, 1000 rpm, 0.8mM of undissociated acetic acid, pH 6.3, pCO ₂ =0.53bar, and 80°C).	51
Figure 20. FeCO ₃ layer morphology of X65 (3wt.% NaCl, pH 6.3, 80°C and 1000 rpm). a) Layer formed in pure CO ₂ after 70 hours and b) layer after addition of 0.8mM of undissociated acetic acid, appearance at the end of the experiment shown in Figure 19 above.....	51
Figure 21. Distribution of species CH ₃ COOH (pK _a 4.86) and CH ₃ COO ⁻ at 80°C.	52
Figure 22. The effect of pH on the corrosion rate and corrosion potential of X65 steel during 168 hours of exposure (3wt.% NaCl, 0.8mM of undissociated acetic acid, pCO ₂ =0.53 bar, static conditions, and 80°C).	53

Figure 23. FeCO ₃ layer morphology of X65 steel (pCO ₂ =0.56 bar, static conditions and 80°C). a) Layer formed in pure CO ₂ after 72 hours and b) layer after addition of 0.8mM of undissociated acetic acid, appearance at the end of the experiment shown in Figure 22 above.	53
Figure 24. EDX analysis before and after the addition of 3mM of undissociated acetic acid (static conditions and 80°C).	57
Figure 25. Unit cells of hematite, siderite and magnetite (a and c= unit cell edges).	59
Figure 26. XRD analysis of possible compounds founds on the steel surface with $\lambda=1.54056 \text{ \AA}$ (Source: ©2010 International Centre for Diffraction Data).	60
Figure 27. XRD analysis of iron carbonate (Source: ©2010 International Centre for Diffraction Data).	62
Figure 28. FIB images of iron carbonate plates formed on X65 mild steel.	63
Figure 29. TEM image and EDS analysis of iron carbonate plates formed on X65 mild steel.	64
Figure 30. TEM image and ED data of the plates found on the X65 mild steel before the addition of undissociated acetic acid.	64
Figure 31. TEM image and EDS analysis of iron carbonate prisms formed on X65 mild steel.	65
Figure 32. TEM image and ED data of the prisms found on the X65 mild steel before the addition of undissociated acetic acid.	65
Figure 33. TEM image and ED data of the prism found on the X65 mild steel after the addition of undissociated acetic acid.	66
Figure 34. FeCO ₃ nanocrystals and ED data.	67
Figure 35. XPS scans of iron carbonate dissolution on X65 steel in the presence of acetic acid (80°C, 0.1wt.% NaCl, and pCO ₂ =0.53 bar).	68
Figure 36. Experimental cell design to measure the solubility of the iron carbonate layer.	72
Figure 37. Iron carbonate precipitation on polarized (-700mV) platinum coated quartz crystal at different pH values (80°C, 0.1wt.% NaCl and pCO ₂ =0.53 bar).	75

Figure 38. SEM image of iron carbonate layer formed on polarized (-700mV) platinum coated quartz crystal at different pH values (80°C, 0.1wt.% NaCl, pCO ₂ =0.53 bar).....	76
Figure 39. EDS analysis of iron carbonate layer formed on polarized (-700mV) platinum coated quartz crystal at different pH values (80°C, 0.1wt.% NaCl, pCO ₂ =0.53 bar).....	77
Figure 40. Raman optical image analysis of the iron carbonate layer formed on polarized (-700mV) platinum coated quartz crystal at different pH values (80°C, 0.1wt.% NaCl, and pCO ₂ =0.53 bar).	78
Figure 41. Raman spectra of the iron carbonate layer formed on polarized (-700mV) platinum coated quartz crystal at different pH values (80°C, 0.1wt.% NaCl, pCO ₂ =0.53 bar).	79
Figure 42. XPS scans of iron carbonate scale formed on polarized (-700mV) platinum coated quartz crystal at different pH values (80°C, 0.1wt.% NaCl, and pCO ₂ =0.53 bar)	80
Figure 43. Reproducibility of the Iron carbonate precipitation on polarized (-700mV) platinum coated quartz crystal at pH 6.0, 80°C, 0.1wt.% NaCl, and pCO ₂ =0.53 bar.	83
Figure 44. SEM image of iron carbonate layer formed on polarized (-700mV) platinum coated quartz crystal at pH 6.0, 80°C, 0.1wt.% NaCl, and pCO ₂ =0.53 bar.....	84
Figure 45. EDS analysis of iron carbonate layer formed on polarized (-700mV) platinum coated quartz crystal at pH 6.0, 80°C, 0.1wt.% NaCl, and pCO ₂ =0.53 bar.....	85
Figure 46. Iron carbonate precipitation-dissolution on polarized (-700mV) platinum coated quartz crystal at different undissociated acetic acid concentrations (80°C, 0.1wt.% NaCl, pCO ₂ =0.53 bar).	87
Figure 47. SEM image of iron carbonate dissolution due to the presence of acetic acid (pH 6.0, 80°C, 0.1wt.% NaCl, and pCO ₂ =0.53 bar).	90
Figure 48. SEM image of iron carbonate precipitation and dissolution (pH 6.0, 80°C, 0.1wt.% NaCl, and pCO ₂ =0.53 bar).	91
Figure 49. Iron carbonate precipitation on polarized (-700mV) platinum coated quartz crystal (3mM of undissociated acetic acid at 80°C, 0.1wt.% NaCl, and pCO ₂ =0.52 bar).	92

Figure 50. EDS analysis of iron carbonate layer formed on polarized (-700mV) platinum coated quartz crystal at pH 6.0, 80°C, 0.1wt.% NaCl, pCO ₂ =0.53 bar and 3mM of undissociated acetic acid.....	93
Figure 51. Raman spectra and optical image of the iron carbonate layer formed on polarized (-700mV) platinum coated quartz crystal at 80°C, 0.1wt.% NaCl, pCO ₂ =0.53 bar and 3mM of undissociated acetic acid.....	94
Figure 52. XPS scans of iron carbonate dissolution on polarized (-700mV) platinum coated quartz crystal in the presence of acetic acid (80°C, 0.1wt.% NaCl, and pCO ₂ =0.53 bar).....	96
Figure 53. TEM image and EDS analysis of iron carbonate plates formed on polarized (-700mV) platinum coated quartz crystal in the presence of 3mM of undissociated acetic acid (80°C, 0.1wt.% NaCl, and pCO ₂ =0.53 bar).....	97
Figure 54. TEM image and ED data of the prisms found on polarized (-700mV) platinum coated quartz crystal in the presence of 3mM of undissociated acetic acid (80°C, 0.1wt.% NaCl, and pCO ₂ =0.53 bar).....	97
Figure 55. Iron carbonate film dissolution with 0.1M of HCl (0.2 unit decrease in pH) at 80°C, 0.1wt.% NaCl, and pCO ₂ =0.53.....	98
Figure 56. Iron carbonate film dissolution with 0.1M of HCl (0.35 unit decrease in pH) at 80°C, 0.1wt.% NaCl, and pCO ₂ =0.53.....	99
Figure 57. SEM image of the iron carbonate film dissolution with HCl and CH ₃ COOH (80°C, 0.1wt.% NaCl, and pCO ₂ =0.53).....	100
Figure 58. Iron-carbon phase diagram[42].	110
Figure 59. Depiction of the formation of proeutectoid or primary iron carbide from austenite upon cooling slowly a hypoeutectoid steel.....	111
Figure 60. SEM image of the microstructure of X65 steel etched in 2% Nital solution.	112

CHAPTER 1: CORROSION IN OIL AND GAS PRODUCTION SYSTEM

1.1 Introduction

Corrosion is a process involving the deterioration of a metal. This occurs through a chemical or electrochemical reaction starting at the metal surface and involving a species in its local environment[1]. Corrosion is a phenomenon easy to perceive in everyday life, but it is not as trivial a process as it often appears. In a study of different industrial sectors, such as oil and gas exploration and production, motor vehicles, ships, petroleum refining, highway bridges, railroads, drinking water, sewer systems and defense, the estimated direct annual impact of corrosion in the United States in 2007 was determined to be \$276 billion per year, which is 3.1 percent of the gross domestic product (GDP). With a population of 303 million, this works out to be an average of \$1,416 per person per year[2]. The importance of corrosion does not only involve simply economics, but also the environment and society. Not anticipating corrosion can expose industry to a high risk of failure. In 1992, Guadalajara, Mexico, suffered its worst industrial accident related to the oil and gas industry. As a result of a failure in a gasoline pipeline, an undetected amount of gasoline leaked into the sewers, causing an explosion that destroyed many kilometers of streets and buildings. Numerous people died and many families were left homeless. Damage to the buildings was estimated to be \$300 million[3]. More recently, in March 2006, at the Prudhoe Bay field, Alaska, corrosion led to the spillage of at least 6,350 barrels of oil. The leak forced BP to suspend production and replace 16 miles of pipeline at a cost of \$250 million[4]. After this event, the cost per barrel of crude increased, having a direct impact on the economy worldwide. All of these

events could potentially have been avoided if the problems associated with corrosion had been detected and addressed. These problems highlight the importance of investment in research designed to develop new techniques, materials, alloys, and human resources that can contribute to preventing the damaging effects of corrosion.

1.2 Fundamentals of CO₂ corrosion

Corrosion by carbon dioxide (CO₂) represents a major problem for the oil and gas industries. Their pipelines are exposed to mixtures of hydrocarbons and aqueous solutions that contain high levels of CO₂. The presence of CO₂ and water causes an acidification of the environment which in turn leads to corrosion. Other factors that contribute to the corrosion rate are: temperature, pH, velocity of the liquid, and aqueous chemistry[5, 6].

In 1975 C. de Waard *et al.* proposed the first electrochemical mechanism for CO₂ corrosion of steel, considering the reduction of carbonic acid as the main cathodic reaction[7-9]. Work on this area was not continued until the late 1980s when Linda Gray *et al.* provided a more detailed approach to the de Waard model, taking into account the reduction of hydrogen ions, carbonic acid, and water as the main cathodic reactions, and the dissolution of iron as the anodic reaction [10, 11]. In 1995 building on the findings of various other studies, Netic *et al.* produced a mechanistic model for CO₂ corrosion based on the individual electrochemical reactions for a H₂O-CO₂ system [12]. The model assesses the electrochemical reactions resulting from the reduction of hydrogen ions, carbonic acid, water and oxygen, in addition to the anodic dissolution of iron. In contrast to the model developed by Gray *et al.*, which analyzed each reaction in isolation, this

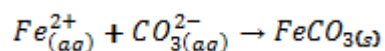
model combined the individual reactions to determine the corrosion rate more accurately. In addition, they provided a full description of the mechanisms controlling each electrochemical reaction (control by activation, diffusion, reaction, mixed). In the same year, B.F.M. Pots proposed a mechanistic model to predict the corrosion rate in a CO₂ system with multiphase flow conditions. The model was based on the assumption that the transport of species happened concurrently. The model also considered mass transfer, chemical reaction, and charge transfer processes[13].

Collectively, these studies provide the main sets of reactions to evaluate the corrosion rate by CO₂. They are as shown in Table 1 [7-9]:

Table 1. Chemical reactions and their equilibrium constants

	Cathodic reactions	Equilibrium constant
Dissolution of carbon dioxide	$CO_{2(g)} \rightleftharpoons CO_{2(aq)}$	$K_1 = \frac{[CO_2]}{p_{CO_2}}$
Water dissociation	$H_2O_{(l)} \rightleftharpoons H_{(aq)}^+ + OH_{(aq)}^-$	$K_2 = [H^+][OH^-]$
Hydrolyzation of carbon dioxide	$H_2O_{(l)} + CO_{2(aq)} \rightleftharpoons H_2CO_{3(aq)}$	$K_3 = \frac{[H_2CO_3]}{[CO_2]}$
Carbonic acid dissociation	$H_2CO_{3(aq)} \rightleftharpoons HCO_{3(aq)}^- + H_{(aq)}^+$	$K_4 = \frac{[HCO_3^-][H^+]}{[H_2CO_3]}$
Bicarbonate ion dissociation	$HCO_{3(aq)}^- \rightleftharpoons CO_{3(aq)}^{2-} + H_{(aq)}^+$	$K_5 = \frac{[CO_3^{2-}][H^+]}{[HCO_3^-]}$
Reduction of hydrogen ion	$2H_{(aq)}^+ + 2e^- \rightarrow H_{2(g)}$	
Anodic Reaction		
Dissolution of iron	$Fe_{(s)} \rightarrow Fe_{(aq)}^{2+} + 2e^-$	

Numerous authors have confirmed that an increase in the pH, temperature and concentration of Fe^{2+} favors the precipitation of the iron carbonate ($FeCO_3$) layer, causing a decrease in the corrosion rate [14-16]. The concentration of Fe^{2+} and CO_3^{2-} must exceed the solubility product in order to form the protective layer [14-17]:



This corrosion product layer can act as a diffusion barrier that limits the transport of species from the bulk solution to the steel surface and vice-versa [18].

1.3 CO_2 Corrosion in the presence of organic acids.

The nature of organic acids (R-COOH) in oil wells plays a determining role in the severity of corrosion. Organic acids are typically weak Brønsted acids that exist mostly as an undissociated molecular species. Like all weak acids, a certain moiety will dissociate to form hydrogen ions and an anionic conjugate base. There are several types of organic acids found in oil fields such as formic (H-COOH), acetic (CH_3 -COOH), propionic (CH_3CH_2 -COOH), and butyric ($CH_3CH_2CH_2$ -COOH). In most cases a mixture of the organic acids will be present, but with acetic acid dominant [19-21]. Sometimes one will be dominant, but in other cases they will be found in a mixture with each other. In 1973 Obuchova reported that the presence of formic, acetic, propionic, and butyric acids in a saturated aqueous solution with CO_2 increases the corrosion rate from 1.3 to 5.7 mm/yr in the North Sea. The organic acid content is considered to be one important factor in the increase of the corrosion rate even when only small amounts of organic acid are present. Crolet reported that merely 1 mM acetic acid can increase the corrosion rate[22].

While the other organic acids can impact the corrosion rate, the vast majority of the literature on the effect of organic acids on CO₂ corrosion of carbon steel focuses on acetic acid. This is because this acid is usually the most abundant in the mixture of organic acids seen in the field [23].

CHAPTER 2: NON-SCALE FORMING CONDITIONS IN THE PRESENCE OF ORGANIC ACIDS

2.1 Introduction

The primary material used in pipelines for the oil and gas industry is API X65 carbon steel, due to its low price, strength and availability. However, carbon steel corrodes in the presence of carbonic and organic acids [24, 25]. Carbon dioxide can be found naturally in water as a dissolved gas in underground oil and gas reservoirs, resulting in formation of carbonic acid. Organic acids can be naturally occurring or injected into the host formation for various purposes, *e.g.*, reservoir stimulation.

Several authors reported that there is a direct correlation between the corrosion rate and the presence of organic acids, even when traces of undissociated organic acid are present [19, 22, 26].

Therefore, it is important to investigate the conditions under which organic acids induce corrosion damage to carbon steel. The extent of R-COOH/CO₂ corrosion depends on many variables such as pH, temperature, flow velocity, CO₂ partial pressure and aqueous chemistry.

2.2 Objective

The aim of this chapter is to determine the differences in the electrochemical behavior of various organic acids under the same total concentration and under the same pH and undissociated concentration.

2.3 Experimental method

A three electrode setup was used in all the experiments as shown in Figure 1. API X65 steel* was used as a working electrode (WE). A concentric platinum ring was used as a counter electrode (CE), and a saturated silver-silver chloride (Ag-AgCl) electrode was used as the reference electrode (RE) via a Luggin capillary. Throughout the entire experiment the pH was monitored. Temperature was regulated using a thermocouple immersed in the solution and a controller linked to a hot plate. The experimental temperature was maintained within $\pm 1^\circ\text{C}$ in all experiments.

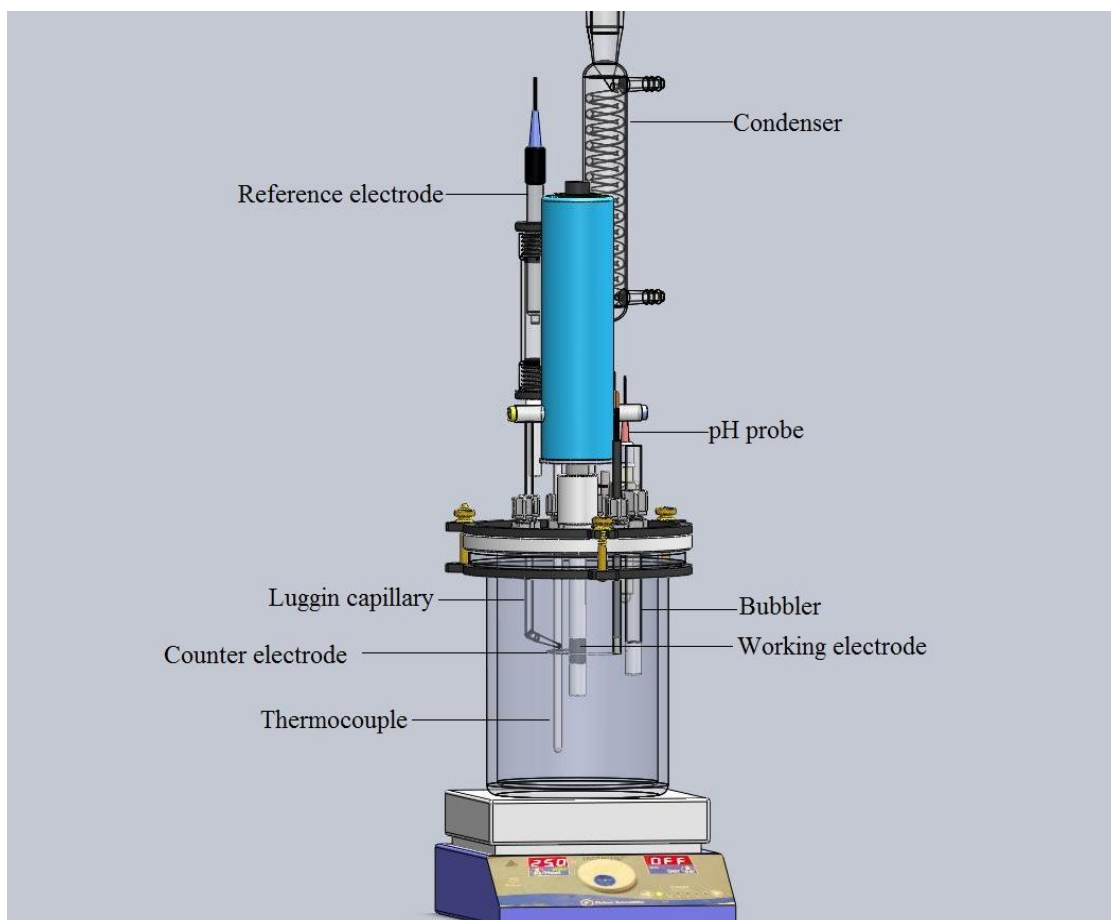


Figure 1. Experimental cell design.

* See appendix I for the characterization of the material

The glass cells were filled with 2 liters of 1wt.% NaCl electrolyte. To facilitate deoxygenation either N₂ or CO₂ was continuously bubbled through the electrolyte for approximately 1 hour before the experiment and during the entire experimental procedure. When needed, deoxygenated hydrochloric acid (HCl) 1M or sodium hydroxide (NaOH) 1M was added to adjust the pH.

One problem with the experimental set up results from the consumption (reduction) of carbonic and/or organic acids at the steel surface. In the case of carbonic acid, the dissolution and hydration of CO₂ replenishes the acid. But, for the organic acids, as they are consumed by the corrosion process, the small amount of organic acid vapour is unable to counter this change. To avoid or minimize the consumption of the organic acid, one can: 1) reduce the testing time and depletion of the acid and 2) reduce the exposed area (Figure 2).

Before each polarization experiment, the working electrode surface was polished using 240, 320, 400 and 600 grit silicon carbide (SiC) paper, washed with isopropyl alcohol and acetone, mounted on the specimen holder, and immersed into the electrolyte. The open circuit potential (E_{oc}) was immediately measured. Polarization resistance (R_p) measurements were conducted by polarizing the WE ± 5 mV from the E_{oc} and scanning at 0.1mV/s. The solution resistance was measured independently using electrochemical impedance spectroscopy (EIS). Impedance measurements were accomplished by applying an oscillating potential (± 5 mV) around the E_{oc} to the working electrode using the frequency range of 1Hz to 100kHz. At the end of each experiment, cathodic and anodic potentiodynamic sweeps, were conducted in this order starting from the open

circuit potential to provide useful information regarding the corrosion mechanisms and corrosion rate.

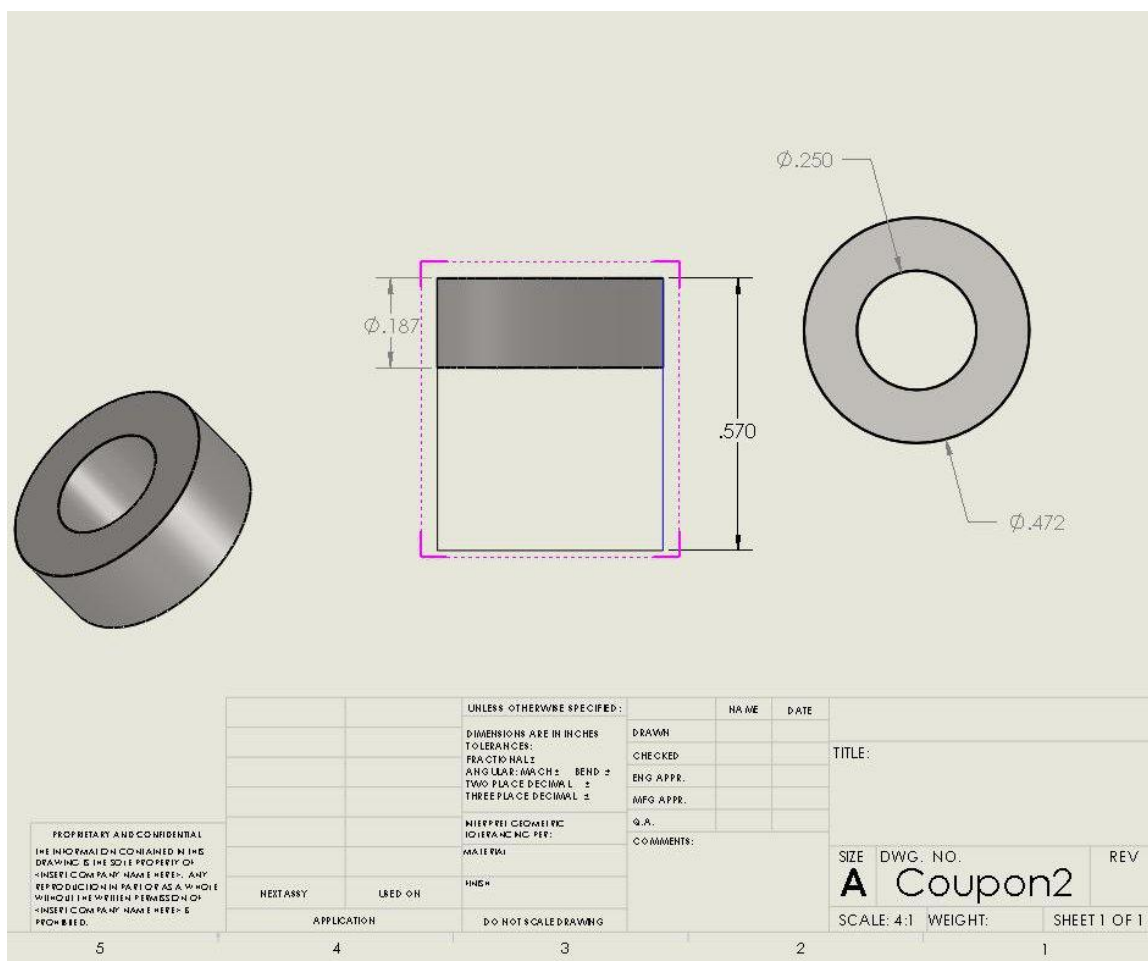


Figure 2. Schematic design for the new rotating cylinder electrode (RCE).

Two sets of experiments were done in order to differentiate the electrochemical behaviour of different acids. Table 2 shows the first set of experiments which evaluates the total molar concentration of different acids at autogenous pH. For the second set of experiments, the molar concentration of the undissociated acid and pH were fixed (Table 3). For each experiment, the molar concentration of acid in the system was measured by

titration of a 20ml sample with 0.1M NaOH at the beginning and at the end of the experiment to observe if there was a change in concentration.

Table 2. Experimental conditions (same total molar concentration at autogenous pH)

Test solution	Deionized water + 1wt.%NaCl
Test material	X65 steel
Temperature	25°C
Total pressure of CO ₂	1 bar
Undissociated (free) organic acid	0.03M
pH	autogenous pH of the organic acid in N ₂ or CO ₂
Rotation velocity	1000rpm
Polarization resistance	From -5mV to 5mV (vs E _{oc}) (scan rate 0.1mV/s)
AC Impedance	± 5mV vs. E _{oc} from 1mHz to 100KHz
Potentiodynamic sweep	From 0mV to -400mV (scan rate 1mV/s) From 0mV to 200mV (scan rate 1mV/s)

Table 3. Experimental conditions (same undissociated molar concentration at fixed pH)

Test solution	Deionized water + 1wt.%NaCl
Test material	X65 steel
Temperature	25°C
Total pressure of CO ₂	1 bar
Undissociated (free) organic acid	0.003M
pH	4.0
Rotation velocity	1000rpm
Polarization resistance	From -5mV to 5mV (vs E _{oc}) (scan rate 0.1mV/s)
AC Impedance	± 5mV vs. E _{oc} from 1mHz to 100KHz
Potentiodynamic sweep	From 0mV to -400mV (scan rate 1mV/s) From 0mV to 200mV (scan rate 1mV/s)

It is important to evaluate and compare the electrochemical behavior of different organic acids to determine whether the concentration of the undissociated acid alone is the most important factor or if it is a combination of different variables such as pH, temperature, and flow velocity in addition to the concentration of undissociated acid.

2.4 Results and Discussion

2.4.1. Effect of the total molar concentration for different acids

The electrochemical behavior of different acids at the same molar concentration was evaluated using electrochemical techniques. The pH was not adjusted during the entire length of the experiment because the goal was to evaluate the availability of the acids within the system without changing the concentration. The desired amount of the acid was added into the system to achieve the same molar concentration. It is a common mistake to compare the effect of different acids by using the same concentration measured in ppm instead of molarity, the latter being more logical because chemical reaction rates are based on moles of reactant. The total concentration in ppm is different for each acid because of the differences in molecular weight (Table 4). The acids used for this set of experiments were formic, acetic, propionic and hydrochloric.

Table 4. Amount of acid to be added in ppm to get 0.03M

Acid	Total concentration (M)	Total concentration (ppm)
Formic	0.03	1380
Acetic	0.03	1800
Propionic	0.03	2220

Table 5 shows the distribution of species at autogenous pH corresponding to the addition of 0.03M of acetic acid.

Table 5. Distribution of species at 0.03M and autogenous pH

Acid	Total concentration (M)	Autogenous pH	Concentration	
			undissociated acid (M)	Anion (M)
Hydrochloric	0.03	1.52	0.00	0.03
Formic	0.03	2.63	0.01089	0.01910
Acetic	0.03	3.13	0.02549	0.00450
Propionic	0.03	3.18	0.02628	0.00371

Hydrochloric acid is expected to yield a higher corrosion rate as a result of the lower pH (pH 1.53) compared with the other acids. Since hydrochloric acid has approximately 10 times more hydrogen ions than formic acid at the same pH, it is expected to produce a higher rate of corrosion, but this was not the case. With the organic acids the corrosion rate is not influenced only by pH, but also by the concentration of the undissociated acids and possibly the anion of the acid (see Figure 3) In the case of formic acid, the formate anion could form a complex with ferrous ions and this would help accelerate the rate of corrosion as shown in Figure 3. Under these experimental conditions, formic acid (weak acid) is more corrosive than hydrochloric acid (strong acid) resulting in an increase of corrosion rate.

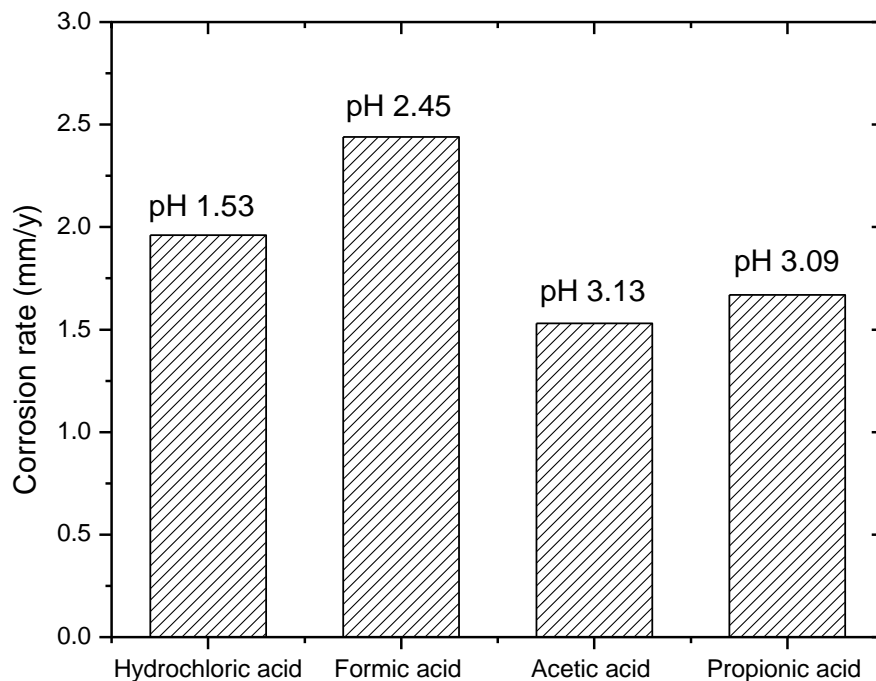


Figure 3. Effect of total molar concentration of different acids on the corrosion rate of X65 steel at autogenous pH after 5 hours of exposure (25°C, 1000rpm, 1 wt.% NaCl, and $p\text{CO}_2=0.98\text{bar}$).

The potentiodynamic sweeps (Figure 4) show a slight difference in the electrochemical behavior of acetic and propionic acid. Formic acid is the most corrosive of these acids. It is not possible to distinguish the limiting current for these acids because the corrosive species concentration of 0.03M is too high. The reactions are under kinetic control (charge transfer control). This is often the case in acid corrosion of steel at high concentration.

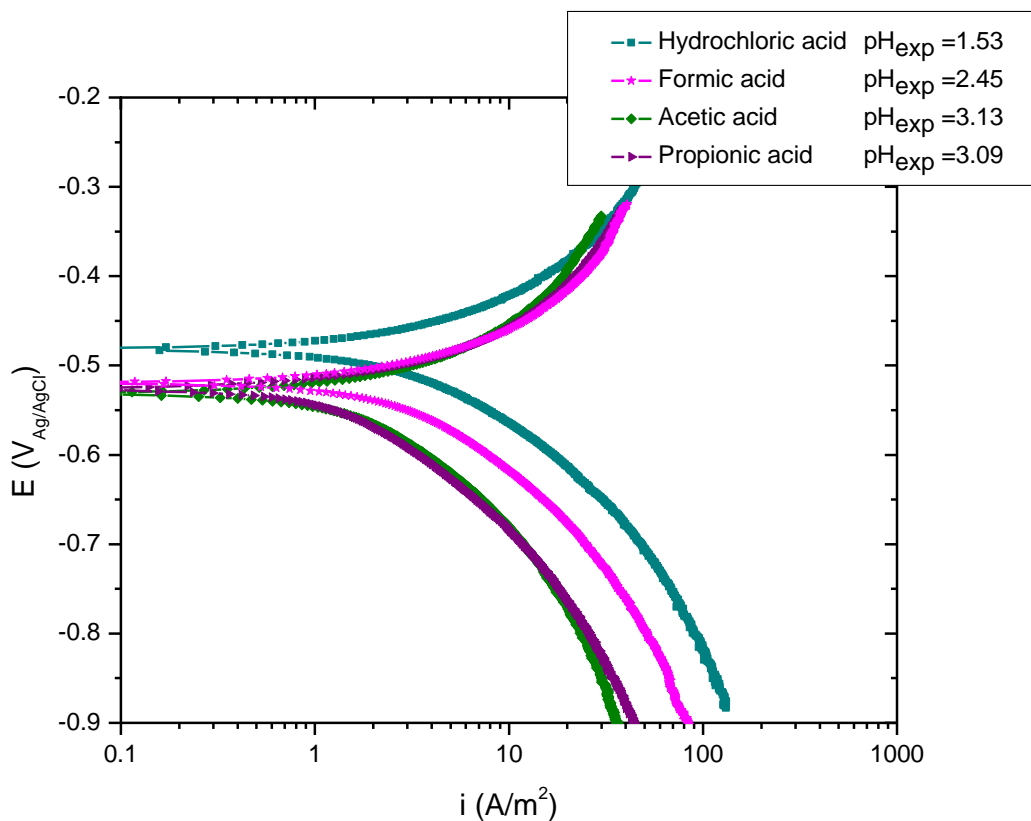


Figure 4. Potentiodynamic sweeps X65 steel (25°C, 1000rpm, 1 wt.% NaCl, and $p\text{CO}_2=0.98\text{bar}$).

2.4.2. Effect of same undissociated molar concentration at fixed pH

The aim of this research is to distinguish the difference between the acids' impact on the corrosivity of the solution. Each acid will have an effect on the pH, thus a fixed pH is used to fix the concentration of hydrogen ions which limits the number of variables in the experiment. Therefore, this study will distinguish the effect of each undissociated acid and determine whether one is more corrosive than the others.

In order to compare these acids with CO_2 , it is necessary to use the equivalent CO_2 species, carbonic acid, which is the undissociated portion of the acid. At first, 0.03M of undissociated organic acid was going to be used, but, to get 0.03M of carbonic acid it

would be necessary to use 370 bar of CO₂. A high pressure like this cannot be used for a glass cell experiment. Hence, it was necessary to decrease the concentration 10 times from 0.03M to 0.003M (Table 6).

Table 7 shows the distribution of species at pH 4 and 0.003M of each undissociated acid.

Table 6. pCO₂ required to get 0.03M of carbonic acid (H₂CO₃)

pCO ₂	[H ₂ CO ₃]	[CO ₂]
370	0.03M	11.78
37	0.003M	1.17
20	0.0016M	0.636

Table 7. Distribution of species at pH 4 and 0.003M of undissociated acid

Acid	Total concentration (M)	undissociated acid (M)	Anion (M)
Formic	0.00826	0.003	0.00526
Acetic	0.00352	0.003	0.00052
Propionic	0.00342	0.003	0.00042

Figure 5 shows the potentiodynamic sweeps for different acids at 0.03M, pH 4, 1000rpm and 25°C. There is no limiting current visible in the potentiodynamic sweeps at 0.03M because of the large concentration of corrosive species which led to large corrosion currents and significant interference in measurements by solution resistance. With the concentration lowered to 0.003M for each undissociated acid, Figure 6, it is possible to see the limiting currents in the potentiodynamic sweeps. Notice that the species with the highest diffusion coefficient, H⁺, has the largest limiting current. To match the concentration of carbonic acid, the potentiodynamic sweeps from Wang's

experiments at 20 bar of CO₂ were used. This experiment was conducted at the Institute for Corrosion and Multiphase Technology at Ohio University.

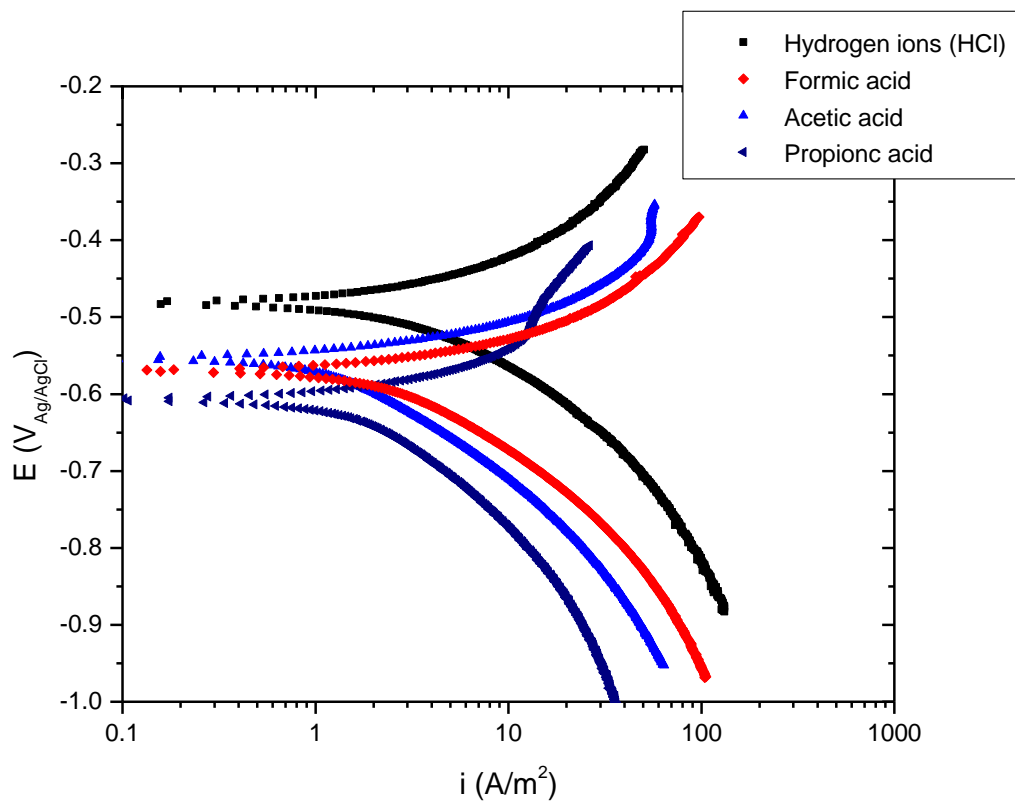


Figure 5. Potentiodynamic sweeps for X65 steel (pH 4, 25°C, 1000rpm, 1 wt.% NaCl, pCO₂=0.98bar, and [R-COOH] = 0.03M).

Figure 6 shows that carbonic acid has the highest limiting current and is more corrosive than the other acids. But this is because it is constantly being replenished by the dissolution and hydration of carbon dioxide.

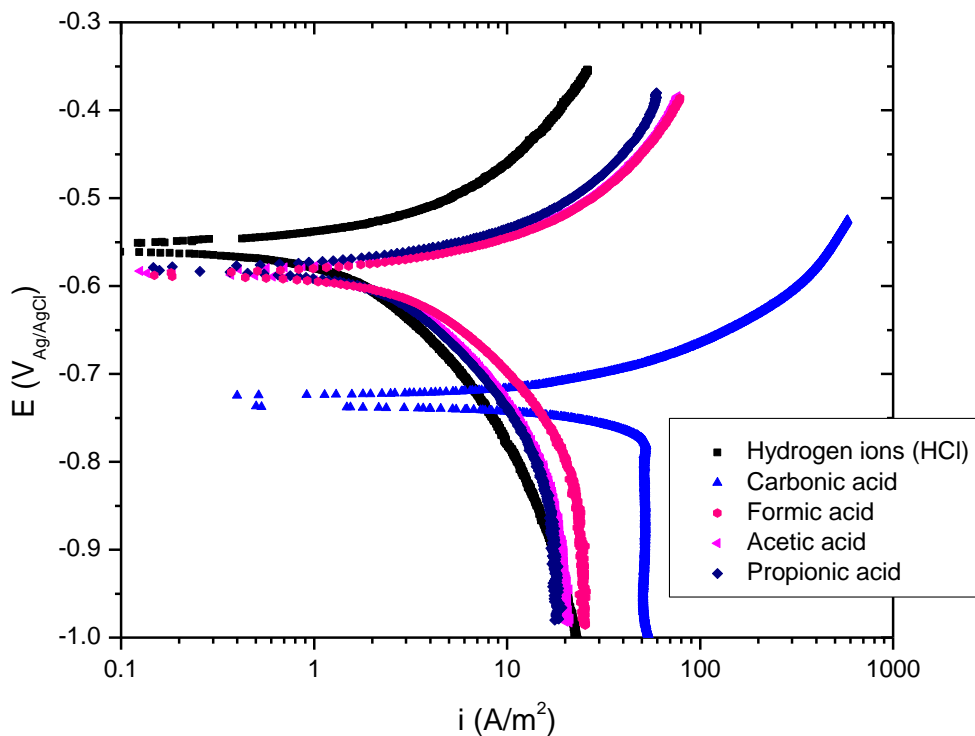


Figure 6. Potentiodynamic sweeps for X65steel (pH 4, 25°C, 1000rpm, 1 wt.% NaCl, $p\text{CO}_2=0.98\text{bar}$ and $[\text{R-COOH}] = 0.003\text{M}$).

Figure 7 shows the potentiodynamic sweeps for X65 steel in acetic acid solution at different concentrations, 0.03 and 0.003M. All organic acids are surface active substances; there is strong evidence that they are adsorbing at the steel surface and changing the wettability of the steel, particularly the larger organic molecules. These molecules do interfere with the electrochemical process at the steel surface; in other words, they interfere with iron dissolution. They may also interfere with the cathodic reaction, but since they adsorb at the steel surface and are reduced there, this interference could not be observed in a cathodic potentiodynamic sweep. What can be observed is that the largest molecules retard the anodic part of the potentiodynamic sweeps. With a higher molar concentration of acetic acid, the corrosion rate unexpectedly decreases at 0.03M

because in this case, the anodic reaction dominates. The corrosion rate is slightly lower for propionic and acetic acid at 0.03M (Figure 8).

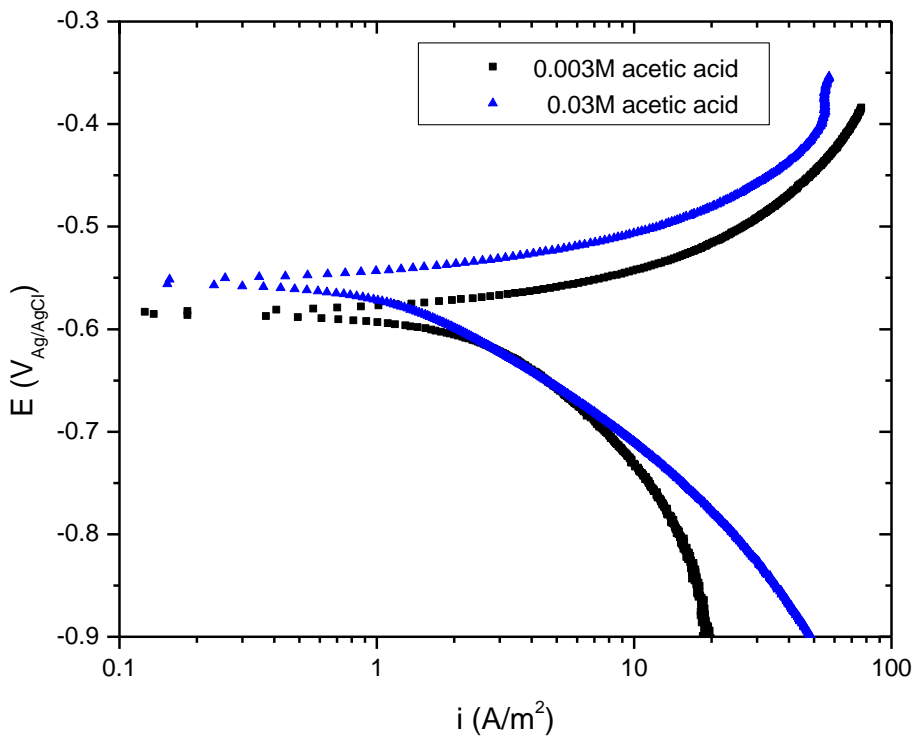


Figure 7. Potentiodynamic sweeps for X65 steel (pH 4, 25°C, 1000rpm, 1 wt.% NaCl and $pCO_2=0.98bar$).

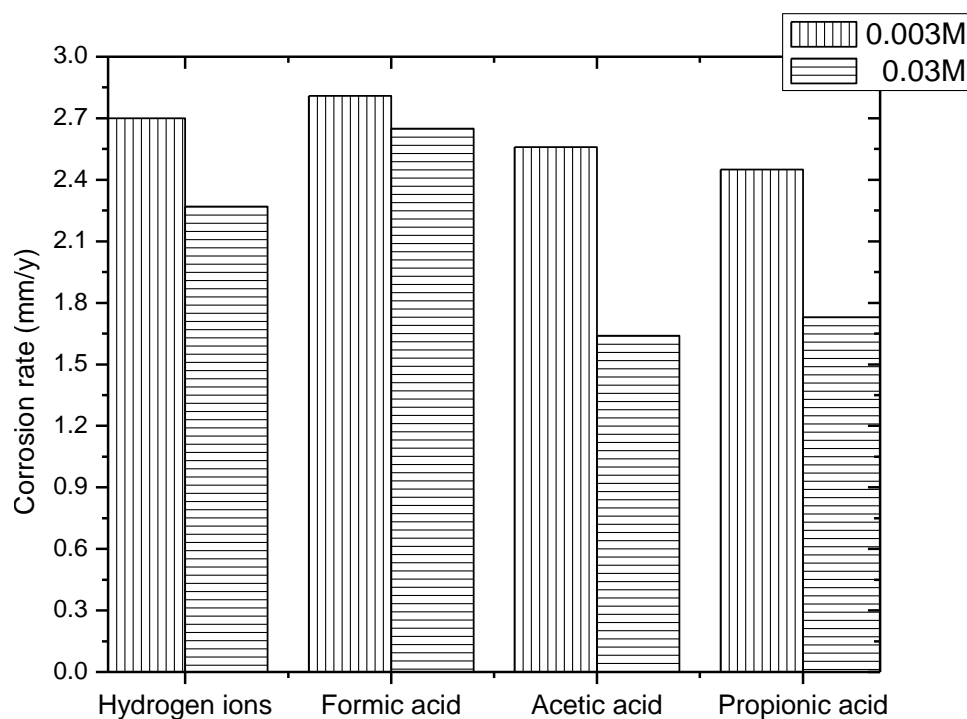


Figure 8. Effect of different acids on the corrosion rate of X65 steel (pH 4, 25°C, 1000rpm, 1 wt.% NaCl, $p\text{CO}_2=0.98\text{bar}$, and $[\text{R-COOH}] = 0.003\text{M}$).

2.5 Summary

- There is very little difference in electrochemical behavior of formic, acetic, and propionic acid (under the same pH and concentration of undissociated organic acid).
- The addition of any of the acids clearly changed the corrosion process by increasing the cathodic reaction and mildly retarding the anodic reaction.
- The increase in corrosion rate is due to the presence of undissociated organic acid.

CHAPTER 3: INTEGRITY OF FeCO_3 LAYER IN THE PRESENCE OF ACETIC ACID[†]

3.1 Introduction to FeCO_3 layer forming conditions

The formation of iron carbonate (FeCO_3) as the main corrosion product in CO_2 environments retards the corrosion rate, but the presence of acetic acid is thought to damage the iron carbonate layer and temporarily increase the corrosion rate [27]. A key element in understanding the role of organic acids in corrosion processes is to determine how they affect the formation and integrity of the FeCO_3 layer. The presence of organic acids does not affect the rate of iron carbonate precipitation, but does prolong the time it takes to form a protective scale [28]. It is suspected that at a pH above 5.6, acetic acid does not affect the solubility of the iron carbonate directly, but rather diffuses through the pores of the layer and directly attacks the steel underneath. As a consequence, the bare steel area and the surrounding area covered by protective layer are exposed to the same corrosive environment and a galvanic cell is established [28-30]. Initiation of localized corrosion can occur by either chemical or mechanical means, and acetic acid has been observed to selectively damage the iron carbonate layer and under specific conditions may cause localized corrosion.

The present research focuses on evaluation of the effect of acetic acid on the integrity and protectiveness of the iron carbonate layer formed on API X65 steel. The effect of three key parameters was observed: concentration of undissociated acetic acid, flow velocity and pH.

[†] Part of the work presented in this chapter was presented at the 2008 NACE International Conference in New Orleans [28].

3.2 Experimental procedure

A three-electrode setup was used in all the experiments and is shown in Figure 9. X65 mild steel material was used for the rotating cylinder electrode (RCE), which served as the working electrode (WE). A platinum wire was used as a counter electrode (CE) with a saturated silver-silver chloride (Ag/AgCl) reference electrode (RE). The pH was monitored with an electrode immersed in the electrolyte. The temperature was regulated using a thermocouple immersed in the solution and a controller linked to a hot plate.

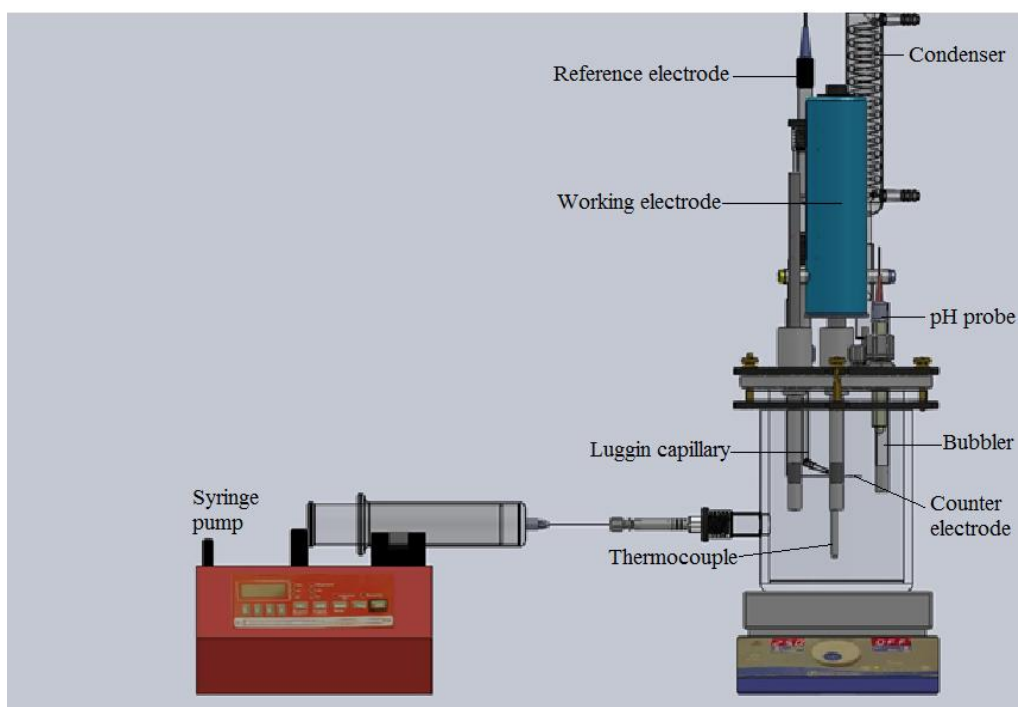


Figure 9. Experimental cell design – Iron carbonate layer formation.

The glass cell was filled with 2 liters of electrolyte, which correspond to 3wt.%NaCl (prepared using deionized water). In all experiments, CO₂ was continuously bubbled through the electrolyte for approximately 1 hour before experimentation and during the entire experimental procedure. This was done in order to ensure that all the

dissolved oxygen was removed and to maintain saturation with CO₂ of the test solution. When needed, a hydrochloric acid (HCl) or sodium bicarbonate (NaHCO₃) solution was added to adjust the pH. The experimental temperature was maintained within $\pm 1^\circ\text{C}$ in all experiments.

To begin each experiment, the steel surface was polished using 240, 320, 400 and 600 grit silicon carbide (SiC) paper, washed with isopropyl alcohol, dried, mounted on the specimen holder, and immersed into the electrolyte. The open circuit potential was immediately measured. Polarization resistance (R_p) measurements were conducted by polarizing the WE $\pm 5\text{mV}$ from the E_{oc} at a scan rate of 0.1mV/s . The solution resistance was measured independently using alternating current (AC) impedance and the measured R_p was then determined. AC impedance measurements were done by applying an oscillating potential ($\pm 5\text{mV}$) around the E_{oc} to the WE using the frequency range of 1Hz to 100kHz.

Three sets of experiments were conducted, using the experimental conditions defined in Table 8, to evaluate the effect that acetic acid has on the integrity of the iron carbonate layer. Variations of the flow velocity and pH in the presence of acetic acid were also evaluated. The acetic acid was always added as a buffered aqueous solution to allow the control of the pH.

Table 8. Experimental conditions – iron carbonate precipitation

Test solution	Deionized water + 3wt.%NaCl
Test material	X65 steel
Temperature	80°C
Total pressure of CO ₂	0.53 bar
Undissociated (free) organic acid	0.8 and 1.6mM (50 and 100ppm respectively)
pH	6.0 and 6.3
Rotation velocity	Static conditions, 100 and 1000rpm
Initial supersaturation	100
Sweep rate	0.1 mV/s to 0.2 mV/s
Polarization resistance	From -5mV to 5mV (vs E _{oc})
AC Impedance	± 5mV vs. E _{oc} from 1mHz to 100KHz

The first set of experiments was done in order to determine the influence of acetic acid on the iron carbonate layer at a constant pH. Therefore, the acetic acid was added into the system as a buffered acetic acid solution with the same pH. The conjugate acid-base pair was acetic acid, CH₃COOH, and acetate ion, CH₃COO⁻ supplied as a soluble salt, such as sodium acetate trihydrate NaC₂H₃O₂·3H₂O. The physical and chemical properties of acetic acid are listed in Table 9. The experiments were carried out with two different undissociated acetic acid concentrations, 0.8 and 1.6mM (50 and 100ppm, respectively) at pH 6.3 (see Table 10).

Table 9. Physical and chemical properties of acetic acid [31, 32]

	Acetic acid
Formula	CH ₃ -COOH
Molecular weight, g/mol	60.05
Density, g/ml at 20°C	1.049
Melting point, °C	16.5
Boiling point, °C	118.1
Acidity (pK _a)	4.76

Table 10. Acetic acid concentration at pH 6.3 and 80°C

Total Concentration		Undissociated acetic acid		Acetate concentration	
(M)	(ppm)	(M)	(ppm)	(M)	(ppm)
0.0238	1418	0.0008	50	0.0229	1368
0.0476M	2836	0.0016	100	0.0459	2736

The buffered acetic acid solution was added into the electrolyte only after a protective iron carbonate layer formed on the steel sample as indicated by a reduction in the corrosion rate to approximately 0.2 mm/y. The total concentration of acetic added into the system was either 0.23M or 0.047M. All tests in this series were conducted at 80°C, 1 bar total pressure (0.56 bar pCO₂, balance pH₂O), 3wt.% NaCl, pH 6.3 and static conditions. The initial supersaturation of the electrolyte with respect to iron carbonate was approximately 100 and was not maintained during the test. Therefore the supersaturation rapidly decreased as iron carbonate precipitated and the solution drifted back toward thermodynamic equilibrium.

The effect that the flow velocity has on the integrity and protectiveness of the iron carbonate layer in the presence of acetic acid was evaluated in the second set of experiments. The iron carbonate layer was developed under different rotational velocities (static, 100 and 1000 rpm). The rotational velocity was maintained constant during each velocity test. These experiments were also conducted at 80°C, 0.53 bar pCO₂, 3wt.% NaCl, 0.8mM (50ppm) of undissociated HAc, and pH 6.3. The initial supersaturation was 100.

Finally, the third set of experiments was conducted to see the effect of pH under the same undissociated acetic acid concentration. Once the iron carbonate layer formed at 80°C, 0.53 bar pCO₂, 3wt.% NaCl, pH 6.3 and initial supersaturation 100, the buffered acetic acid solution (0.8mM of undissociated HAc) was added into the system. The pH of the buffered solution which was added was 6.0 with the intention of lowering the pH of the original electrolyte. This was possible since the buffered solution was made with a smaller amount of acetate salt (Table 11).

Table 11. Acetic acid concentration at different values of pH at 80°C

pH	Undissociated acetic acid		Acetate concentration	
	(M)	(ppm)	(M)	(ppm)
6.0	0.0008	50	0.0113	685
6.3	0.0008	50	0.0229	1368

Analysis of the corrosion product scale was performed using scanning electron microscopy (SEM), energy dispersive X-ray analysis (EDX) and X-ray diffraction (XRD). See appendix III for further description of the use of these techniques.

3.3 Results and discussion

A large number of baseline experiments with iron carbonate layer formation in pure CO₂ corrosion (in the absence of acetic acid) were conducted. At the beginning of each experiment, the corrosion rate on the bare steel surface was typically 1 mm/y and decreased within a few days to values which were approximately one order of magnitude lower (< 0.1 mm/y) as iron carbonate layer formed. For the five experiments reviewed here, the acetic acid was added only after the FeCO₃ layer formed and the corrosion rate

remained stable for 2 days (in Figure 10, Figure 11, Figure 17, Figure 19, Figure 22 this is shown by a vertical line).

3.3.1. Influence of acetic acid concentration

In Figure 10 it is seen that the corrosion rate decreased to a low level (0.2 mm/y) following formation of an iron carbonate layer. The addition of 0.8 mM (50ppm) of undissociated acetic acid caused a temporary increase in the corrosion rate to about 0.3 – 0.4 mm/y, however this was followed by another decrease and within a day the corrosion rate settled back to 0.2 mm/y and remained constant beyond that point. In Figure 11, it is shown that in another similar experiment, the addition of 1.6mM of undissociated acetic acid increased the corrosion rate up to 1.4 mm/y. However, it proved that this effect was also temporary, as after a few days the corrosion rate returned to the low values below 0.2 mm/y. This behaviour appeared to be as expected, at least when compared with the previous work done in the same laboratory [28, 33]. Since the corrosion rate only temporarily increased with addition of acetic acid and eventually returned to the low values it had before the acetic acid was added, it was assumed that the protective iron carbonate layer was not affected, as reported earlier[28, 33].

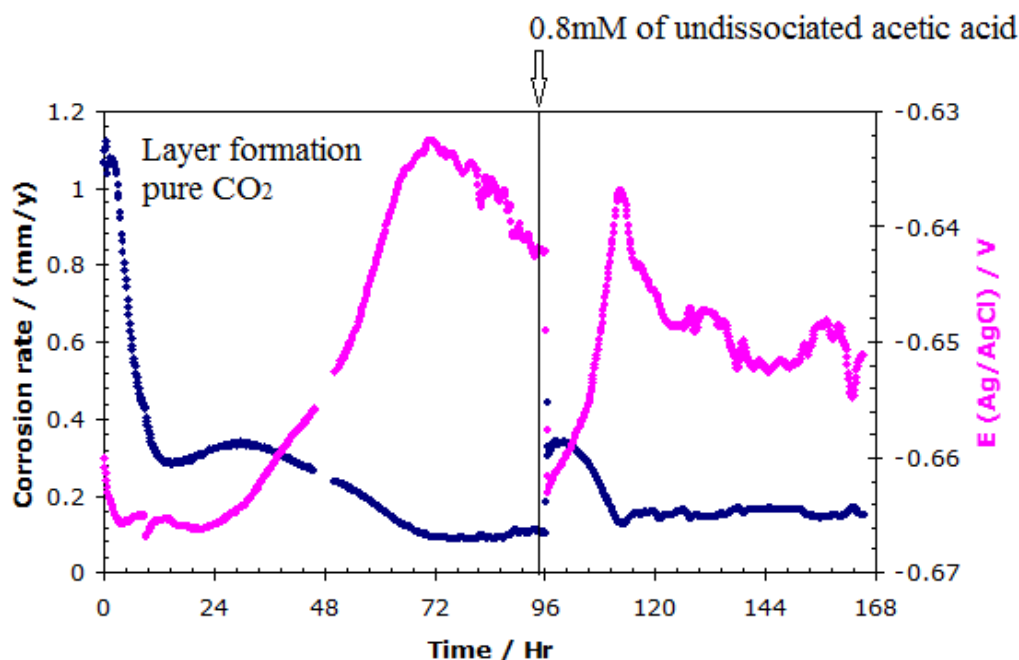


Figure 10. The effect of 0.8mM of undissociated acetic acid on the corrosion rate and corrosion potential of X65 steel during 168 hours of exposure (3 wt.% NaCl, pH 6.3, $p\text{CO}_2=0.53\text{bar}$, static conditions and 80°C).

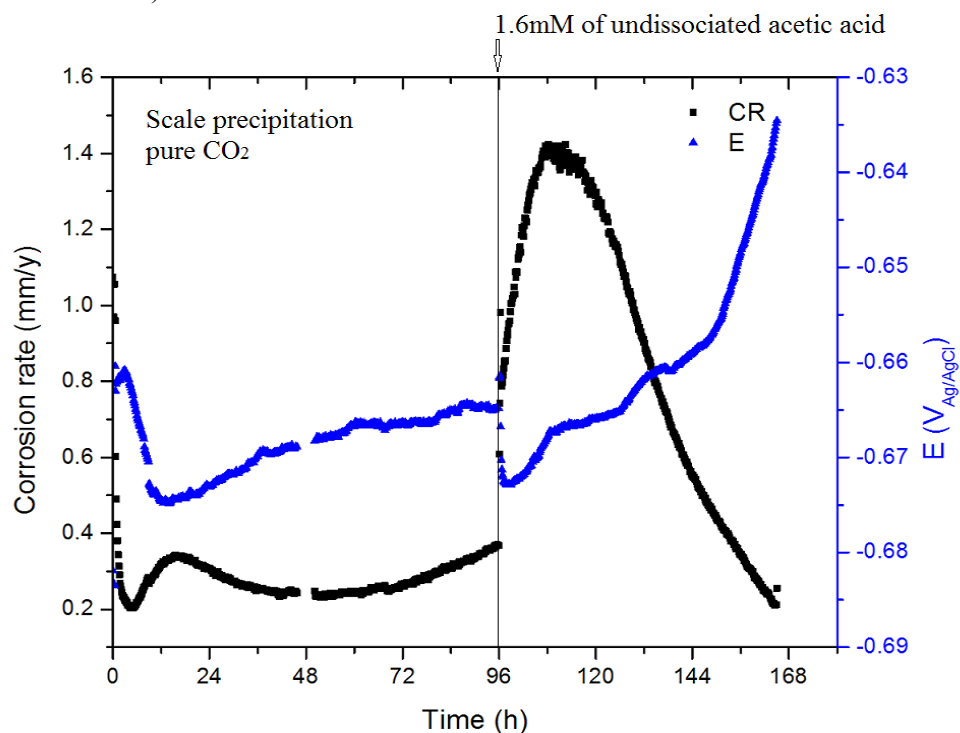


Figure 11. The effect of 1.6 mM of undissociated acetic acid on the corrosion rate and corrosion potential of X65 steel during 168 hours of exposure (3 wt.% NaCl, pH 6.3, $p\text{CO}_2=0.53\text{bar}$, static conditions and 80°C).

However, the SEM images show a significant loss of iron carbonate crystals from the surface following the addition of acetic acid, and even more so when the concentration of acetic acid was higher (Figure 12b and Figure 13b). This seems to support the view that the solubility of the iron carbonate increases in the presence of the acid even if the pH is maintained (presumably via complex formation)[27]. However, a more careful examination of the SEM images shows that the surviving crystals still have sharp edges and maintain the hexagonal morphology, and this is not a hallmark of a crystal dissolution process. Dissolution typically (but not always) leads to some “rounding” of the crystals, surface pitting and generally leaves behind more irregular crystalline shapes. Therefore, it is suspected that in these experiments the organic acid either: (a) led to a case of selective dissolution of iron carbonate (which is yet to be proven and explained) or the acid did not do much to the crystals but rather it has diffused through the pores of the layer and directly attacked the steel underneath (as evidenced by the temporary increase in the corrosion rate seen in Figure 10 and Figure 11). This has led to the undermining of the iron carbonate layer and the weakening of adhesion between the iron carbonate and the steel that eventually lead to loss of parts of the layer by detachment.

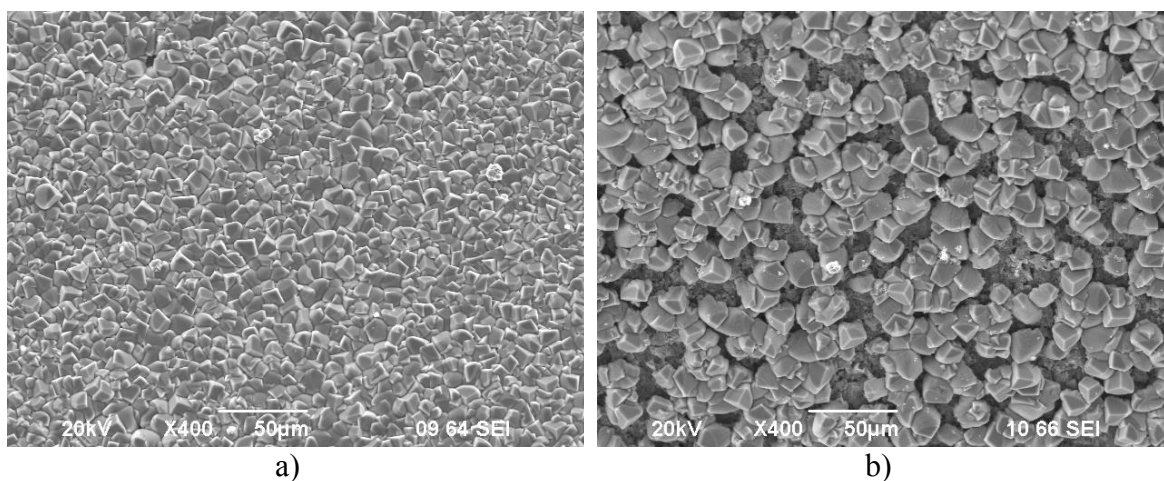


Figure 12. FeCO₃ layer morphology of X65 steel (3 wt.% NaCl, pH 6.3, pCO₂=0.53bar, static conditions and 80°C). a) layer formed after 96 hours in CO₂ environment and b) 72 hours after addition of the acetic acid/acetate buffer solution (0.8 mM of undissociated acetic acid)

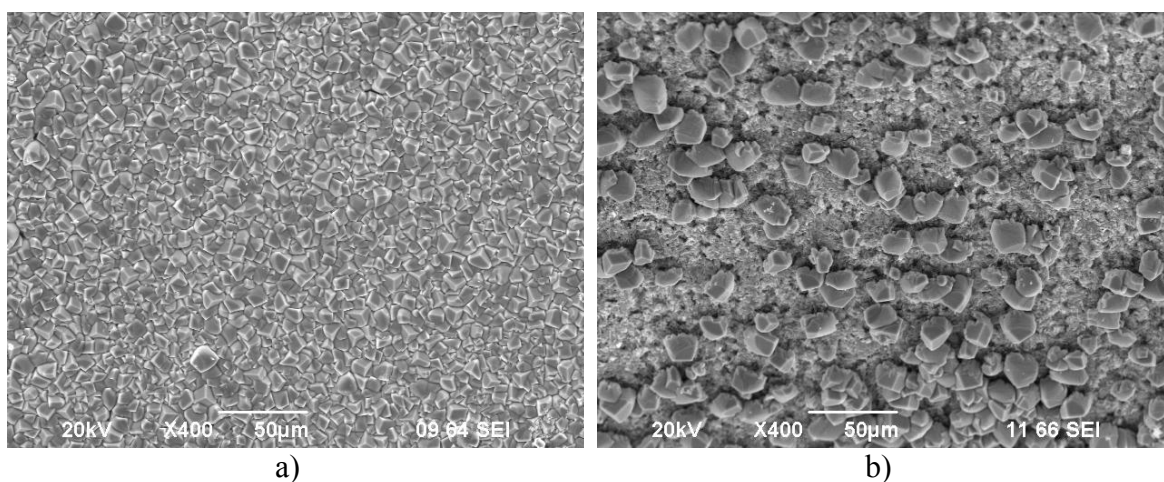


Figure 13. FeCO₃ layer morphology of X65 steel (3 wt.% NaCl, pH 6.3, pCO₂=0.53bar, static conditions and 80°C). a) layer formed after 96 hours in CO₂ environment and b) 72 hours after addition of the acetic acid/acetate buffer solution (1.6 mM of undissociated acetic acid)

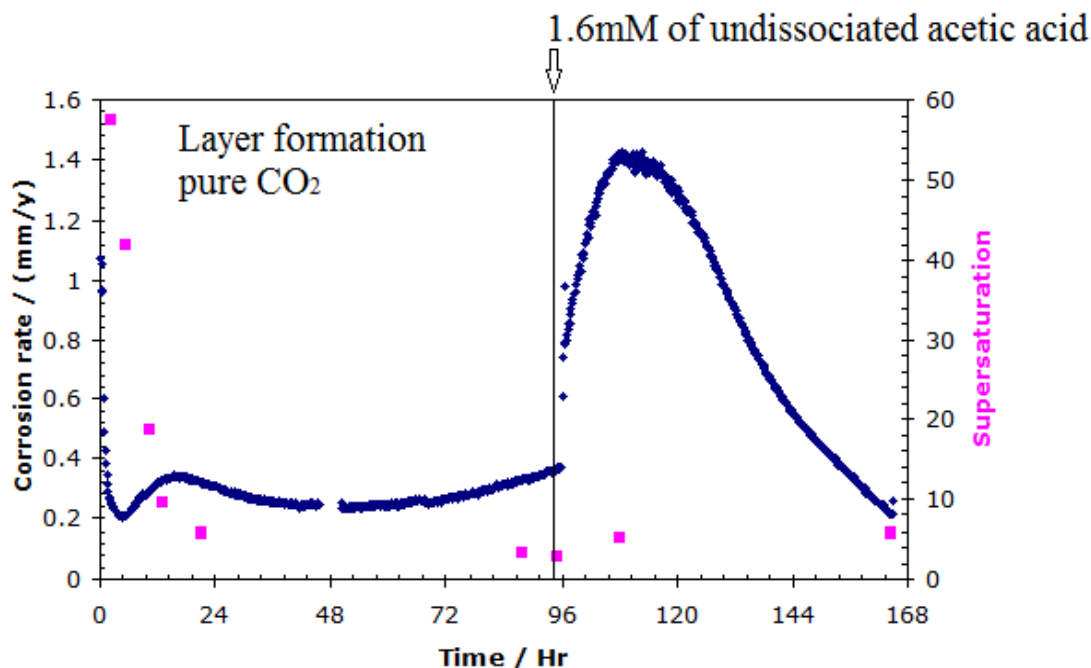


Figure 14. The effect of 1.6 mM of undissociated acetic acid on the corrosion rate and supersaturation during 168 hours of exposure (3% NaCl, pH 6.3, $p\text{CO}_2=0.53\text{bar}$, static conditions and 80°C).

In conjunction with SEM, energy dispersive X-ray analysis (EDX) was used to confirm the elements present in the layer seen on the X65 steel. Figure 15 shows EDX analysis of: (a) a crystal seen on the steel surface following the attack by acetic acid and (b) an exposed substrate, the space where the crystal was removed. The crystal shows the peaks of Fe, O, and C elements that form the FeCO_3 , while the exposed surface only shows the peak of Fe. While this seems logical, a perplexing question remains unanswered. *How can an iron carbonate surface layer which survived the acetic acid attack and which is as porous as the one seen in Figure 12b and Figure 13b still protect the steel surface from corrosion?* Furthermore, this porous layer appears to be as

protective as the much denser layer seen before the acid was added (see Figure 12a and Figure 13a).

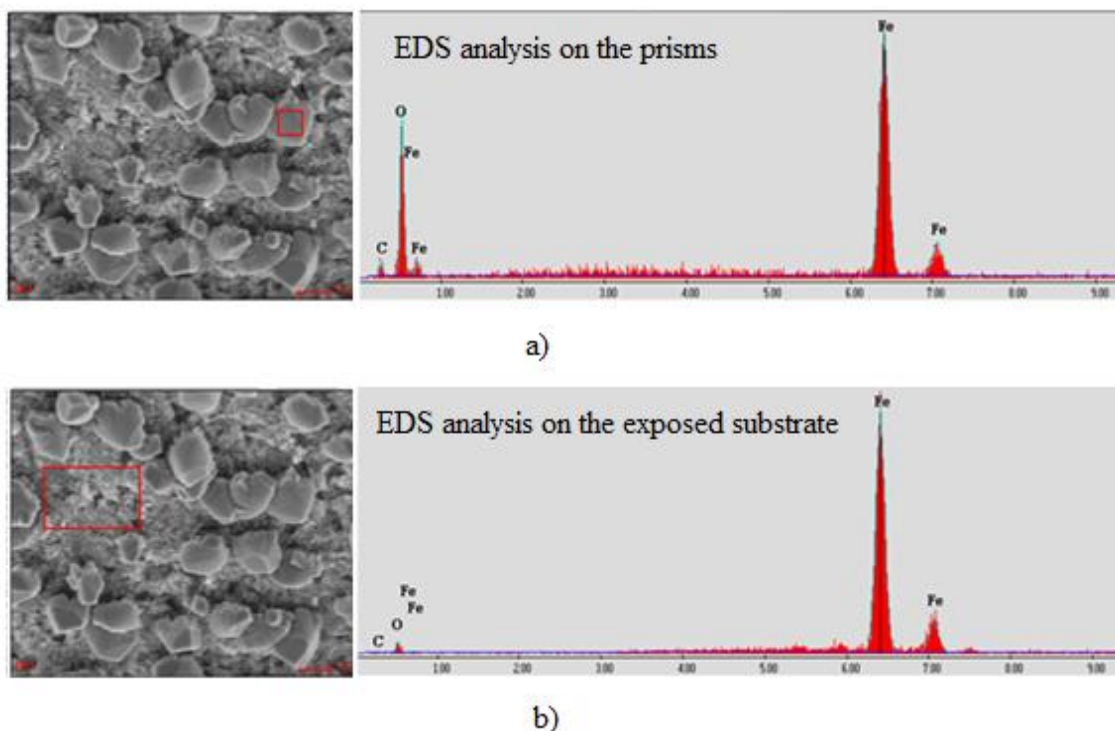


Figure 15. EDX analysis of the a) crystal and b) the exposed substrate after the addition of 1.6mM of undissociated acetic acid at pH 6.3, static conditions and 80°C. Sample taken at the end of the experiment shown in Figure 11 above.

X-ray diffraction (XRD) was used in order to evaluate if there is any other compound other than FeCO_3 which could be identified on the steel surface. The XRD signal has not revealed any pure iron peaks on the sample which has not been exposed to acetic acid (Figure 16a). This does not happen often, as the 110 reflection of α -Fe is strong, suggesting that the iron carbonate layer deposited over the iron surface is rather thick. On the sample where the addition of 1.6mM (100ppm) of undissociated acetic acid caused the steel surface to partially loose some of its iron carbonate crystals, the increase of the main iron peak can be seen (compare Figure 16a to Figure 16b). The experimental

data shows that the main phase (FeCO_3) has a nearly perfect structure, large crystals that provide spots on the 2D-pattern.

Crystalline, semi-crystalline, and amorphous phases are all possibilities in the corrosion product layer. The current XRD analysis can only properly identify crystalline substances such as FeCO_3 , while the semi-crystalline Fe-compounds such as Fe-salts/hydroxides are much harder to pinpoint. The amorphous phase is not detectable with XRD. In summary, the SEM, EDX and XRD analysis used may not have been adequate techniques to help us answer the question posed above. This will be the subject of the next chapter.

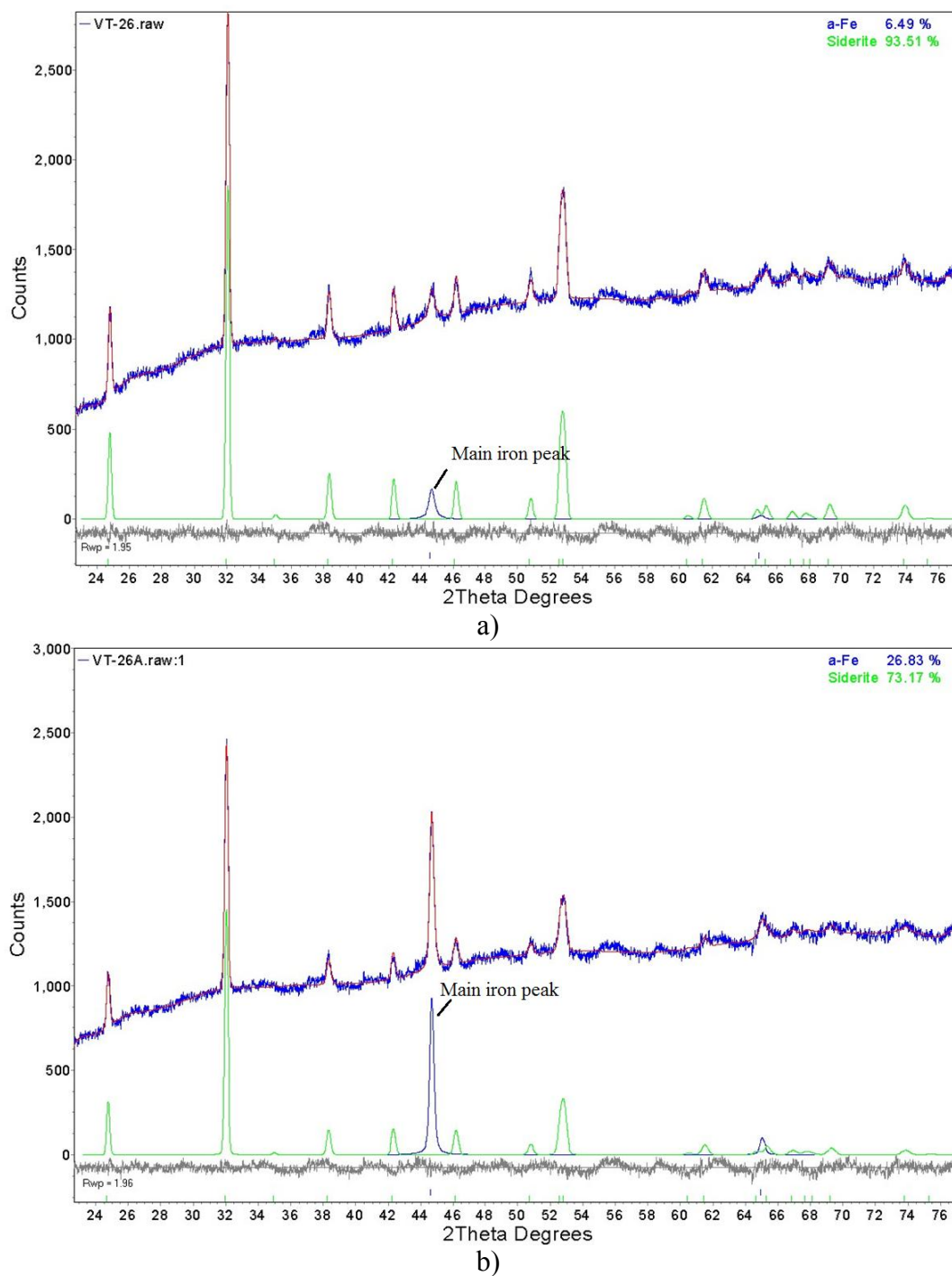


Figure 16. XRD analysis of the layer formed on the steel at pH 6.3, static conditions and 80°C; a) layer formed in pure CO₂ after 96 h, see Figure 13a above and b) layer after addition of 1.6mM of undissociated acetic acid, at the end of the experiment shown in Figure 13b above.

3.3.2. Effect of the flow velocity

The effect that flow may exhibit on the integrity of the iron carbonate layer can manifest itself in different ways [18]. The most obvious pathways involve mechanical effects such as shear stress that can lead to or assist removal of iron carbonate crystals. Another possibility is an increase in the transport of dissolved species between the bulk flow and the steel surface. In the present experiments without acetic acid, an increase in the shear stress was observed to cause a decrease in the density of the iron carbonate layer (see Figure 18a. and Figure 20a). This is supported by the corrosion rate measurements shown in Figure 17 and Figure 19. At an increased rotation speed, the corrosion rate is three times higher than in static conditions. The combined effect of the flow and acetic acid addition increased the final corrosion rate to 0.25mm/y at 100 rpm, and to 0.65mm/y at 1000 rpm. Mechanical removal is suspected since the iron carbonate crystals were removed from over 80% of the entire surface at a high shear stress (Figure 20), with no indication of chemical dissolution of the iron carbonate crystals.

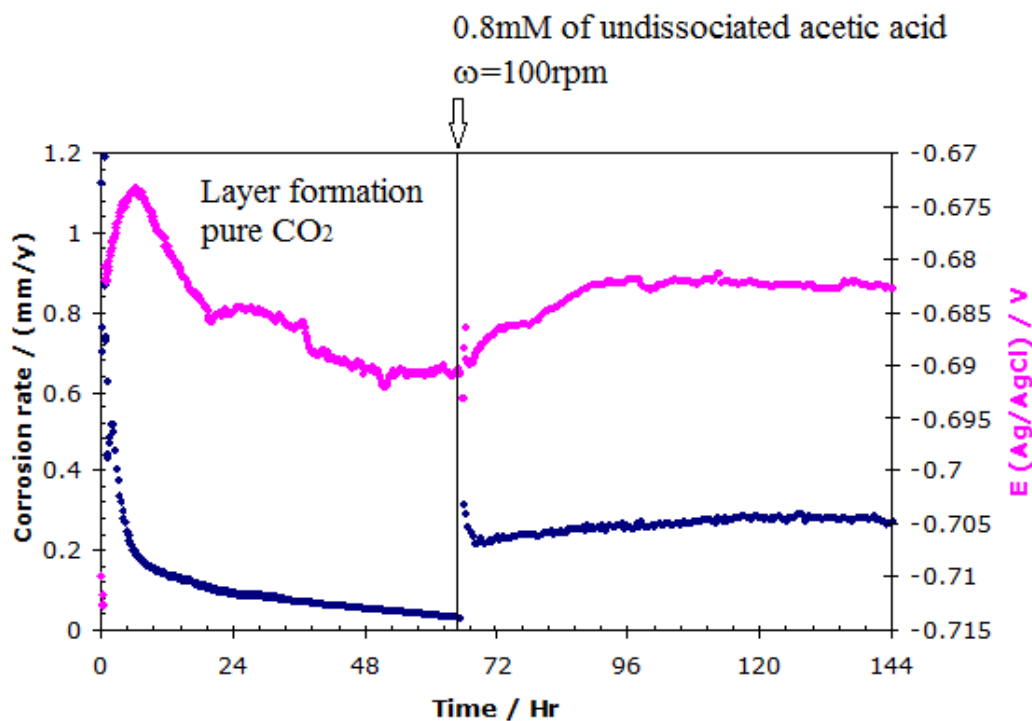


Figure 17. The effect of flow rate on the corrosion rate and corrosion potential of X65 steel during 168 hours of exposure (3wt.% NaCl, 100 rpm, 0.8mM of undissociated acetic acid, pH 6.3, and 80°C).

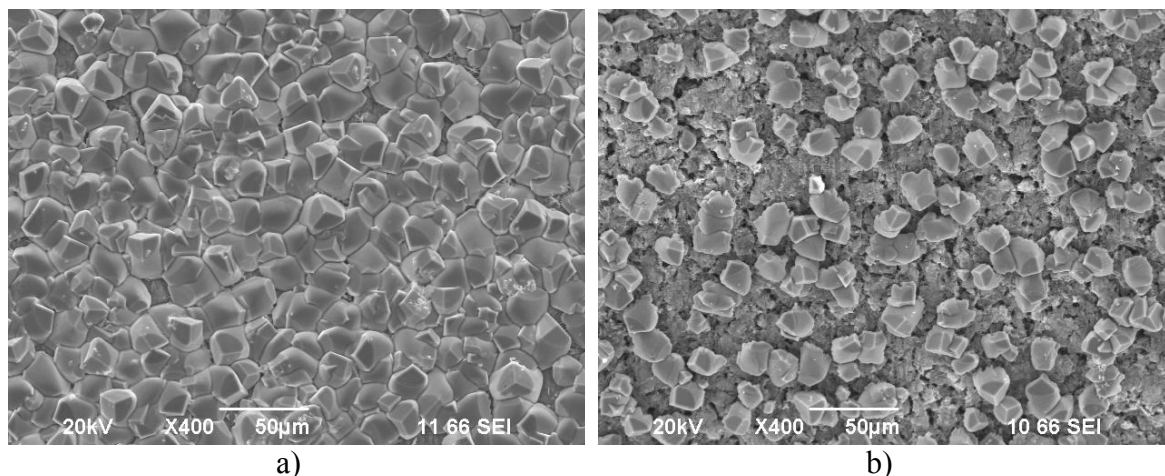


Figure 18. FeCO₃ layer morphology of X65 steel (3wt.% NaCl, pH 6.3, 80°C and 100 rpm). a) Layer formed in pure CO₂ after 67 hours and b) layer after addition of 0.8mM of undissociated acetic acid, appearance at the end of the experiment shown in Figure 17 above.

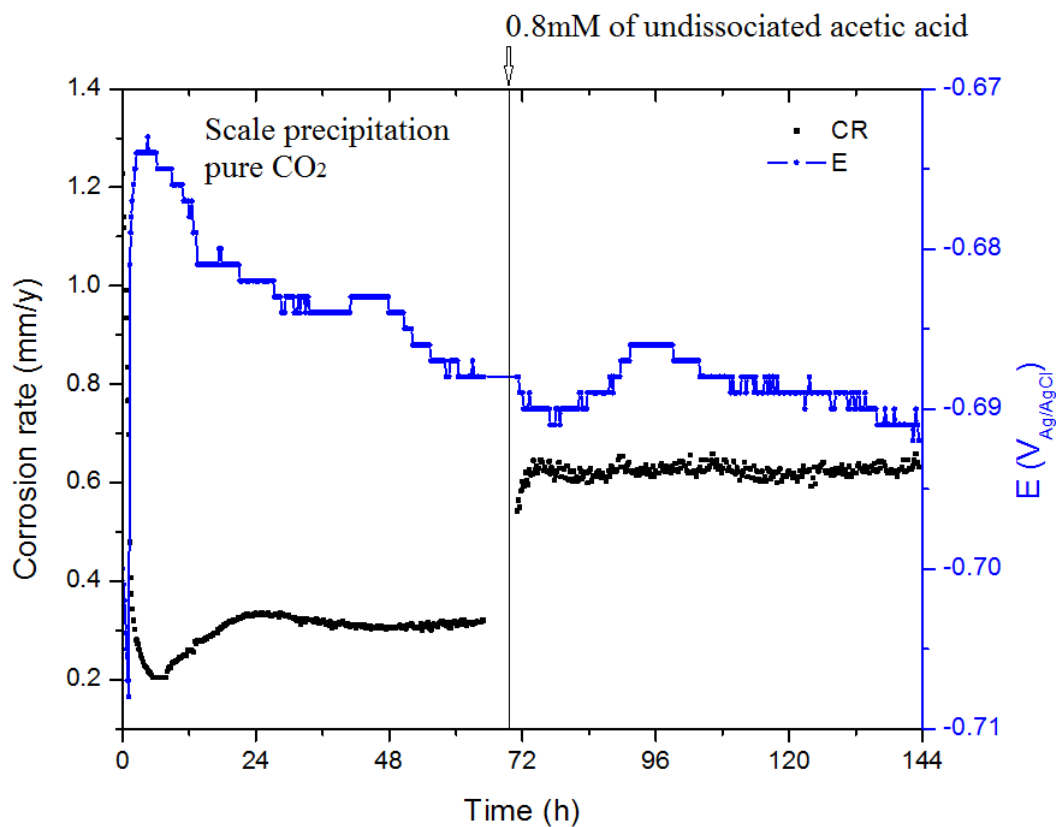


Figure 19. The effect of flow rate on the corrosion rate and corrosion potential of X65 steel during 168 hours of exposure (3wt.% NaCl, 1000 rpm, 0.8mM of undissociated acetic acid, pH 6.3, $p\text{CO}_2=0.53\text{bar}$, and 80°C).

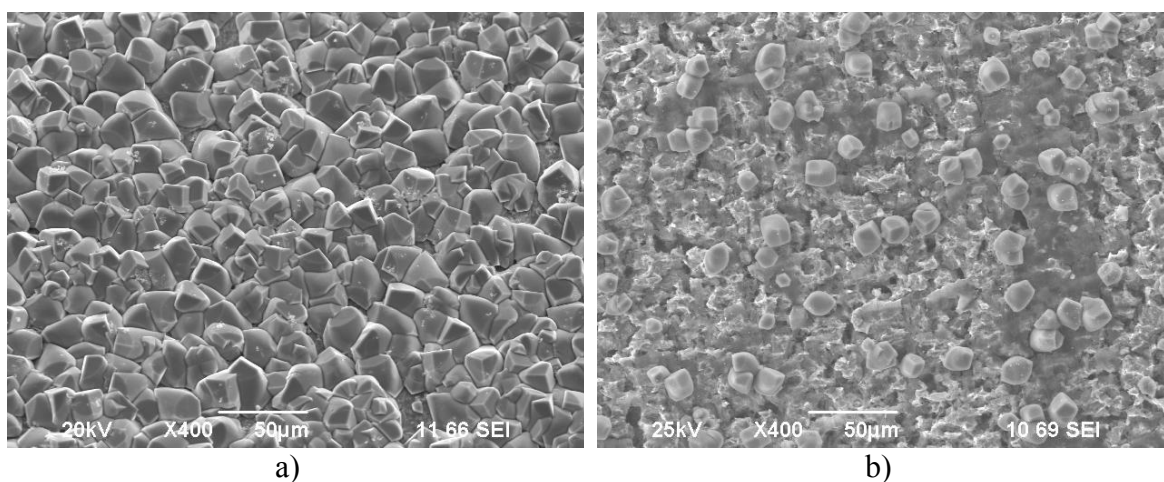


Figure 20. FeCO_3 layer morphology of X65 (3wt.% NaCl, pH 6.3, 80°C and 1000 rpm). a) Layer formed in pure CO_2 after 70 hours and b) layer after addition of 0.8mM of undissociated acetic acid, appearance at the end of the experiment shown in Figure 19 above.

3.3.3. Effect of the pH

It was thought that a slight decrease of pH from 6.3 to 6.0, which would be allowed during the addition of acetic acid, might help elucidate the problem. The decrease of pH affects the concentration of species in the electrolyte and in this particular case it forces the conversion of acetate into acetic acid and the solution becomes more aggressive (Figure 21). At the same time, the saturation level for iron carbonate decreases with the drop in pH.

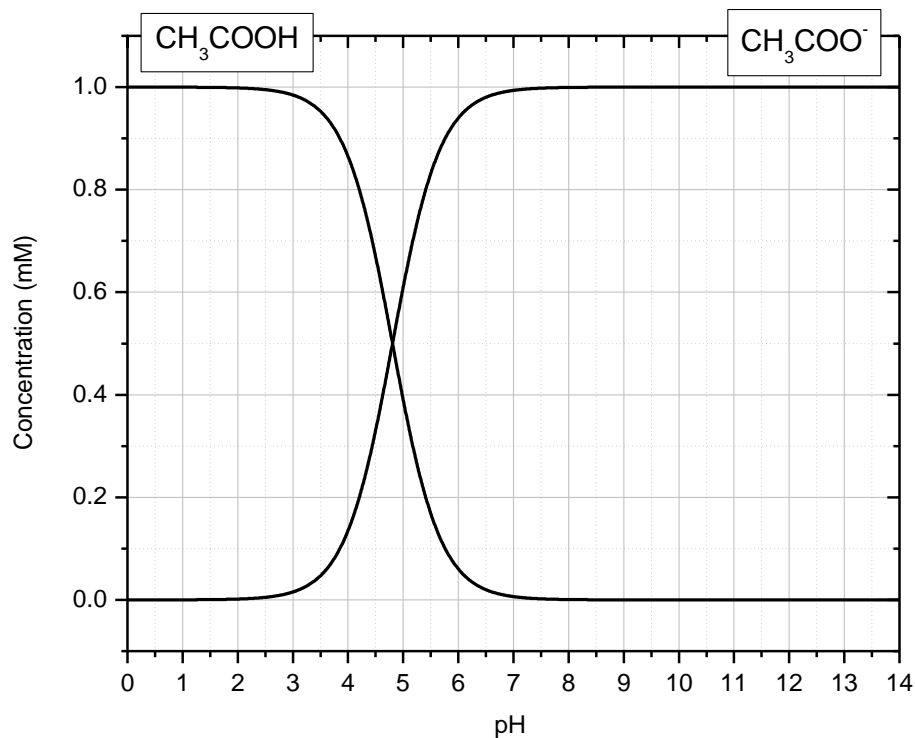


Figure 21. Distribution of species CH₃COOH (pK_a 4.86) and CH₃COO⁻ at 80°C.

The analysis of the steel surface from this experiment reveals that the surviving iron carbonate layer had even fewer crystals when compared to the equivalent experiment conducted at a slightly higher pH 6.3 (compare Figure 12b and Figure 23b). However,

this did not seem to have any effect on final corrosion rate (see Figure 22 and compare to Figure 10).

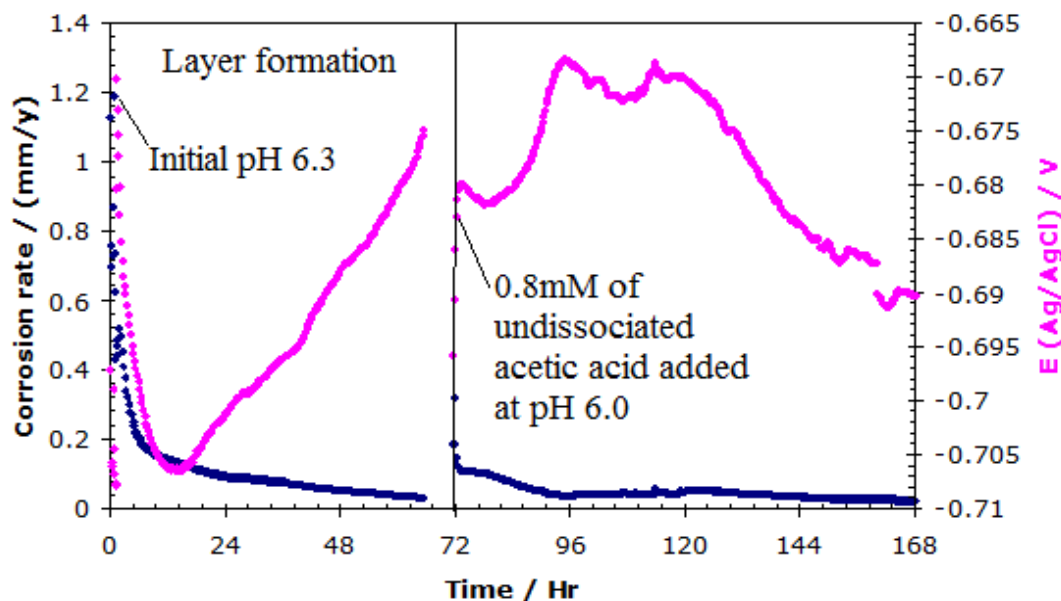


Figure 22. The effect of pH on the corrosion rate and corrosion potential of X65 steel during 168 hours of exposure (3wt.% NaCl, 0.8mM of undissociated acetic acid, $p\text{CO}_2=0.53$ bar, static conditions, and 80°C).

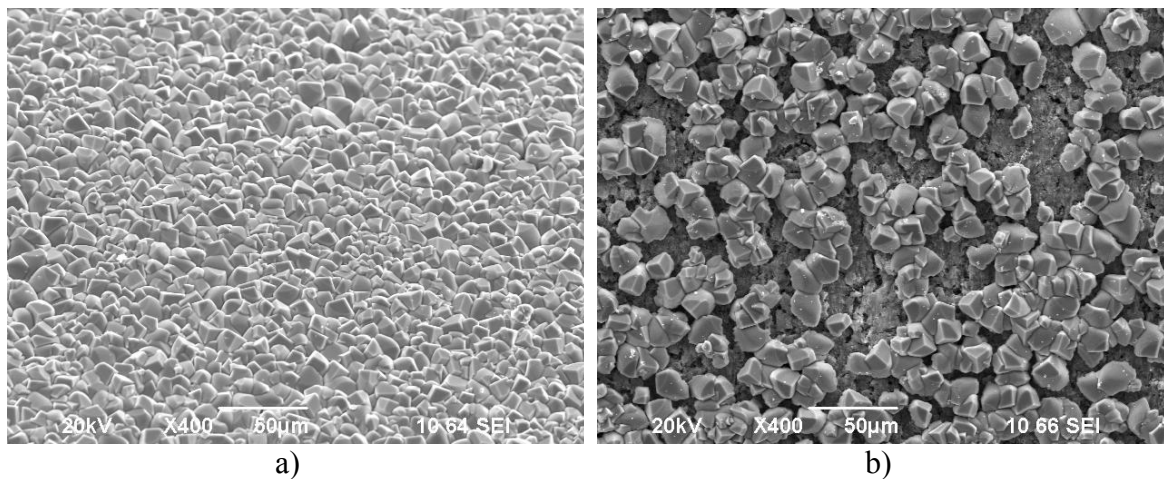


Figure 23. FeCO_3 layer morphology of X65 steel ($p\text{CO}_2=0.53$ bar, static conditions and 80°C). a) Layer formed in pure CO_2 after 72 hours and b) layer after addition of 0.8mM of undissociated acetic acid, appearance at the end of the experiment shown in Figure 22 above.

3.4 Summary

It was found that the presence of acetic acid may damage the protective iron carbonate layer formed on mild steel. This leads to a temporary increase in the corrosion rate. In spite of this fluctuation, the final corrosion rate does not seem to be affected. It remains unclear how the very porous iron carbonate films that survive the attack by the acetic acid continued to protect the underlying steel. This behavior will be discussed in the next chapter.

CHAPTER 4: CHARACTERIZATION OF THE CORROSION PRODUCT LAYER

Based on the previous study, the presence of acetic acid may lead to damage of the protective iron carbonate layer formed on mild steel. This leads directly to a temporary increase in the corrosion rate. However, the final corrosion rate does not seem to be affected. It remains unclear how the very porous iron carbonate layer that survives the attack of acetic acid continues to protect the underlying steel. This raises the possibility that there may be a different phase on the steel surface, conferring protection, which was not detected. This research sought to identify this “mysterious” phase by characterizing the corrosion layer using different analytical techniques (SEM, EDS, FIB/TEM/EDS, XRD and XPS). A multi-pronged analytical approach will provide a more complete picture of the species found on the steel surface.

4.1 Objective

To determine the species that offer protection to the exposed steel surface area after the iron carbonate has been partially removed by acetic acid.

4.2 Experimental method

Selected experiments (Table 12) were repeated in order to obtain more information about the corrosion product with and without the addition of acetic acid. The experimental procedure was the same as presented in Chapter 3. The corrosion product layer was closely examined using different surface techniques, such as scanning electrode microscopy (SEM), energy-dispersive X-ray spectroscopy (EDS), X-ray photoelectron

spectroscopy (XPS), and focused ion beam/transmission electron microscopy/ energy-dispersive X-ray spectroscopy (FIB/TEM/EDS).

Table 12. Experimental conditions – iron carbonate precipitation

Test solution	Deionized water + 1wt.%NaCl
Test material	X65 steel
Temperature	80°C
Total pressure of CO_2	0.53 bar
Undissociated (free) organic acid	3mM
pH	6.3
Rotation velocity	Static conditions
Initial supersaturation	200
Sweep rate	0.1 mV/s to 0.2 mV/s
Polarization resistance	From -5mV to 5mV (vs E_{oc})
AC Impedance	$\pm 5mV$ vs. E_{oc} from 1mHz to 100KHz

4.3 Results and discussion

A detailed surface analysis approach was sought in these experiments in order to determine the nature of the thin layer remaining after the action of the acetic acid. The first step was carried out using SEM and EDS to provide the morphology and the elemental analysis of the layer formed on the steel surface before and after acetic acid was added to the bulk solution. The SEM showed a partial removal of the $FeCO_3$ (Figure 24). The EDS analysis of the exposed substrate showed lower intensity peaks of Fe, O and C, constituent elements that form $FeCO_3$, compared with the EDS done on the prismatic crystals (Figure 24). However, this elemental analysis is not conclusive since it is not possible to identify the exact chemical composition of the compound. It is easy to misinterpret the results based only on the ratios of atomic weight percent provided by EDS.

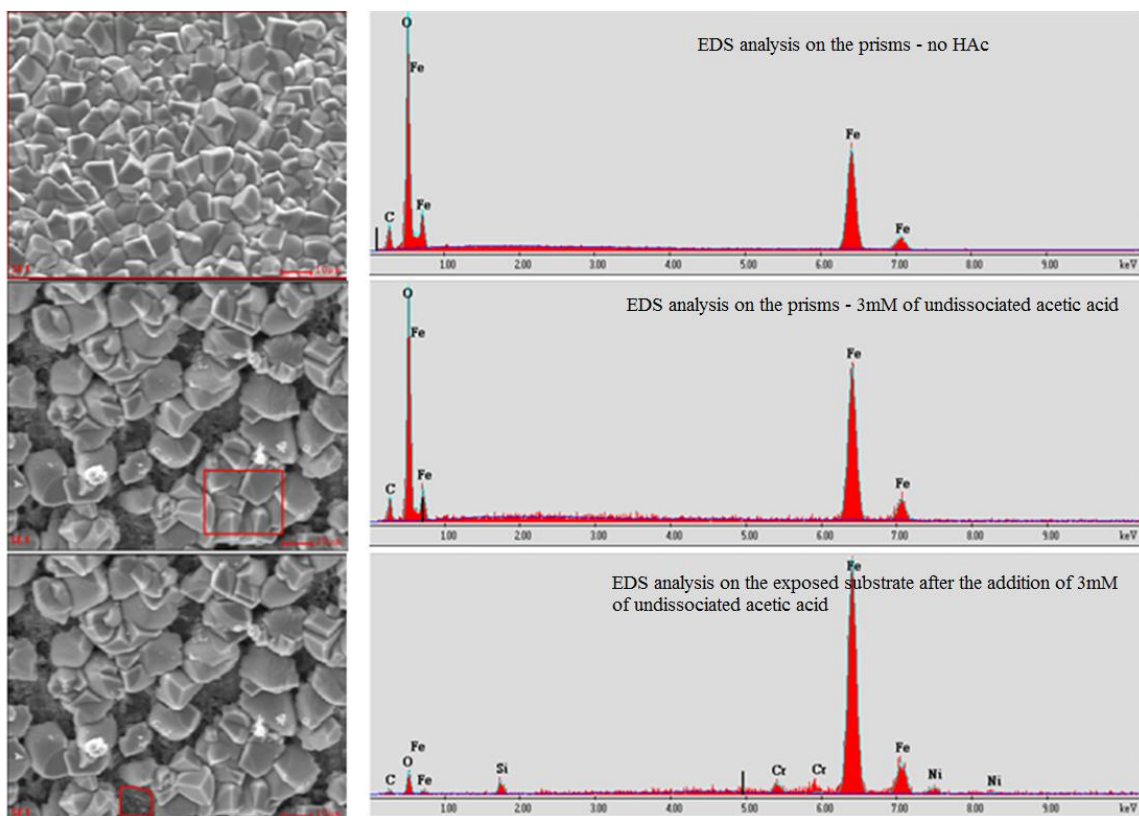
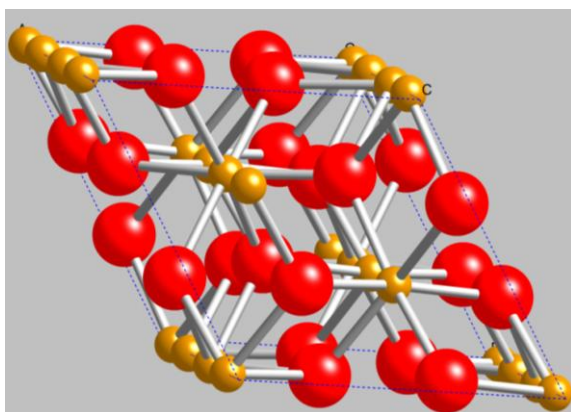


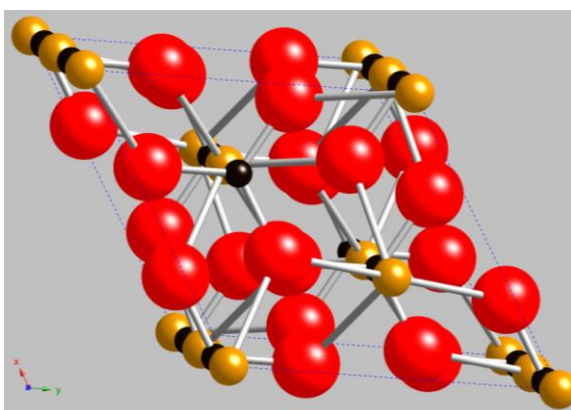
Figure 24. EDX analysis before and after the addition of 3mM of undissociated acetic acid (static conditions and 80°C).

Based on the known aqueous chemistry in these experiments, it could be possible to have cementite (Fe_3C), siderite (FeCO_3), hematite (Fe_2O_3), magnetite (Fe_3O_4) and various forms of iron hydroxide, on the steel surface. In order to distinguish between these possible compounds, additional analyses had to be conducted. Using transmission electron microscopy (TEM) it is possible to obtain electron diffraction (ED) data. The generated diffraction pattern is unique to the crystal structure of the compound or element present in characterized solid phases and depends solely on the geometry and symmetry of the unit cell [34, 35]. Small areas can be selected for acquisition of diffraction data down to a length scale of 300nm. The rings obtained from the diffraction data provide the

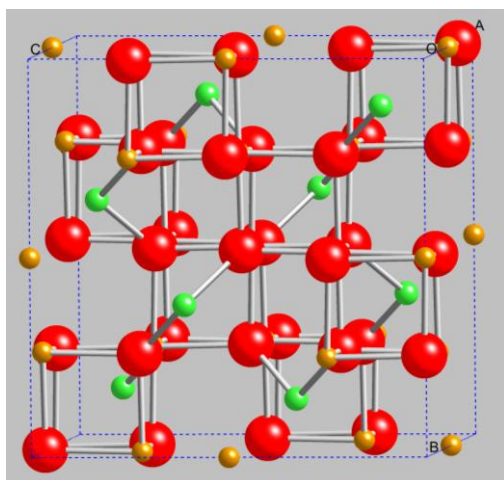
d-spacings for each unique phase: pure element or compound. For the purpose of this study, it is important to determine the crystal structure of the thin layer formed on the steel, since hematite and siderite share the same hexagonal unit cell type and have certain similarities in their diffraction patterns as shown in Figure 25. As magnetite is a cubic structure, as shown in Figure 25, it will be easy to distinguish from other possible phases if it is present in the system.



Hematite (Fe_2O_3)
Hexagonal crystal system
 \underline{a} : 5.038Å, \underline{c} : 13.772Å [36]



Siderite (FeCO_3)
Hexagonal crystal system
 \underline{a} : 4.694Å, \underline{c} : 15.386Å [37]



Magnetite[‡] (Fe_3O_4)
Cubic crystal system
 \underline{a} : 8.396Å [38]

Figure 25. Unit cells of hematite, siderite and magnetite (\underline{a} and \underline{c} = unit cell edges).

[‡] This is a spinel-type (MgAl_2O_4) structure with Fe^{2+} and Fe^{3+} occupying different positions within the lattice, in analogy to Mg^{2+} and Al^{3+}

Diffraction data from the International Center for Diffraction Data (ICDD) show that the highest intensity peaks for hematite and siderite are found very close to each other with d-spacings of 2.703 and 2.795 Å, respectively, as shown in Figure 26 and Table 13.

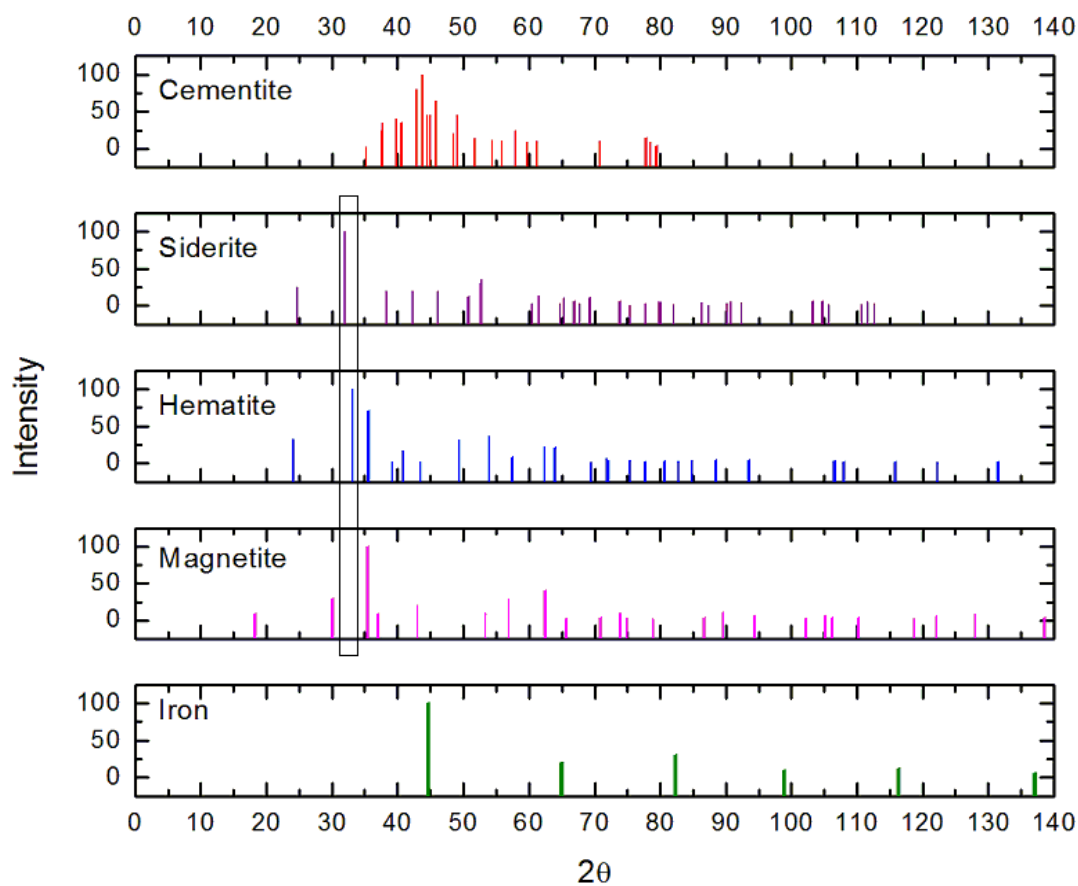


Figure 26. XRD analysis of possible compounds found on the steel surface with $\lambda = 1.54056 \text{ \AA}$ (Source: ©2010 International Centre for Diffraction Data).

Table 13. d–Spacings with $\lambda = 1.54056(\text{\AA})$ (Source: ©2010 International Centre for Diffraction Data)[§]

Iron		Magnetite		Hematite		Siderite		Cementite	
$d(\text{\AA})$	Intensity								
2.027	100	4.852	8	3.686	33	3.593	25	2.547	2
1.433	20	2.967	30	2.703	100	2.795	100	2.387	25
1.170	30	2.532	100	2.519	70	2.564	<1	2.381	35
1.013	10	2.424	8	2.295	2	2.346	20	2.264	40
0.906	12	2.099	20	2.208	17	2.134	20	2.219	35
0.828	6	1.715	10	2.080	2	1.965	20	2.108	80
		1.616	30	1.843	31	1.797	12	2.068	100
		1.485	40	1.697	36	1.738	30	2.032	45
		1.419	2	1.601	8	1.732	35	2.014	45
		1.328	4	1.601	8	1.529	3	1.978	65
		1.281	10	1.487	22	1.506	14	1.873	20
		1.266	4	1.454	21	1.439	3	1.854	45
		1.212	2	1.351	2	1.427	11	1.764	14
		1.122	4	1.313	7	1.397	6	1.685	12
		1.093	12	1.308	4	1.382	3	1.685	12
		1.050	6	1.260	4	1.355	11	1.642	10
		0.990	2	1.229	2	1.282	5	1.590	25
		0.970	6	1.191	3	1.259	1	1.547	8
		0.963	4	1.191	3	1.227	3	1.512	10
		0.939	4	1.165	3	1.200	5	1.330	10
		0.895	2	1.142	4	1.198	4	1.330	10
		0.880	6	1.104	4	1.174	2	1.226	14
		0.857	8	1.057	4	1.125	4	1.217	8
		0.823	4	0.961	3	1.115	1	1.205	4
		0.812	6	0.960	3	1.087	3		
		0.808	4	0.952	2	1.082	5		
				0.909	2	1.067	4		
				0.879	2	0.983	5		
				0.845	2	0.972	5		
				0.845	2	0.967	2		
						0.936	2		
						0.931	6		
						0.926	3		

[§] For conversion to 2θ angle, Bragg's law should be applied ($n\lambda = 2d \sin \theta$)

Thus, it is clear that a single analytical technique such as EDS does not provide enough information about any compound formed on the surface for adequate identification. The electron diffraction data in conjunction with the XRD provide the best accuracy for the detection and identification of compounds in local areas on sample surfaces. The positions and intensities of an element's or a compound's XRD peaks or ED spots from an analyzed crystal are related to reflections from the lattice planes encountered [34] as shown in Figure 27.

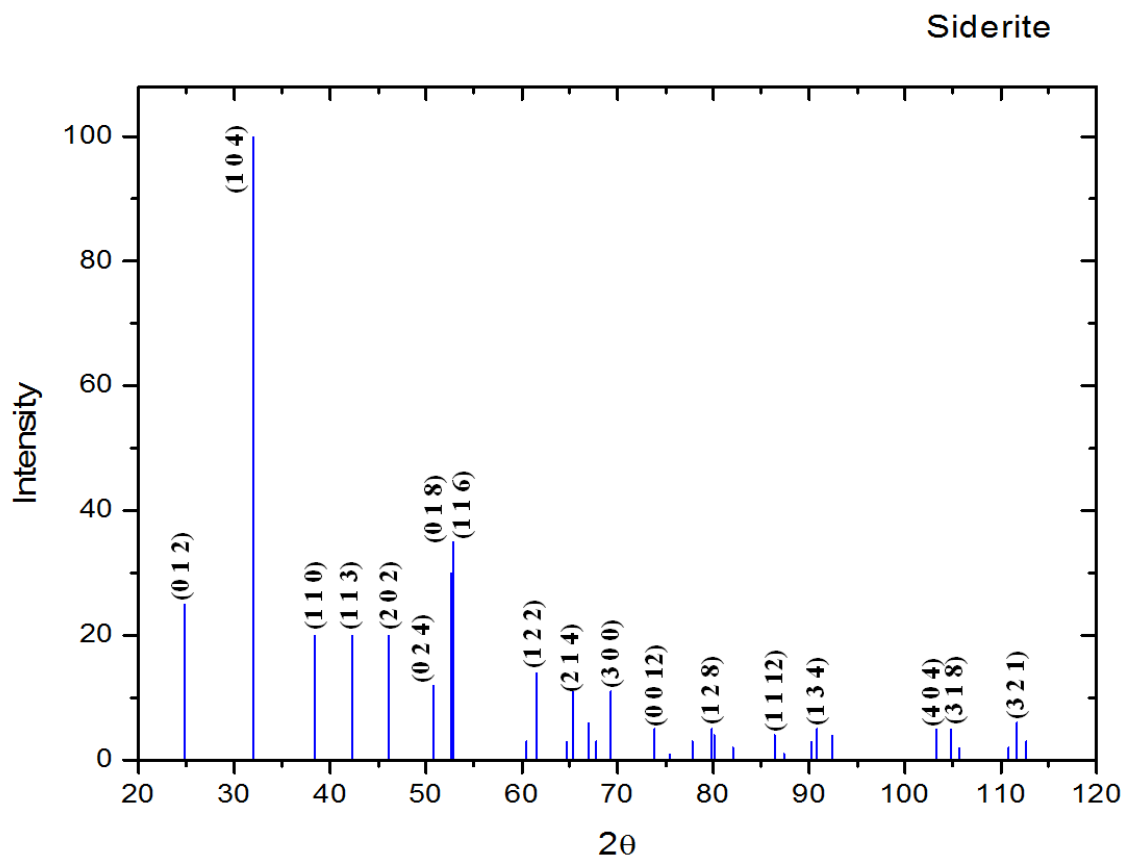


Figure 27. XRD analysis of iron carbonate (Source: ©2010 International Centre for Diffraction Data).

To relate the XRD data with the electron diffraction pattern it is necessary to conduct FIB/TEM analyses of the samples. The focus ion beam (FIB) mills the sample to

nanometers as shown in Figure 28. Then, the transmission electron microscopy (TEM) provides an image of the crystal structure down to the crystal lattice, providing the diffraction data.

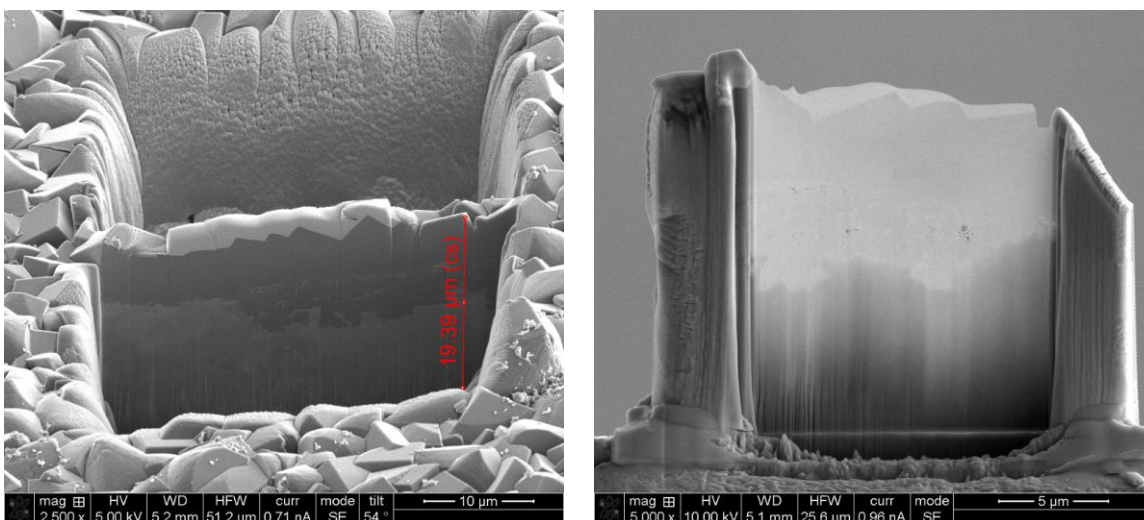


Figure 28. FIB** images of iron carbonate plates formed on X65 mild steel.

The samples were analyzed using TEM/EDS techniques for the precipitation and dissolution processes. In the precipitation process, both plates and prisms of iron carbonate formed. Even though the morphology of the precipitates is different, the TEM/EDS showed that both were iron carbonate (Figure 29 and Figure 31). Electron diffraction data confirmed this assumption (Figure 30 and Figure 32). The Bragg reflections (interplanar spacing d_{hkl}) obtained from the lattice planes for the plates are: $R_1[1\ 1\ 2]$, $R_2[1\ 0\ 4]$, $R_3[1\ 1\ 0]$ and $R_4[0\ 1\ 2]$, which correspond to some of the major peak intensities of iron carbonate according to XRD data from the ICDD. Every d-

** The FIB/TEM/EDS analyses were conducted by Dr. Amir Avishai in the Department of Material Science and Engineering in CASE Western University.

spacing has a corresponding XRD 2θ value and hkl planes (Figure 27), which further confirms the type of compound present on the surface. For every electron diffraction pattern, d-spacing was calculated using $\lambda L = 1.935 \text{ \AA cm}$.

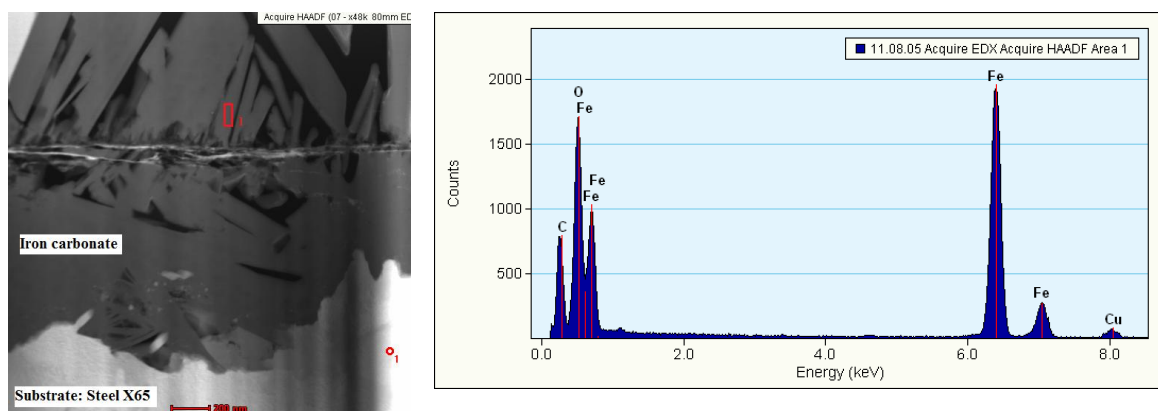


Figure 29. TEM image and EDS analysis of iron carbonate plates formed on X65 mild steel.



Figure 30. TEM image and ED data^{††} of the plates found on the X65 mild steel before the addition of undissociated acetic acid.

^{††} The electron diffraction (ED) data was conducted by Dr. Martin Kordesch in the Department of Physics and Astronomy at Ohio University.

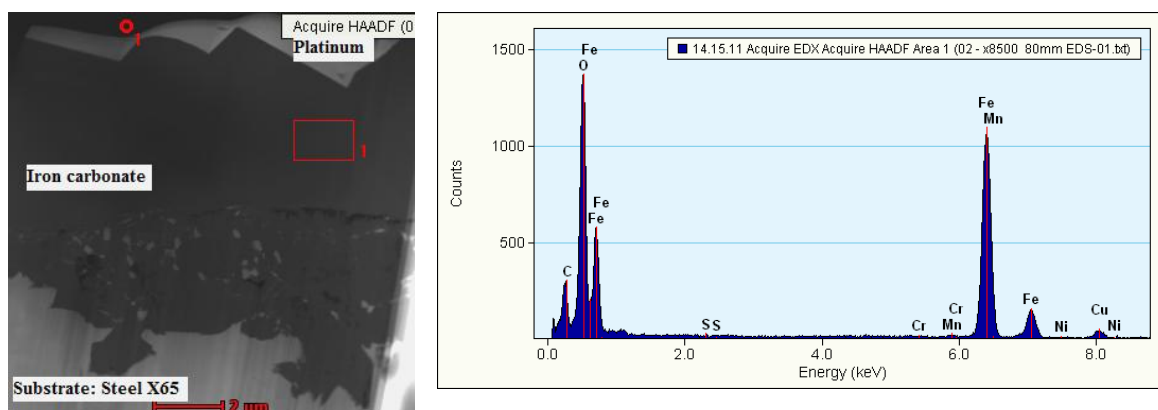


Figure 31. TEM image and EDS analysis of iron carbonate prisms formed on X65 mild steel.

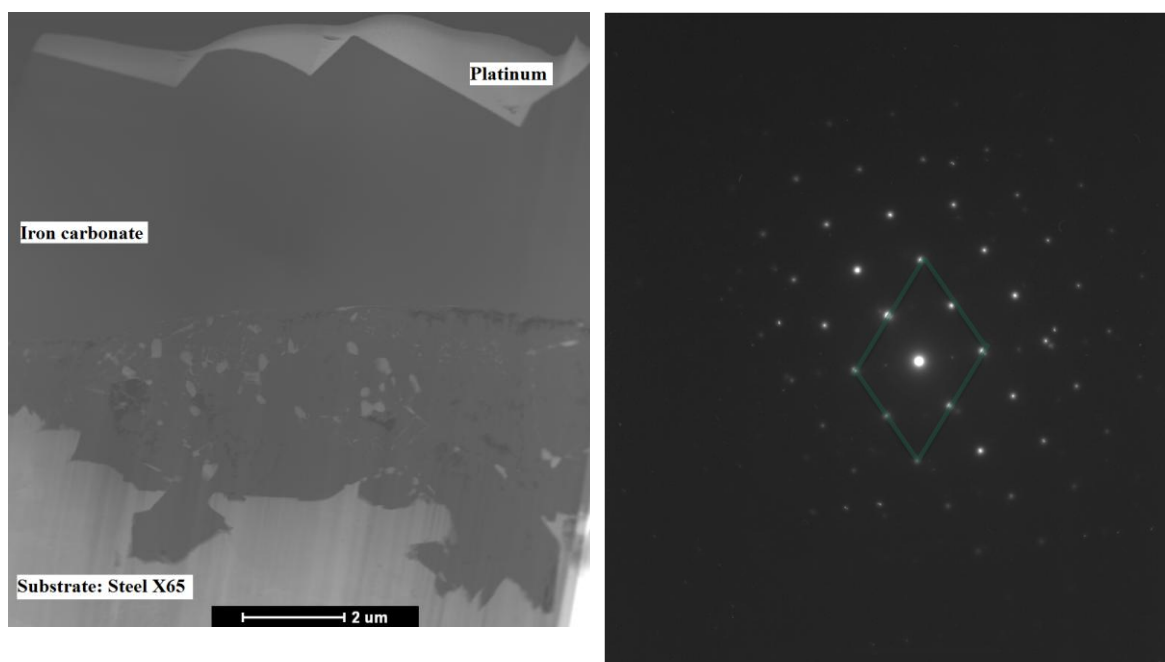


Figure 32. TEM image and ED data of the prisms found on the X65 mild steel before the addition of undissociated acetic acid.

After the dissolution process by the addition of 3mM of undissociated acetic acid, only prisms of iron carbonate remained on the steel surface. The electron diffraction patterns of the prism found on the X65 steel showed the hexagonal shape. The d-spacing

corresponded to those of siderite (Figure 33). Although the morphology of the exposed substrate looks amorphous, it is possible that the scale remaining on the steel surface is an agglomeration of nanocrystals. This may be explained by the electron diffraction pattern for the powder formed in the bulk solution is shown in Figure 34. The sizes of the intergrown nanocrystals are of the order of $\sim 58\text{nm}$ ($0.05\mu\text{m}$). Agglomeration of such nanocrystals may resemble an amorphous phase when observed at higher magnifications. The ED data is consistent with FeCO_3 .

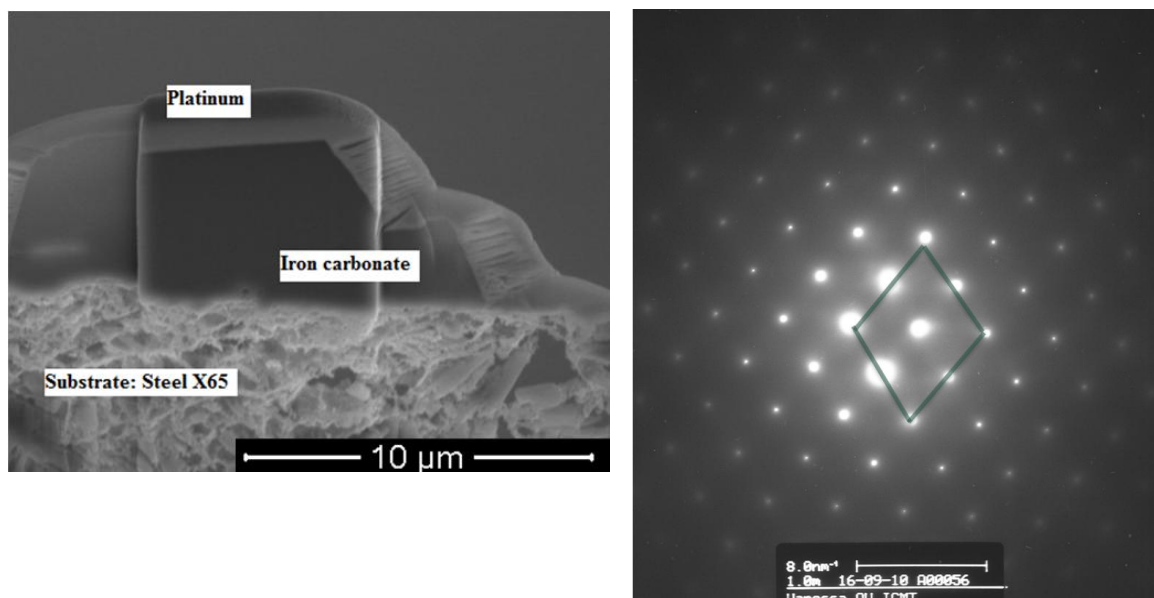


Figure 33. TEM image and ED data of the prism found on the X65 mild steel after the addition of undissociated acetic acid.

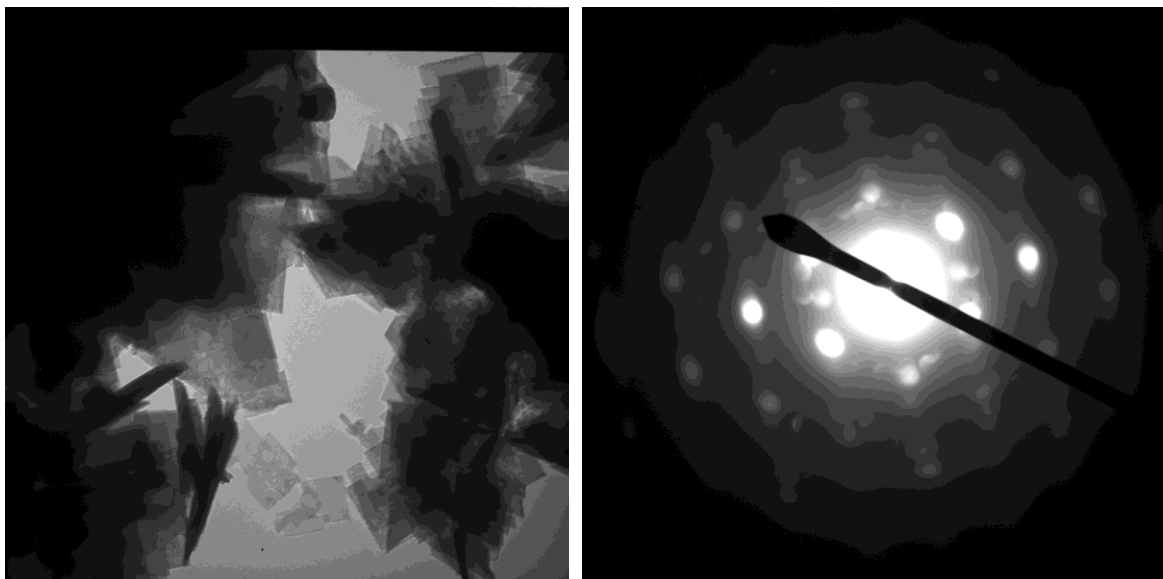


Figure 34. FeCO_3 nanocrystals and ED data.

In addition, XPS was utilized to confirm the results obtained from the other techniques. Figure 35 shows the XPS scans of the iron carbonate scale formed on X65 steel which matches the theoretical binding energy for FeCO_3 [39].

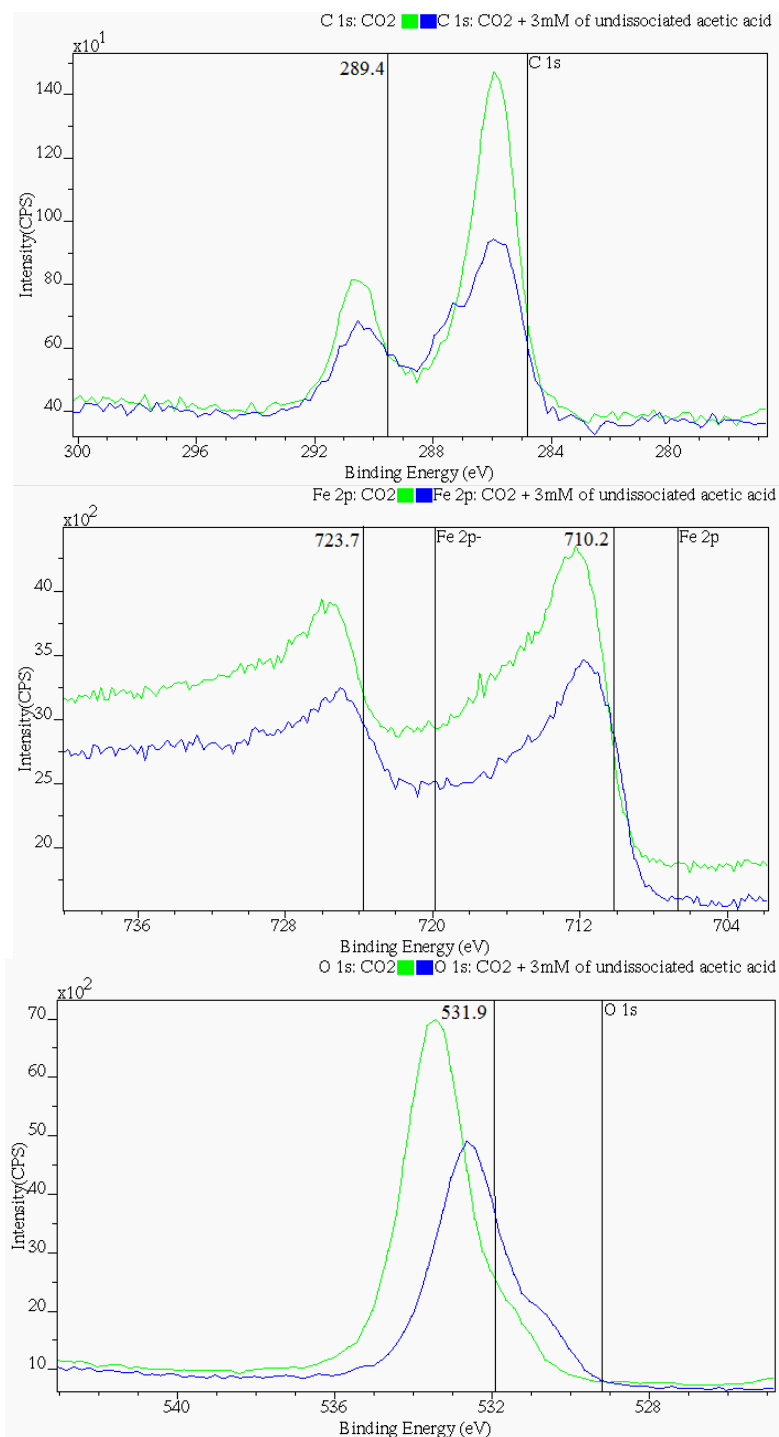


Figure 35. XPS^{‡‡} scans of iron carbonate dissolution on X65 steel in the presence of acetic acid (80°C, 0.1 wt.% NaCl, and pCO₂=0.53 bar).

^{‡‡} The XPS analyses were conducted by Dr. David Ingram in the Department of Physics and Astronomy at Ohio University.

4.4 Summary

The presence of acetic acid, at a constant pH, partially removed the iron carbonate layer. However, the protection stayed, because part of the FeCO_3 remained on the surface. This iron carbonate is a very thin surface layer of intergrown nanocrystals. Several surface analyses methods have proven this hypothesis (SEM, EDS, XRD, XPS, FIB/TEM/EDS and ED data).

**CHAPTER 5: STUDY OF THE SOLUBILITY OF IRON CARBONATE IN THE
PRESENCE OF ACETIC ACID USING THE ELECTROCHEMICAL
QUARTZ CRYSTAL MICROBALANCE**

5.1 Introduction

It was shown in the previous chapter that due to the action of acetic acid some iron carbonate was lost from the steel surface. This loss can happen for one of the two following reasons:

- a) Undermining – Acetic acid diffuses through the pores of the layer and directly attacks the steel underneath resulting in loss of the FeCO_3 adherence, or
- b) Selective dissolution of iron carbonate – It is possible that the acetic acid has a preference for certain crystal morphologies that it can more easily dissolve.

The loss of the FeCO_3 was only detected after the completion of the experiments and the steel samples were analyzed using a range of techniques. In order to determine the nature of this loss, it was deemed beneficial to make use of an *in situ* mass loss detection device, which was readily available in the lab: the quartz crystal microbalance. Several sets of experiments were conducted with it, in order to quantitatively evaluate the solubility of an iron carbonate scale in the presence of acetic acid, *in situ*. The first set of experiments was designed to determine the influence of the pH on the iron carbonate precipitation in the absence of acetic acid. The second set of experiments were carried out with three different undissociated acetic acid concentrations, 1, 3, and 5mM at pH 6.0 and 80°C to study the solubility of the iron carbonate layer. The acetic acid was added into

the system as a buffered acetic acid solution after a protective iron carbonate layer formed as indicated by a stable mass detected by the EQCM.

5.2 Objective

To study and quantify the solubility of the iron carbonate layer in the presence of acetic acid *in situ*, using the electrochemical quartz crystal microbalance (EQCM).

5.3 Experimental method

A three-electrode setup was used in all the experiments (Figure 36). A platinum coated quartz crystal was used as the working electrode (WE). Platinum wire was used as a counter electrode (CE) with a saturated silver-silver chloride (Ag/AgCl) as a reference electrode (RE). The glass cell was filled with 2 liters of 0.1 wt.% NaCl electrolyte and heated to 80°C (pH was adjusted to 6.0 with NaHCO₃). In all experiments, CO₂ was continuously bubbled through the electrolyte for approximately 1 hour before the experiment and during the entire experiment. The platinum coated crystal was polarized to -700mV to mimic the corrosion potential of iron and to facilitate the iron carbonate precipitation. The platinum coated crystal was the key element in these experiments, because being a noble metal the platinum does not corrode, making it possible to measure the mass gain and loss of the iron carbonate layer. Moreover, this could be done without any interference by corrosion of the underlying steel. Although the purpose of this study is to quantify the solubility of the iron carbonate layer on iron, it was decided not to use iron coated crystal for several reasons: 1) the thickness of the iron coated crystal is around 1µm and therefore would corrode away before the precipitation process was complete; 2) the surface of the vapor deposited iron surface was too smooth

which inhibited the nucleation process that precedes any crystal growth during precipitation; and 3) it is not possible to differentiate the mass lost from the corrosion process and that lost as a result of dissolution by the acetic acid, as both processes occur simultaneously.

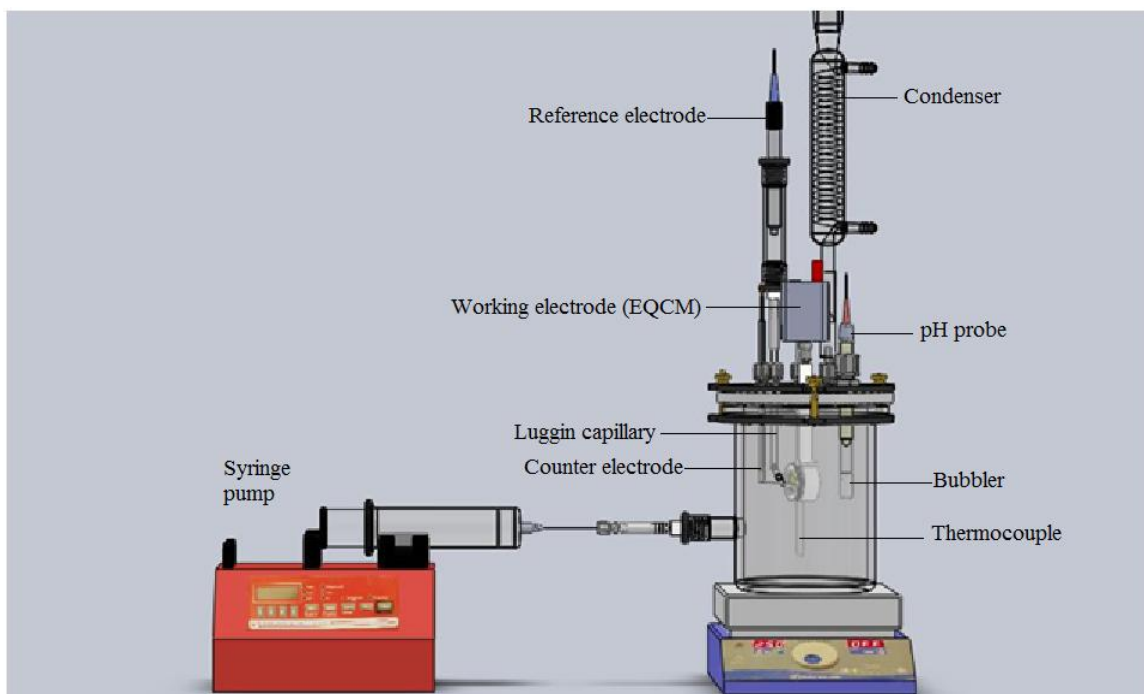


Figure 36. Experimental cell design to measure of the solubility the iron carbonate layer.

Several sets of experiments were conducted to evaluate the solubility of the iron carbonate layer in the presence of acetic acid using the electrochemical quartz cell microbalance (EQCM). Surface analyses were performed with scanning electrode microscopy (SEM), energy-dispersive X-ray spectroscopy (EDX/EDS), Raman spectroscopy and X-ray photoelectron spectroscopy (XPS). See appendix III for further information about the data provided by these techniques.

The first set of experiments was designed to determine the influence of the pH on the iron carbonate precipitation in the absence of acetic acid (Table 14). The second set of experiments were carried out with three different undissociated acetic acid concentrations, 1, 3, and 5mM at pH 6.0 and 80°C to study the solubility of the iron carbonate layer (Table 15). The acetic acid was added into the system as a buffered acetic acid solution (to avoid a change in pH) after a protective iron carbonate layer formed as indicated by a stable mass detected by the EQCM and with a supersaturation close to 10. For the first set of experiments, an initial FeCO₃ supersaturation of 300 was achieved by FeCl₂ addition. For the second set of experiments the supersaturation was 200.

Table 14. Experimental conditions – Iron carbonate precipitation on polarized (-700mV) platinum coated quartz crystal at different pH values

Test solution	Deionized water + 0.1 wt% NaCl
Test material	Platinum coated quartz crystal
Temperature	80°C
Total pressure of CO ₂	1 bar
Undissociated organic acid	None
Initial pH	6.6, 6.3, 6.0
Rotation velocity	Static conditions

Table 15. Experimental conditions – Iron carbonate dissolution on polarized (-700mV) platinum coated quartz crystal

Test solution	Deionized water + 0.1 w.t% NaCl
Test material	Platinum coated quartz crystal
Temperature	80°C
Total pressure of CO ₂	1 bar
Undissociated (free) organic acid	1, 3 and 5mM
Initial pH	6.0
Rotation velocity	Static conditions

5.4 Result and discussions

5.4.1. *Iron carbonate precipitation*

The first set of experiments sought to determine if the pH has any influence on the iron carbonate precipitation. The unpolished platinum coated crystal was used as a working electrode to avoid corrosion and to focus on the change in mass per unit area measured by the quartz cell microbalance (QCM). It is well known that higher values of pH, temperature and supersaturation favor the formation of iron carbonate on iron. But, since it was decided to use a platinum substrate, instead of iron, it was important to reevaluate all the factors that could affect the iron carbonate precipitation. Figure 37 shows the iron carbonate precipitation on a polarized platinum coated crystal for the three different values of pH. The gain in mass measured by the quartz crystal microbalance for pH 6.6, 6.3 and 6.0 is 1.6, 1.5 and 1.7mg·cm⁻², respectively. The drop in pH and supersaturation during these three experiments is to be expected, due to the formation of the iron carbonate layer (Table 16).

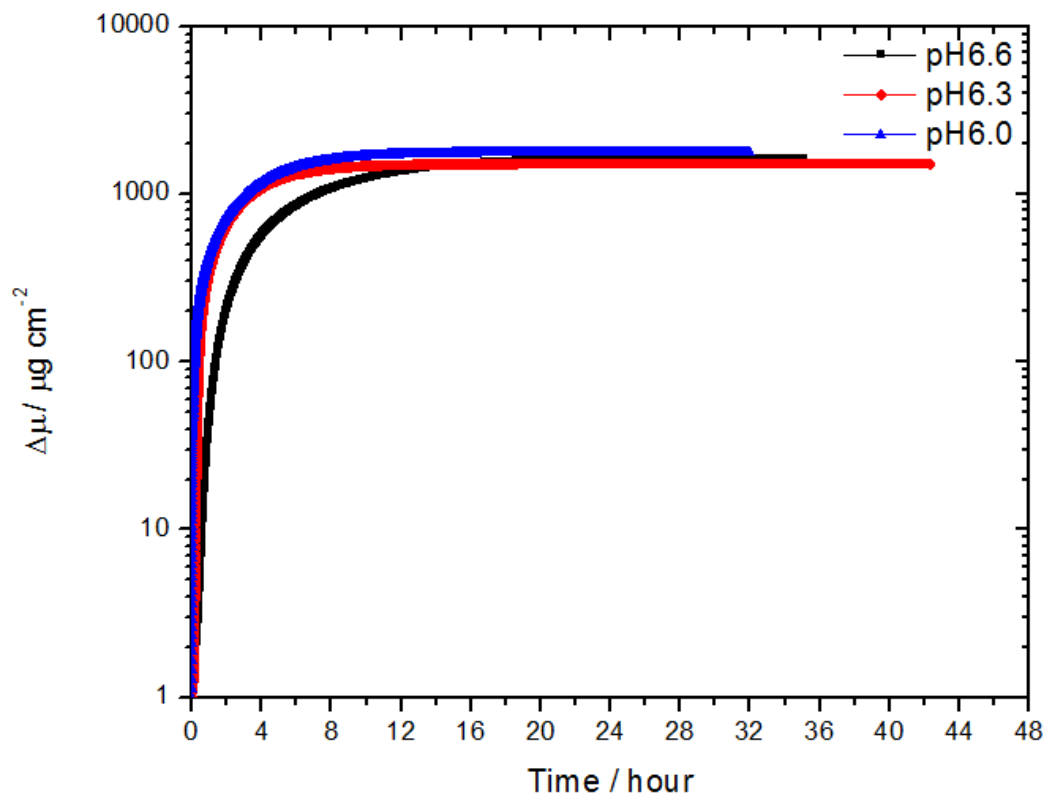


Figure 37. Iron carbonate precipitation on polarized (-700mV) platinum coated quartz crystal at different pH values (80°C, 0.1wt.% NaCl and $p\text{CO}_2=0.53$ bar).

Table 16. Experimental results of the iron carbonate precipitation on polarized (-700mV) platinum coated quartz crystal from Figure 37

pH		Fe^{2+} /ppm		SS		Δm / $\mu\text{g cm}^{-2}$	
I	F	I	F	I	F	I	F
6.6	6.58	32	1.51	300	12.8	0	1620
6.3	5.98	126	9	300	5.12	0	1523
6.0	5.38	547	506	300	16	0	1757

I: initial data

F: final data

The SEM images (Figure 38) show either plates or prisms of iron carbonate depending on pH. pH 6.6 shows well packed prisms, while at pH 6.3 there is a combination of prisms and plates. However, at pH 6.0 only plates were observed. Figure

39 shows the EDS analysis of the layer formed on the platinum crystal. The analysis shows the peaks of Fe, O, and C, consistent with the formation of FeCO_3 .

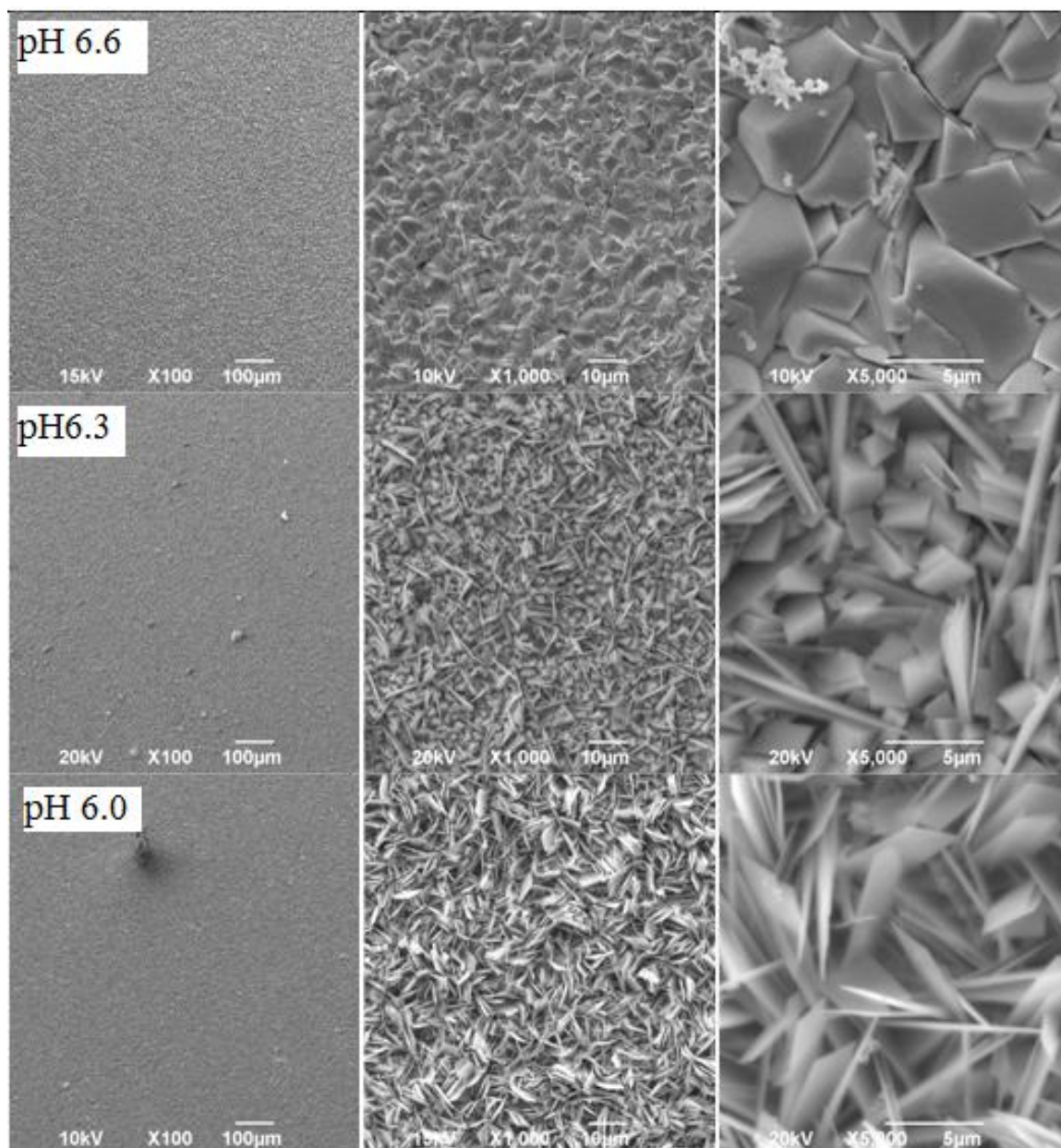


Figure 38. SEM image of iron carbonate layer formed on polarized (-700mV) platinum coated quartz crystal at different pH values (80°C , 0.1 wt.% NaCl, $p\text{CO}_2=0.53$ bar).

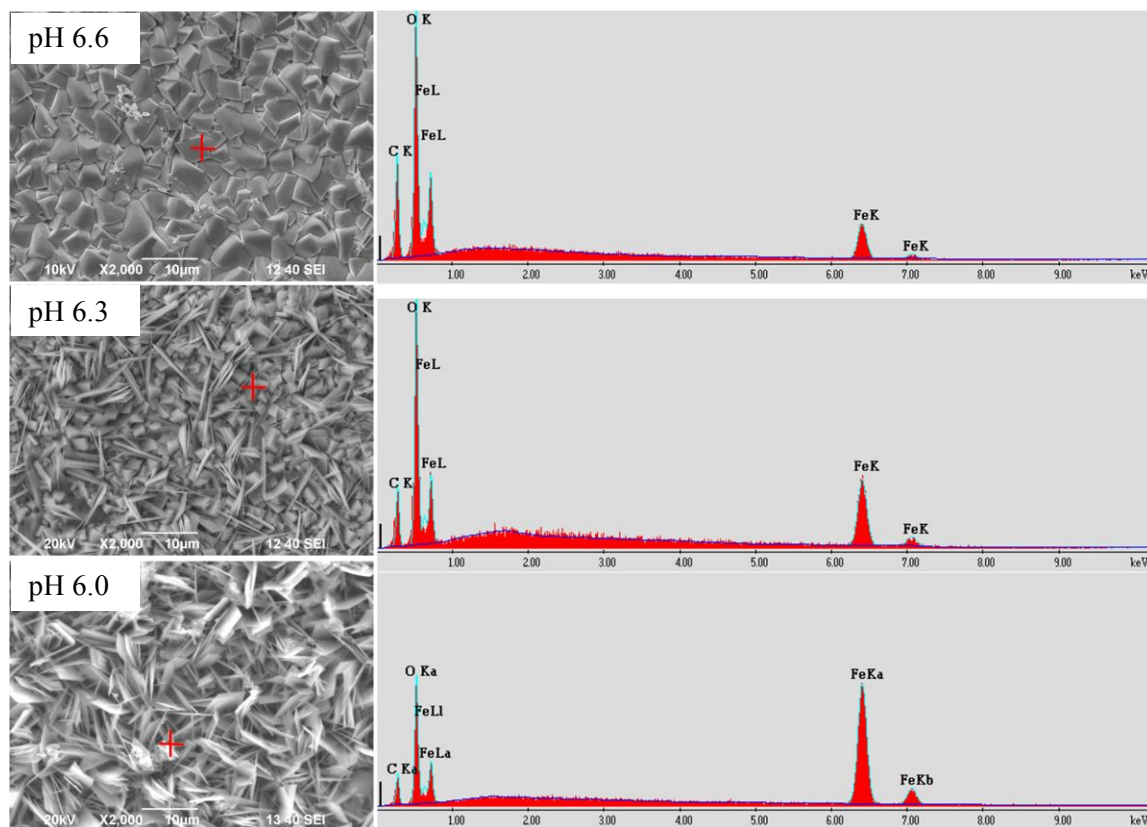


Figure 39. EDS analysis of iron carbonate layer formed on polarized (-700mV) platinum coated quartz crystal at different pH values (80°C, 0.1wt.% NaCl, $p\text{CO}_2=0.53$ bar).

These results match perfectly with the Raman spectroscopy and XPS analysis. Figure 40 and Figure 41 show the optical image and the Raman spectra for the three different pH values. A specific spot was selected for the optical image in the experimental data: prisms for pH 6.6 and 6.3, and plates for pH 6.0. The Raman spectra for those spots show two main vibrational modes at 292 and 1087 wavenumbers, which match the existing data in the literature for iron carbonate (siderite).

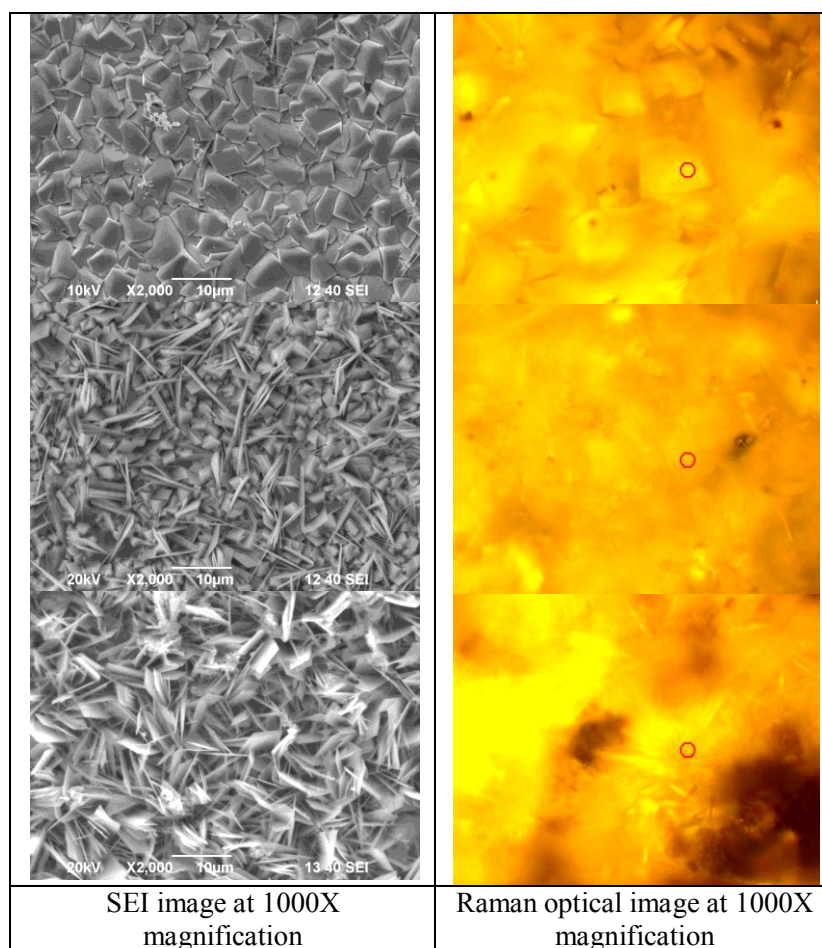


Figure 40. Raman optical image analysis of the iron carbonate layer formed on polarized (-700mV) platinum coated quartz crystal at different pH values (80°C, 0.1wt.% NaCl, and $p\text{CO}_2=0.53$ bar).

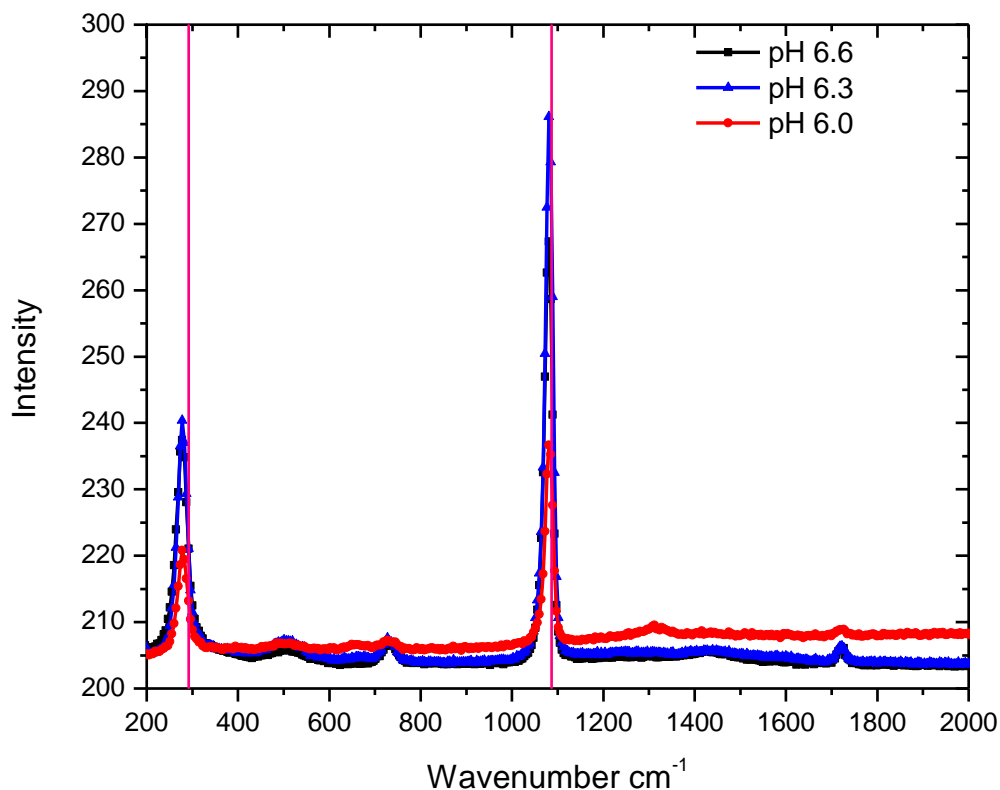


Figure 41. Raman spectra of the iron carbonate layer formed on polarized (-700mV) platinum coated quartz crystal at different pH values (80°C, 0.1wt.% NaCl, $p\text{CO}_2=0.53$ bar).

X-ray photoelectron spectroscopy (XPS) corroborates the composition of an iron carbonate layer on the platinum coated crystal (see Figure 42). The experimental results were compared with the binding energies reported by J. K. Heuer in 1999 [39]. Table 17 shows the comparison between the experimental results and the data reported in the literature by Heuer which again verifies the composition of the iron carbonate layer precipitated on the platinum coated crystal [39]. This leads to the first conclusion, that *while the morphology of the crystals appeared to be different at the three different pH values, the composition of the layer precipitated on the platinum coated crystal is the same - iron carbonate (siderite).*

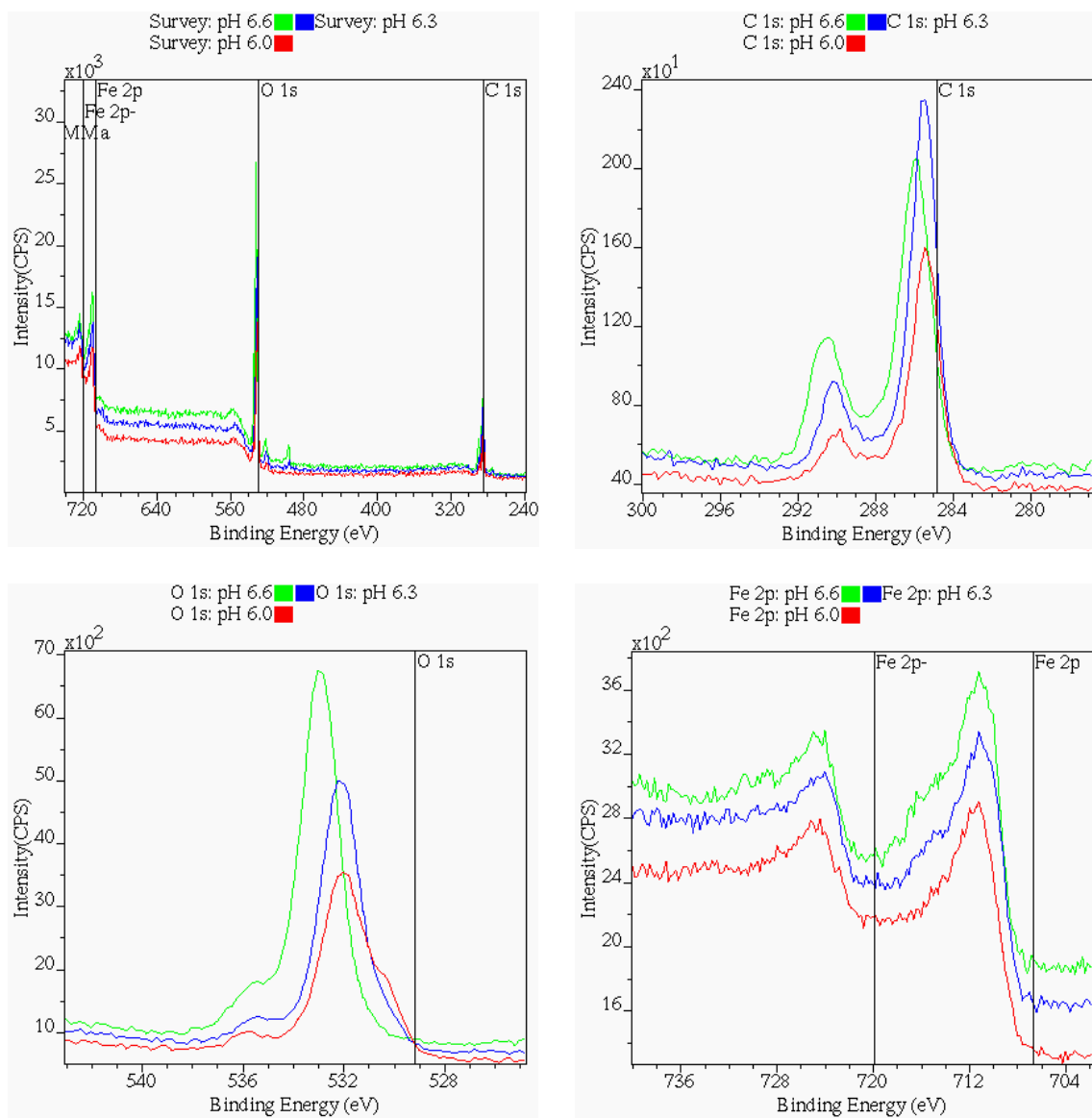


Figure 42. XPS scans of iron carbonate scale formed on polarized (-700mV) platinum coated quartz crystal at different pH values (80°C, 0.1 wt.% NaCl, and $p\text{CO}_2=0.53$ bar)

Table 17. Binding energies for FeCO₃[39]

	Theoretical data			
	C 1s	O 1s	Fe 2p _{3,2}	Fe 2p _{1/2}
	289.4	531.9	710.2	723.7
	Experimental data			
	C 1s	O 1s	Fe 2p _{3,2}	Fe 2p _{1/2}
pH 6.6	285.8	532.9	711.6	724.8
pH 6.3	285.7	532.0	710.9	724.5
pH 6.0	284.8	532.0	711.4	724.8

Since this research sought to identify the solubility of iron carbonate in the presence of acetic acid, it was necessary to focus the experimental conditions as shown in Table 18. Whereas previously the matrix allowed for three different measures of pH (see Table 14) similar results were obtained with respect to iron carbonate layer formation and only an initial pH 6.0 was used further (Table 18). An initial plan was to add acetic acid as a buffered solution in order to avoid a change in pH. The buffer solution is more effective when the pH to pK_a ratio is close to 1 [40]. However, it is also practical to use a pH range of approximately ± 1 with respect to the pK_a. Since the dissociation constant of acetic acid at 80°C is 4.86, it is better to work at an initial pH of 6.0 since this pH will decrease to around 5.4, in the range where the buffer solution is most effective. A large number of experiments were done in order to evaluate the reproducibility of the iron carbonate precipitation at pH 6.0, 80°C and 0.1 wt.% NaCl.

Table 18. Experimental conditions – Iron carbonate precipitation at pH 6.0

Test solution	Deionized water + 0.1wt.% NaCl
Test material	Platinum coated quartz crystal
Temperature	80°C
Total pressure of CO ₂	1 bar
Undissociated (free) organic acid	None
Initial pH	6.0
Rotation velocity	Static conditions

For the purpose of this study, three repeats of the same experiment were selected and labeled R1, R2 and R3. Figure 43 shows that the gain in mass for R1, R2 and R3 are very close to each other, approximately $1.5\text{mg}\cdot\text{cm}^{-2}$. The pH dropped to around 5.4 in all the experiments as a result of the iron carbonate precipitation. Consequently, the supersaturation (SS) of FeCO₃ also decreased. The SEM images for R1, R2 and R3 are mostly plates with a few prisms on the top of the plates (Figure 44). EDS analyses of the layer formed on a polarized platinum coated crystal confirm the presence of C, Fe and O constituent elements for the FeCO₃ as shown in Figure 45. XPS analyses corroborate this observation. Therefore, these experiments prove that is possible to successfully reproduce the iron carbonate precipitation on polarized platinum coated crystal, at the give conditions.

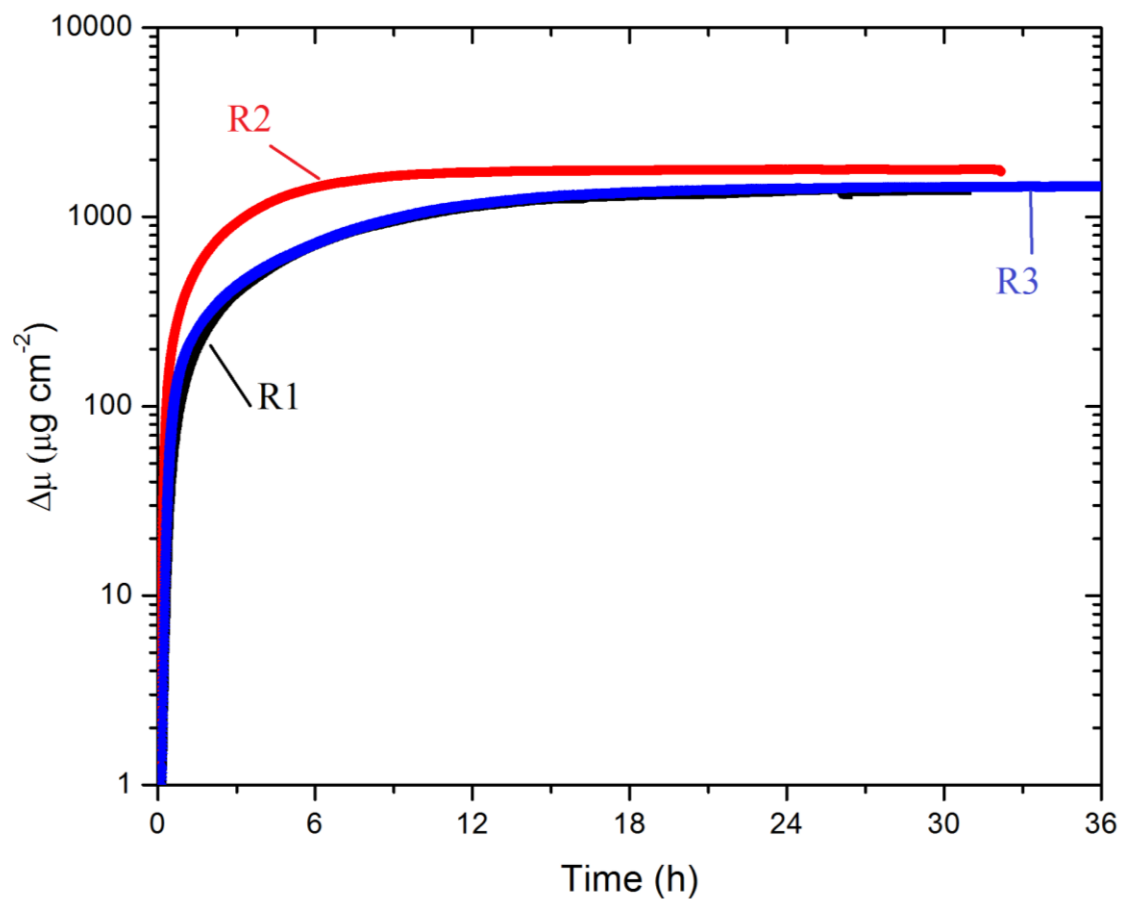


Figure 43. R1, R2 and R3 represent the reproducibility of the iron carbonate precipitation on polarized (-700mV) platinum coated quartz crystal at pH 6.0, 80°C, 0.1wt.% NaCl, and $p\text{CO}_2=0.53$ bar.

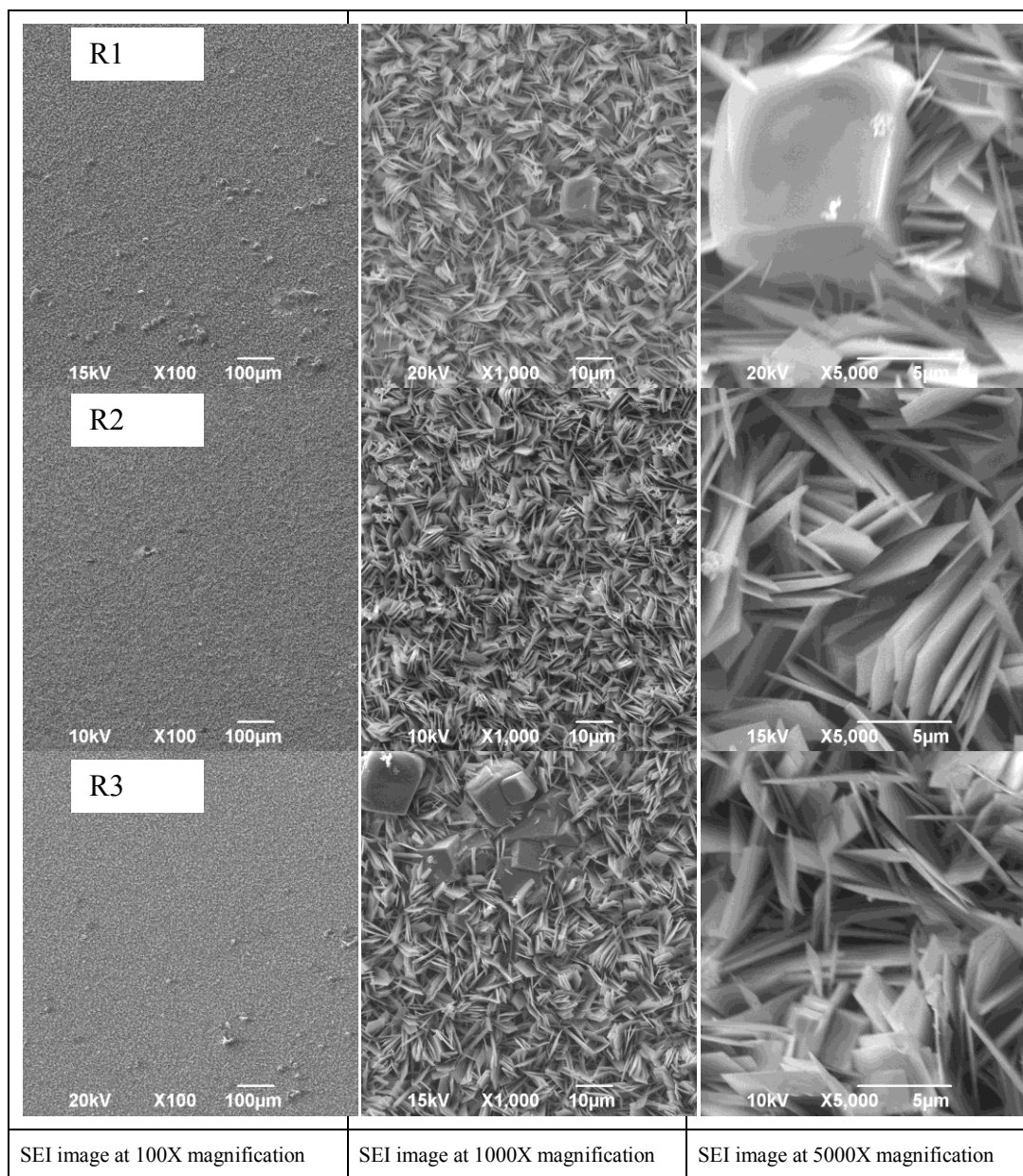


Figure 44. SEM image of iron carbonate layer formed on polarized (-700mV) platinum coated quartz crystal at pH 6.0, 80°C, 0.1wt.% NaCl, and $p\text{CO}_2=0.53$ bar.

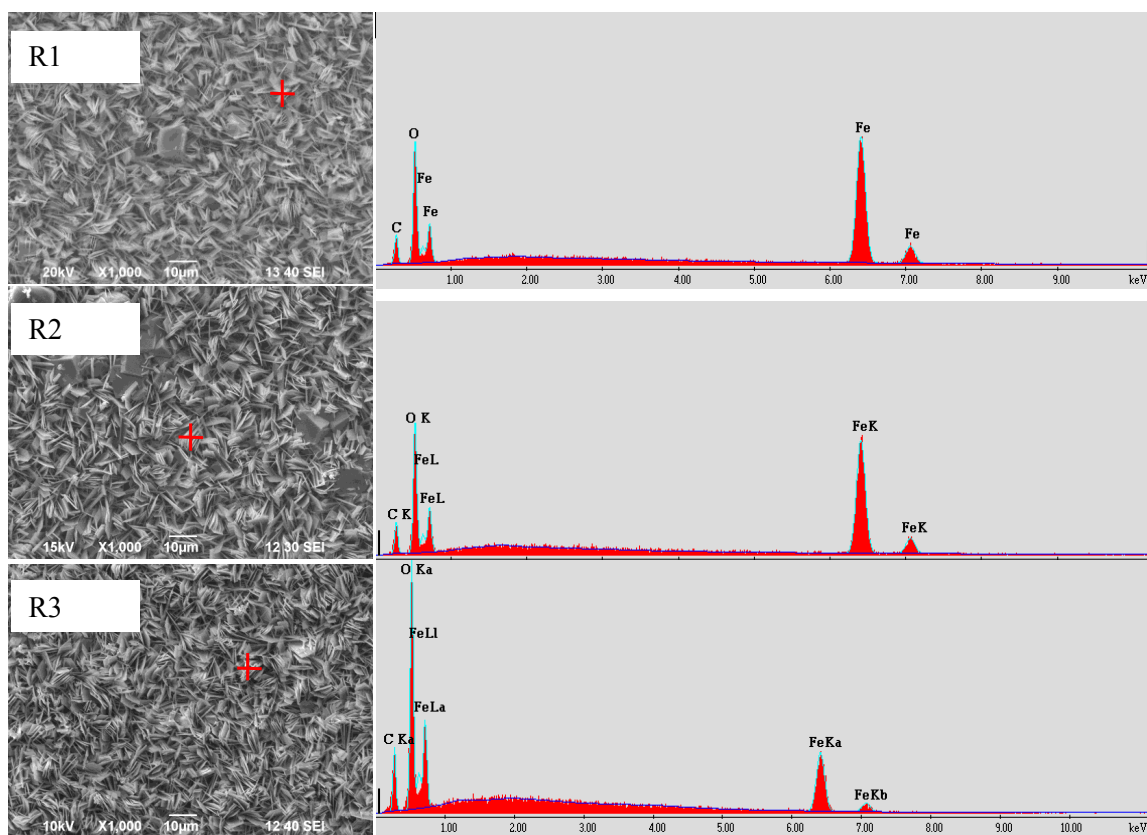


Figure 45. EDS analysis of iron carbonate layer formed on polarized (-700mV) platinum coated quartz crystal at pH 6.0, 80°C, 0.1wt.% NaCl, and $p\text{CO}_2=0.53$ bar.

5.4.2. Iron carbonate dissolution by acetic acid

The electrochemical quartz crystal microbalance (EQCM) was used to evaluate the dissolution of iron carbonate due to the presence of different concentrations of undissociated buffered acetic acid solution at 80°C, an initial pH 6.0, 0.1wt.% NaCl, initial SS of 200 and $p\text{CO}_2=0.53$ bar. The results in Figure 46 showed that the presence of acetic acid at a constant pH partially dissolved the iron carbonate, as indicated by a decrease in the mass of the FeCO_3 . The vertical lines show the period of time during which the designated amount of acid was added into the solution.

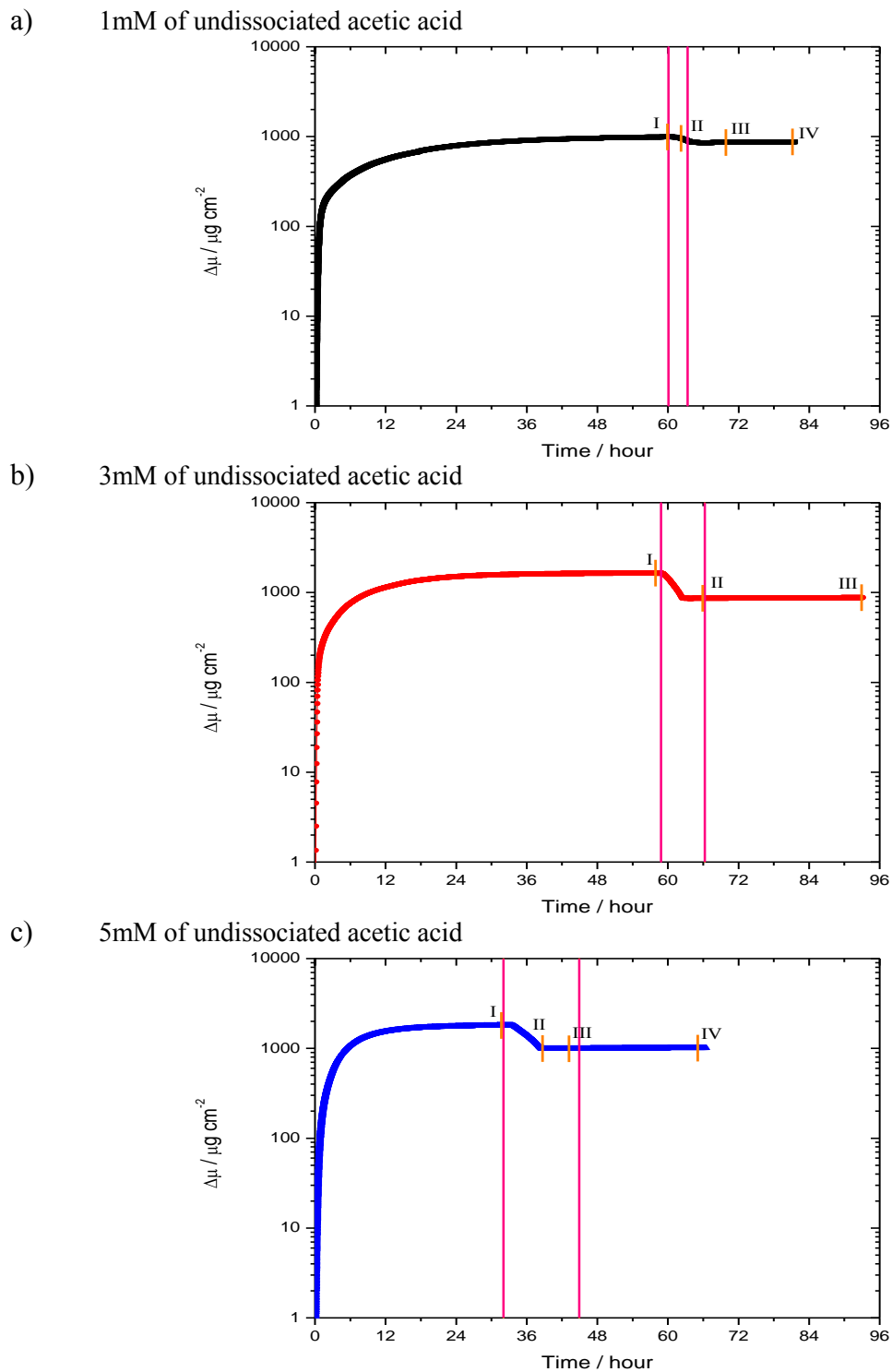


Figure 46. Iron carbonate precipitation-dissolution on polarized (-700mV) platinum coated quartz crystal at different undissociated acetic acid concentrations (80°C, 0.1wt.% NaCl, $p\text{CO}_2=0.53$ bar).

Table 19 shows the change in mass per unit area (Δm), pH, iron concentration (Fe^{2+}), and supersaturation (SS) at points I, II, III, and IV for each graph a, b, and c.

Table 19. Experimental results of the iron carbonate dissolution in the presence of different concentrations of acetic acid

1mM of undissociated acetic acid				
Period of time	Δm ($\mu\text{g cm}^{-2}$)	pH	Fe^{2+} (ppm)	SS
I	989	5.41	343	13
II	955	5.29	355	9.16
III	859	5.25	294	6.32
IV	873	5.21	392	7
3mM of undissociated acetic acid				
Period of time	Δm ($\mu\text{g cm}^{-2}$)	pH	Fe^{2+} (ppm)	SS
I	1639	5.37	347	11.1
II	866	5.20	291	4.6
III	875	5.17	270	3.9
5mM of undissociated acetic acid				
Period of time	Δm ($\mu\text{g cm}^{-2}$)	pH	Fe^{2+} (ppm)	SS
I	1797	5.40	284	10.5
II	994	5.13	308	3.6
III	991	5.14	341	4.2
IV	1006	5.09	290	2.9

The loss of iron carbonate at 1, 3 and 5mM was 11%, 46% and 44% respectively for the entire surface (Figure 47). The SEM shows that the FeCO_3 plates that initially formed on the platinum quartz crystal dissolved, and only prisms remained (Figure 48). These prisms were not clearly visible in SEM following the iron carbonate precipitation at pH 6.0 (see Figure 48). This may have happened for two reasons: 1) the prisms were hidden amongst the plates or 2) Ostwald ripening occurred. If the first scenario is correct, it may follow that the plates (which are smaller crystals) are less stable and therefore more easily dissolved by the addition of the acetic acid, and the prisms are all that

remain. The second possibility, Ostwald ripening, goes a bit further and refers to a spontaneous process of crystal enlargement which occurs because smaller crystals are kinetically favored (nucleate more easily and are energetically less stable), while large crystals are thermodynamically favored (represent a lower energy state). Small crystals will attain a lower energy state if transformed into larger crystals [35]. This process could explain the presence of the prisms on the platinum coated crystal.

These two possibilities might explain why even though acid was still being added, there was a point at which the dissolution process stopped. It is possible that the acetic acid has a preference for certain crystal structures that it can more easily dissolve, as was reported for the case of calcium carbonate (CaCO_3). Since both, CaCO_3 and FeCO_3 , belong to the same family of carbonates the different rate of dissolution observed in varying CaCO_3 crystal structures can be generalized. For example, a pellet of CaCO_3 will easily dissolve in HCl as compared with a prism of CaCO_3 . So this may explain why the dissolution of mass discontinues in spite of the continued addition of the acetic acid as shown in Figure 46.

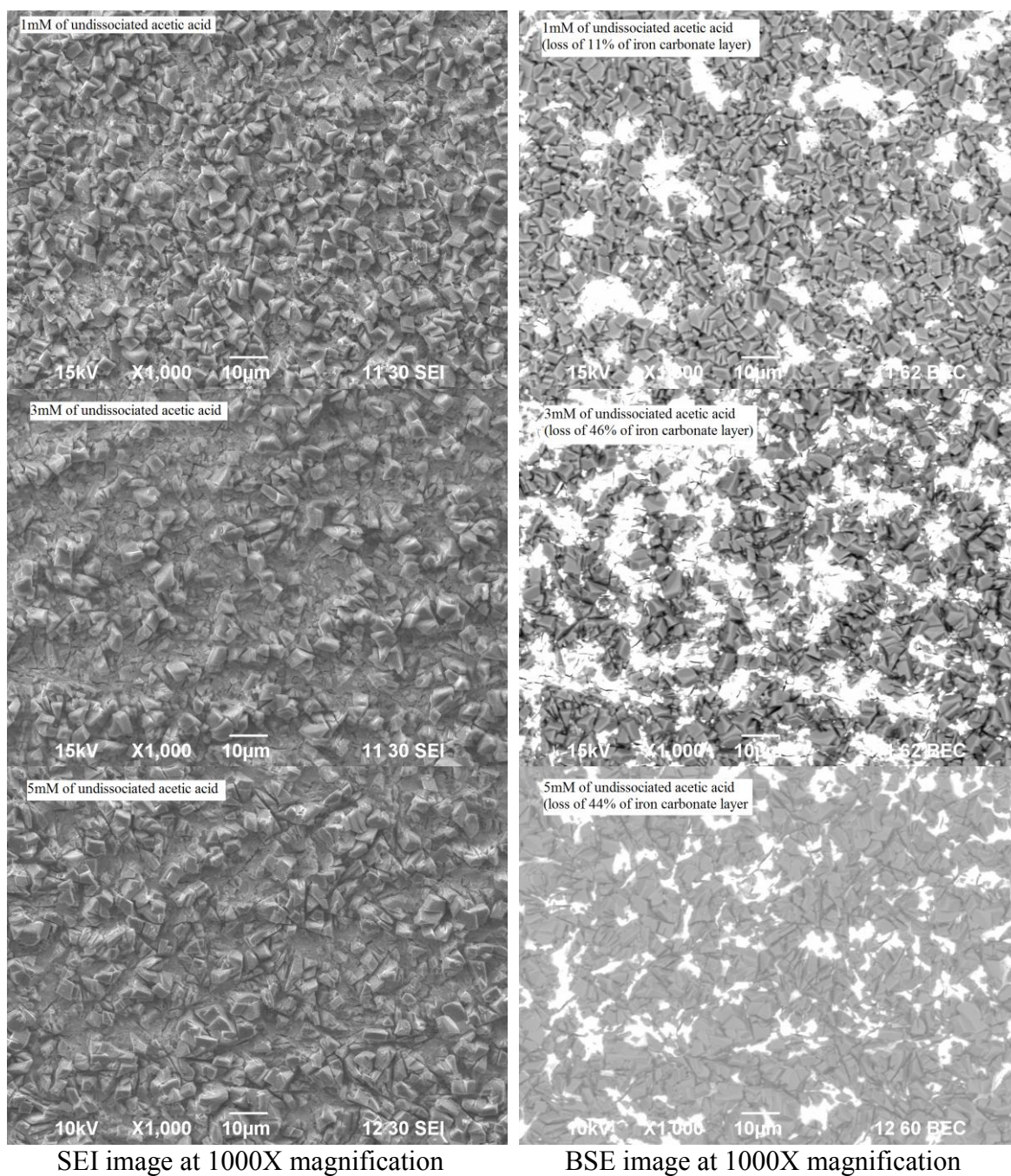


Figure 47. SEM image of iron carbonate dissolution due to the presence of acetic acid (pH 6.0, 80°C, 0.1wt.% NaCl, and $p\text{CO}_2=0.53$ bar).

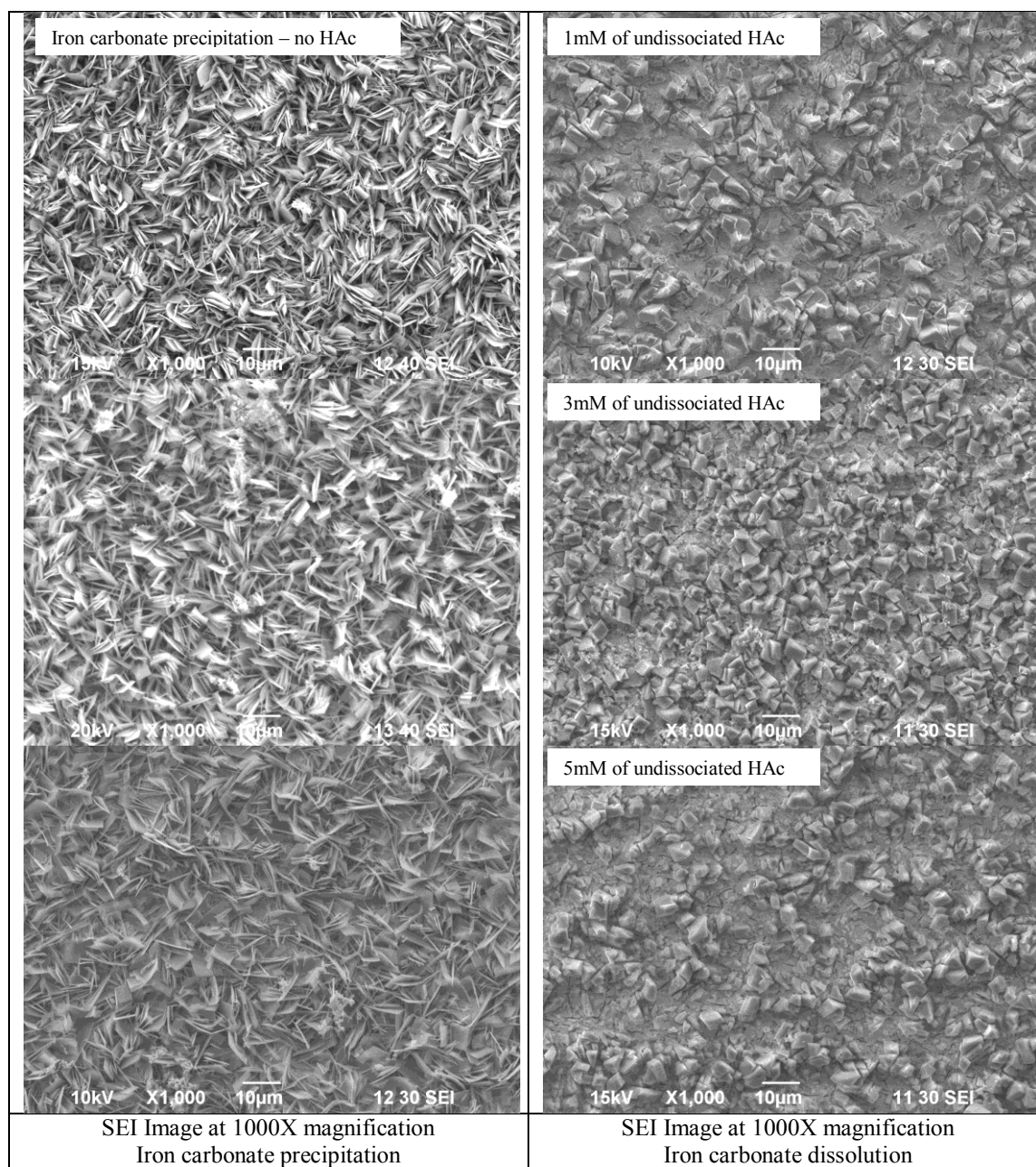


Figure 48. SEM image of iron carbonate precipitation and dissolution (pH 6.0, 80°C, 0.1wt.% NaCl, and $p\text{CO}_2=0.53$ bar).

As the addition of different amounts of acetic acid yielded similar results, the following discussion will use the 3mM addition as the representative of the three experiments. In Figure 49 it can be observed that the buffered acetic acid solution dissolves the iron carbonate layer in the first few hours, even when the acid is still being injected.

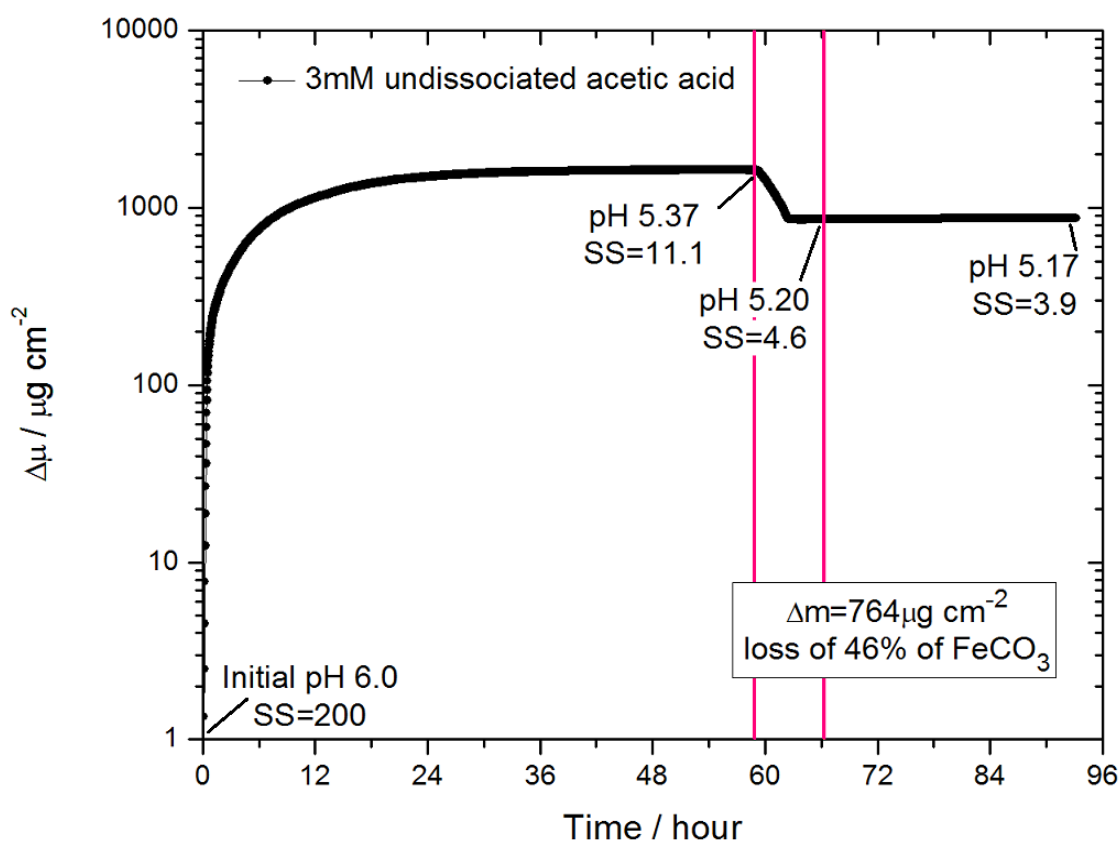


Figure 49. Iron carbonate precipitation on polarized (-700mV) platinum coated quartz crystal (3mM of undissociated acetic acid at 80°C, 0.1wt.% NaCl, and $p\text{CO}_2=0.52$ bar).

Energy-dispersive X-ray spectroscopy (EDS) analysis of the prisms shows that Fe, C, and O constitute the component elements for FeCO_3 . Further, analysis of the exposed area revealed the presence of platinum in addition to Fe, C, and O (Figure 50).

This means there is a thin layer formed on the exposed substrate, otherwise it would not be possible to see these peaks, even though the intensity is low compared to the prisms. The EDS reveals the presence of the platinum because the laser can easily penetrate the scale formed on the platinum coated crystal.

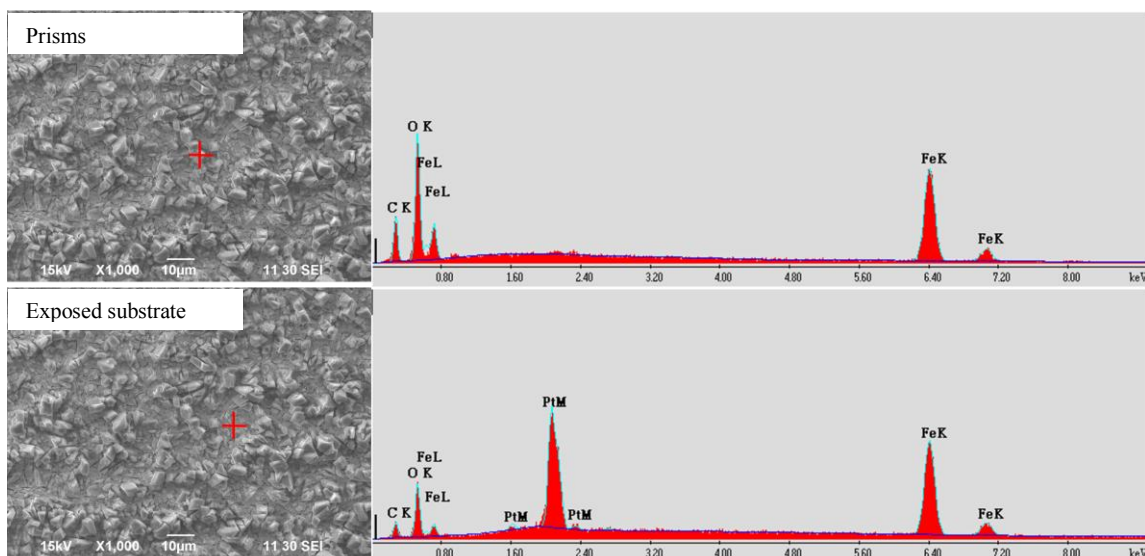


Figure 50. EDS analysis of iron carbonate layer formed on polarized (-700mV) platinum coated quartz crystal at pH 6.0, 80°C, 0.1wt.% NaCl, $p\text{CO}_2=0.53$ bar and 3mM of undissociated acetic acid.

The Raman spectra and optical image for 3mM of undissociated acetic acid is shown in Figure 51. Two areas were analyzed: the prisms and the exposed area. Both areas showed the main two peaks of iron carbonate. The surface analysis performed by Raman spectroscopy requires the presence of a dense corrosion product scale. As the vibrational spectrum of the substrate is dominant, Raman spectroscopy is an inappropriate method for analysis of the thin layer that remains after the addition of the buffered acetic acid solution.

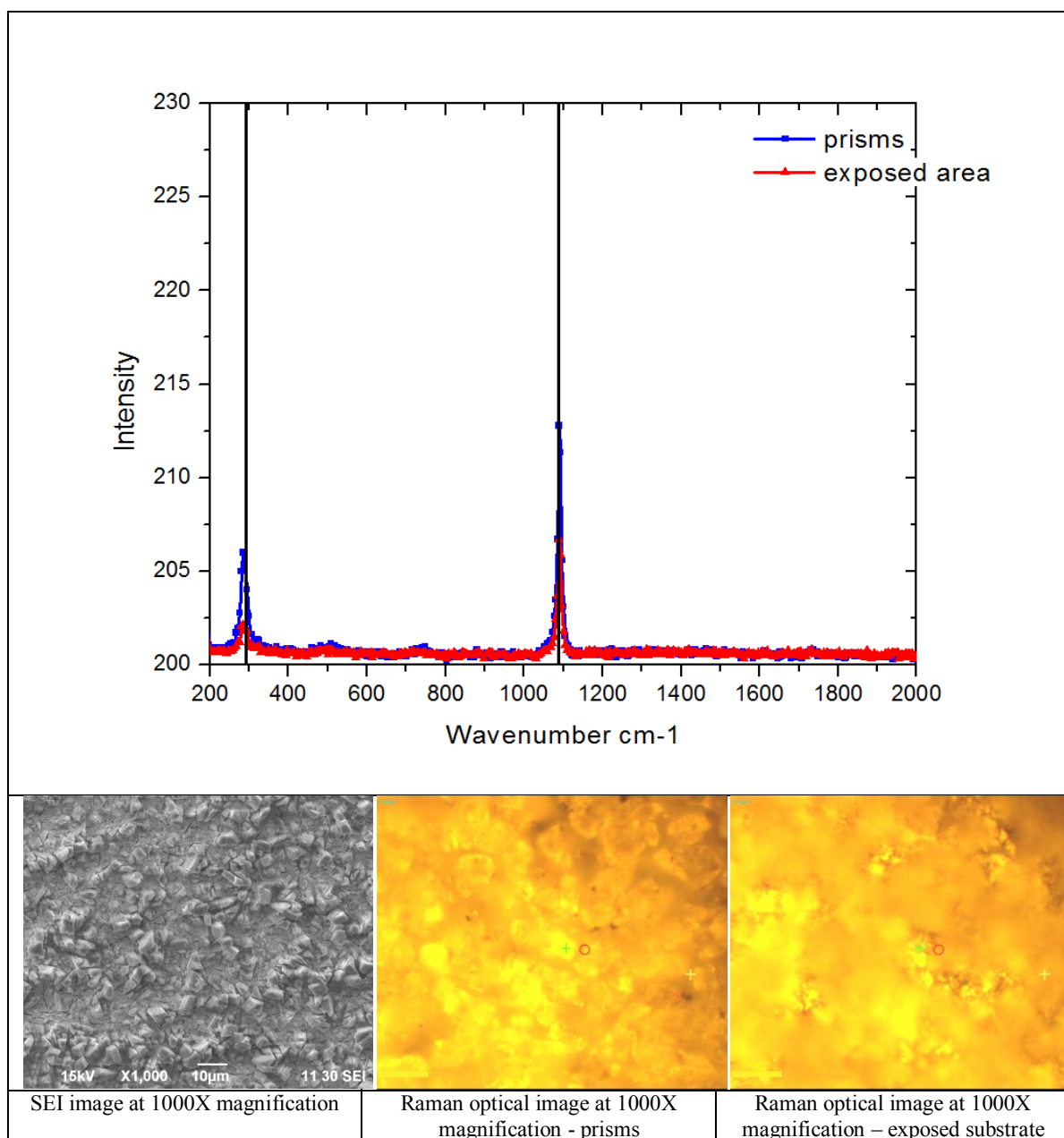


Figure 51. Raman spectra and optical image of the iron carbonate layer formed on polarized (-700mV) platinum coated quartz crystal at 80°C, 0.1wt.% NaCl, $p\text{CO}_2=0.53$ bar and 3mM of undissociated acetic acid.

X-ray photoelectron spectroscopy (XPS) scans of the iron carbonate layer formed on polarized (-700mV) platinum coated quartz crystal (80°C, 0.1wt.% NaCl, $p\text{CO}_2=0.53$ bar) were performed before and after the addition of 3mM of undissociated acetic acid as

shown in Figure 52. The results match the binding energies of FeCO_3 at 298.8 for C 1s, 532 for O 1s, 711 for Fe $2p_{3,2}$ and 724.8 for Fe $2p_{1/2}$. It was important to analyze the remaining prismatic crystals by different analytical technique to prove that FeCO_3 was the deposit (scale) formed on the platinum substrate. Since, the hexagonal crystals were not perfectly formed. TEM/EDS and electron diffraction pattern confirmed this assumption as shown in Figure 53 and Figure 54.

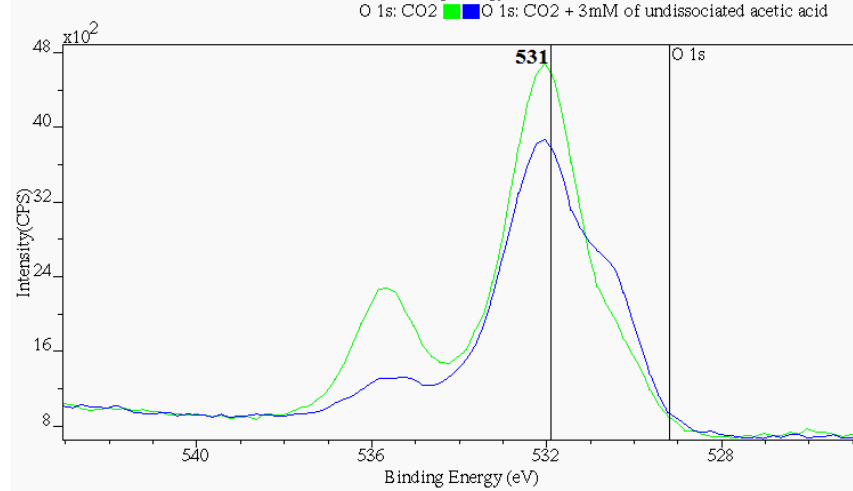
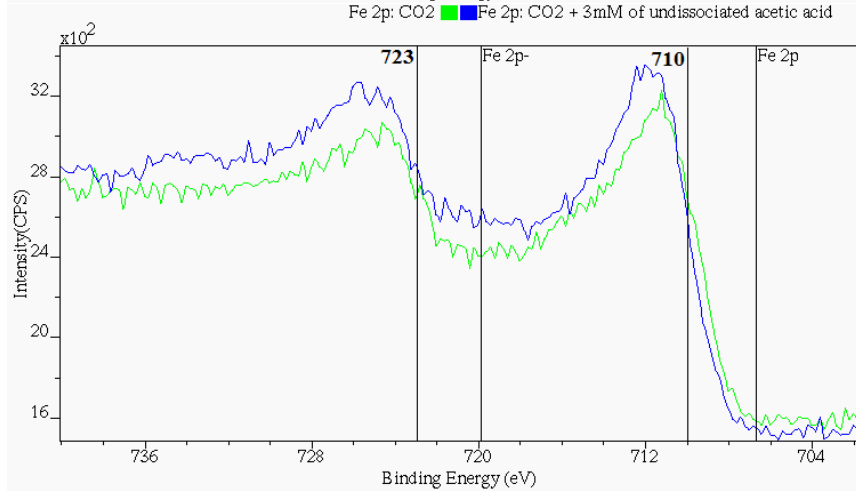
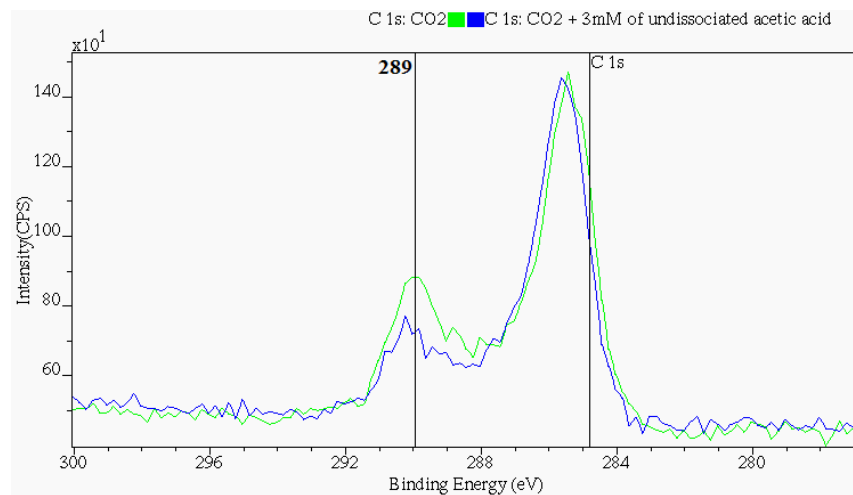
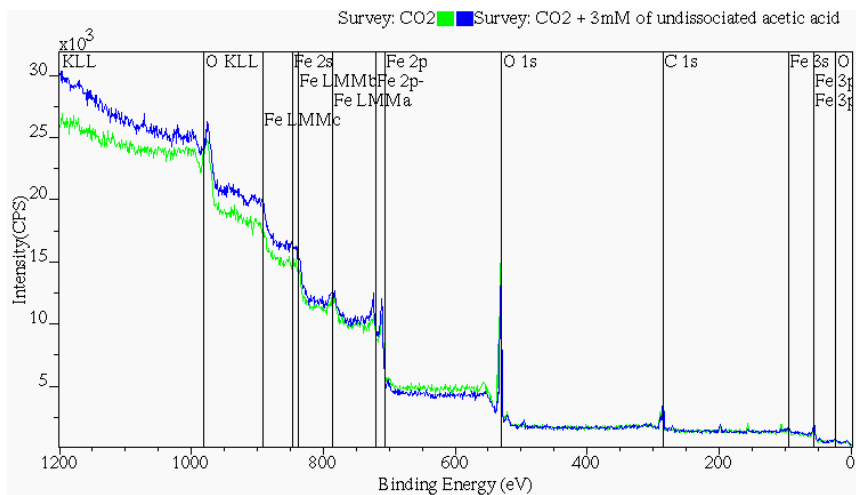


Figure 52. XPS scans of iron carbonate dissolution on polarized (-700mV) platinum coated quartz crystal in the presence of acetic acid (80°C, 0.1wt.% NaCl, and pCO₂=0.53 bar).

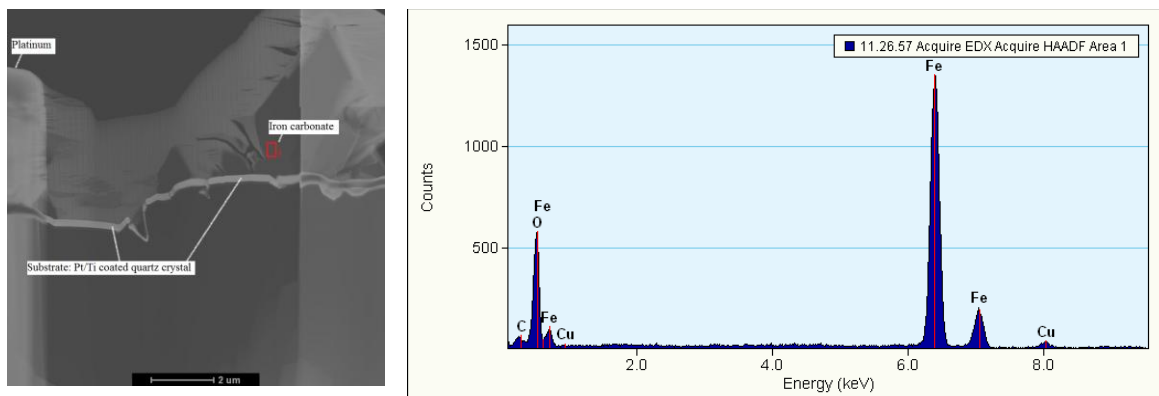


Figure 53. TEM image and EDS analysis of iron carbonate plates formed on polarized (-700mV) platinum coated quartz crystal in the presence of 3mM of undissociated acetic acid (80°C, 0.1wt.% NaCl, and $p\text{CO}_2=0.53$ bar).

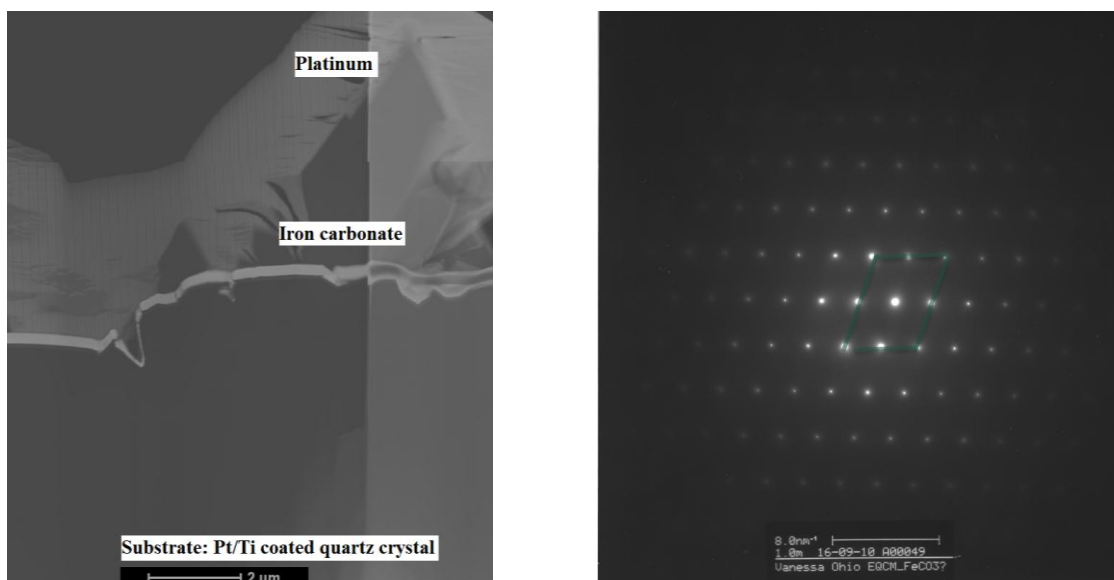


Figure 54. TEM image and ED data of the prisms found on polarized (-700mV) platinum coated quartz crystal in the presence of 3mM of undissociated acetic acid (80°C, 0.1wt.% NaCl, and $p\text{CO}_2=0.53$ bar).

5.4.3. Iron carbonate dissolution by hydrochloric acid

The previous experiments demonstrate that in most cases the pH drops approximately 0.3 pH units after the addition of the buffer acetic acid solution. This small decrease in pH may lead to a high corrosion rate in the field. Therefore, it is important to challenge the following hypothesis: *if the dissolution of the iron carbonate layer is a*

result of the small change in pH, then using hydrochloric acid instead of acetic acid would produce the same results. Figure 55 and Figure 56 shown that a small change in the acidity (HCl) influenced the iron carbonate removal very little as indicated by the change in mass from $1889 \mu\text{g}/\text{cm}^2$ to $1864 \mu\text{g}/\text{cm}^2$. The SEM pictures do not show a major loss of FeCO_3 , thus corroborating the results from of the EQCM.

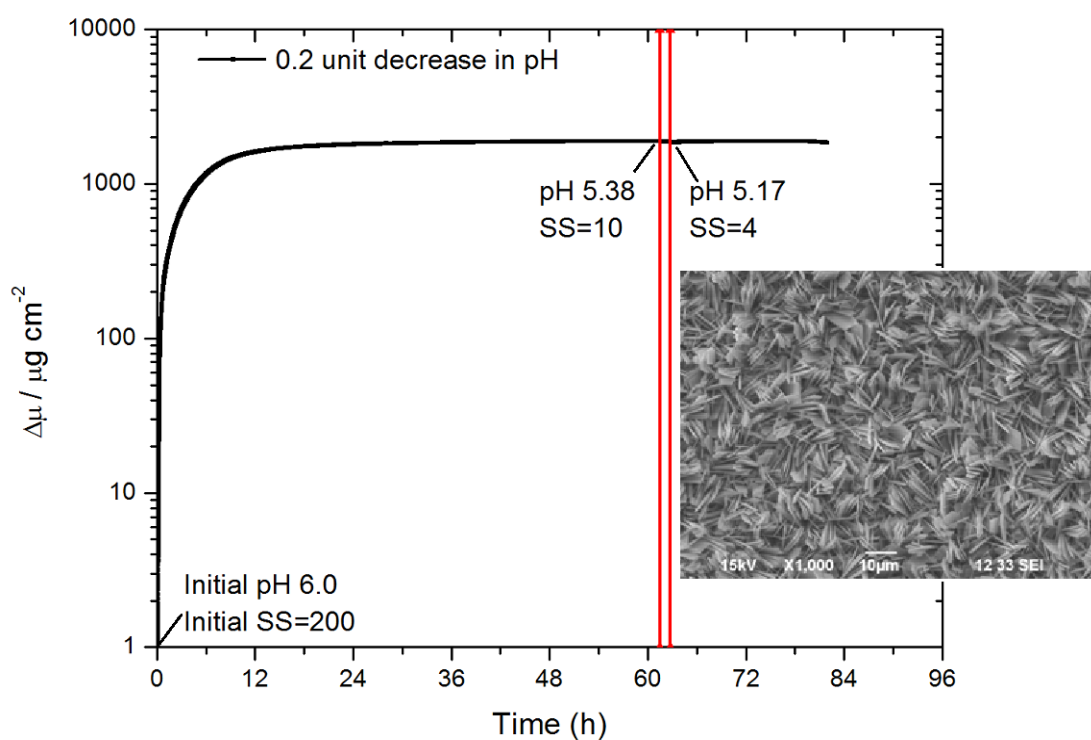


Figure 55. Iron carbonate layer dissolution with 0.1M of HCl (0.2 unit decrease in pH) at 80°C , 0.1wt.% NaCl, and $p\text{CO}_2=0.53$.

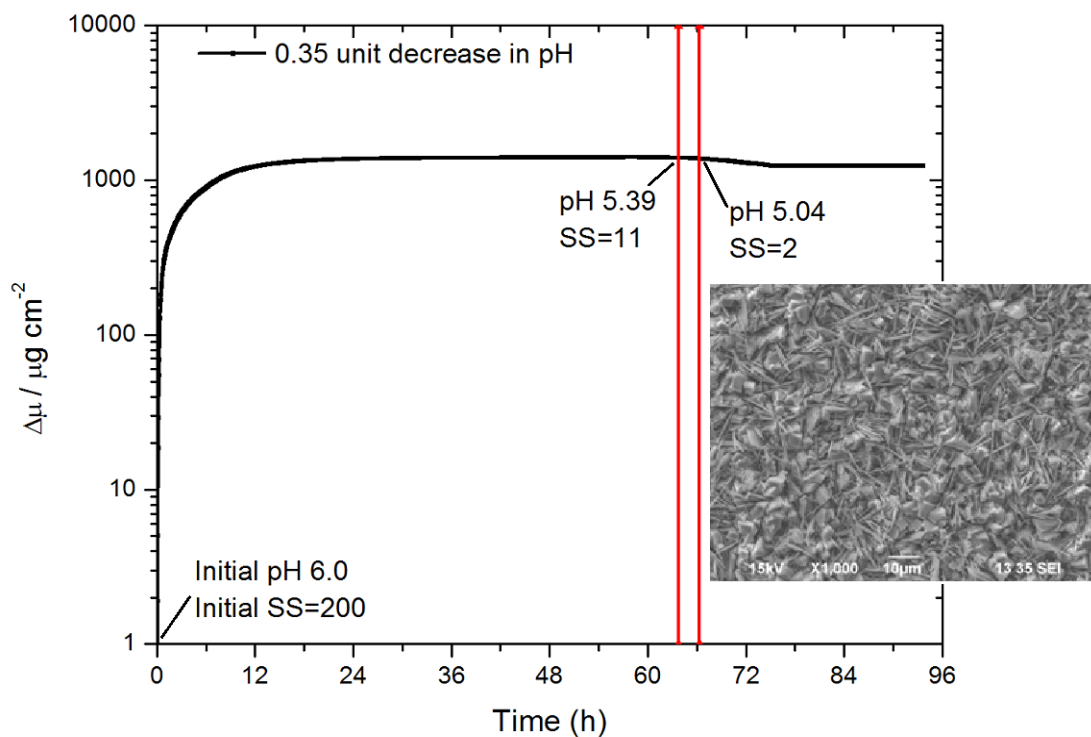


Figure 56. Iron carbonate layer dissolution with 0.1M of HCl (0.35 unit decrease in pH) at 80°C, 0.1wt.% NaCl, and $p\text{CO}_2=0.53$.

By comparing the SEM images of FeCO_3 dissolution with hydrochloric acid and acetic acid (Figure 57), the results show a greater loss of plates of iron carbonate when acetic acid was added.

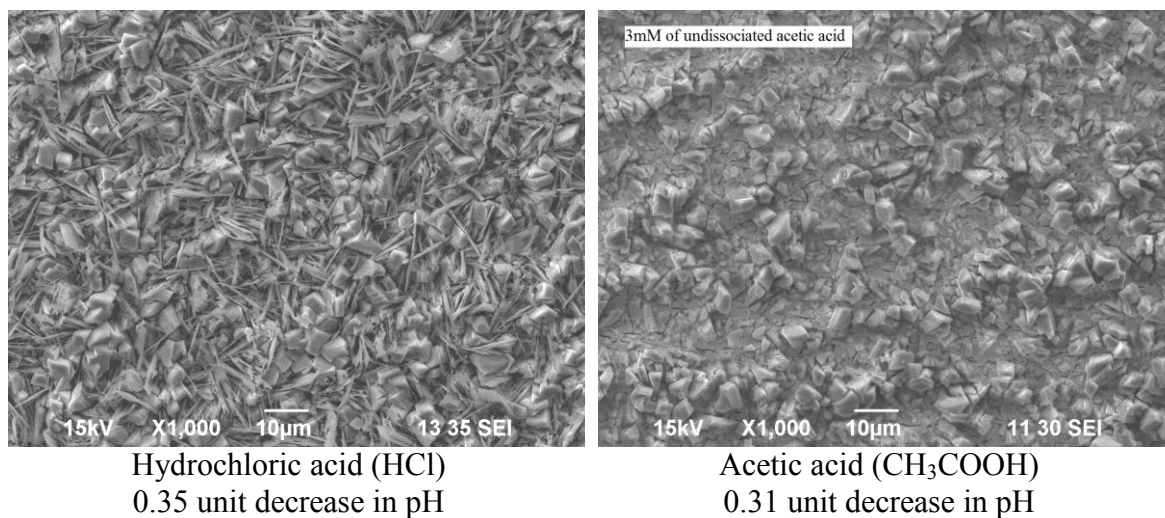


Figure 57. SEM image of the iron carbonate film dissolution with HCl and CH₃COOH (80°C, 0.1wt.% NaCl, and pCO₂=0.53).

5.5 Summary

It was shown that:

- The presence of acetic acid partially removed the iron carbonate layer on the platinum quartz crystal by selective dissolution.
- The dissolution of iron carbonate is not affected by a small change of pH (~0.4 units) under the tested conditions.

CHAPTER 6: CONCLUSIONS AND FUTURE WORK

6.1 Conclusions

Non-FeCO₃ layer forming conditions

- The presence of organic acids in CO₂ corrosion increased the corrosion rate due to an additional cathodic reaction—direct reduction of undissociated organic acid. The anodic reaction was mildly retarded.
- Under the same pH and concentration of undissociated organic acid, there is very little difference in electrochemical behavior of formic, acetic, and propionic acid.

Layer forming conditions

- The presence of acetic acid, at a constant pH, partially removed the iron carbonate layer, however, the corrosion protection was retained, because part of the FeCO₃ stayed attached to the steel surface. Several surface analysis methods have proven this assumption (SEM, EDS, XRD, XPS, FIB/TEM/EDS and ED data).
- No localized attack was found under the studied conditions.
- The electrochemical quartz crystal microbalance used to quantify the dissolution process confirmed that the presence of acetic acid was responsible for partial removal of the iron carbonate layer, corroborating the characterization data obtained by surface analysis.

6.2 Future work

In recent years, the deepwater portion of the Gulf of Mexico has shown a remarkable increase in oil and gas exploration, development and production, under increasingly severe conditions. Oilfield production worldwide constantly faces new challenges that need to be addressed for exploration and deepwater production, key factors that influence corrosion include flow rates, organic acid content, pH, souring, temperature, high pressures, etc.

A major change in the corrosion rate was seen with the combination of an increase in temperature and the presence of organic acids. a pure CO₂ corrosion rate increases by a factor of 2-3 over the same temperature range, while in the presence of organic acids the corrosion rate increased more than tenfold. This is despite the fact that some of the acid might have been lost to the gas phase by evaporation. The very different temperature sensitivity is indicative of a different corrosion mechanism which is due to the new cathodic reaction – the undissociated acid. This particular aspect of mild steel corrosion needs further investigation. The results will contribute to our overall understanding and ultimately to our ability to mitigate the severe corrosivity of such environments.

REFERENCES

- [1] Jones, D.A. *Principles and Prevention of Corrosion* .New Jersey:Upper Sanddle River, 1996, pp. 570.
- [2] Committee on Assessing Corrosion Education, National Research Council. *Assessment of Corrosion Education*.Washington DC:National Academic Press, 2009, .
- [3] Dugal, J.2010, "[Http://www.Drj.com/drworld/content/w2_028.Htm](http://www.Drj.com/drworld/content/w2_028.Htm)," Disaster Recovery Journal, 2010 (January/15) .
- [4] Anonymous 2010, "[Http://www.Bp.com/genericarticle.do?categoryId=2012968&contentId=7020563](http://www.Bp.com/genericarticle.do?categoryId=2012968&contentId=7020563)," 2010 (March/03) .
- [5] Dugstad, A., "The Importance of FeCO₃ Supersaturation on the CO₂ Corrosion of Carbon Steel."CORROSION/92, paper no.14. Houston, TX:NACE, 1992.
- [6] Van Hunnik, E. W., Pots, B. F., and Hendriksen, E., "The Formation of Protective FeCO₃ Corrosion Product Layers in CO₂ Corrosion."CORROSION/96, paper no.61. Houston, TX:NACE, 1996.
- [7] de Waard, C., and Milliams, D. E., "Carbon Acid Corrosion of Steel ." Corrosion Journal 35, 5(1975): p. 177.
- [8] de Waard, C., and Milliams, D. E., "Prediction of Carbonic Acid in Natural Gas Pipelines."First International Conference on the Internal and External Protection of Pipes/ 75, paper no.F1. Durham, UK.:University of Durham, 1975.
- [9] de Waard, C., and Lotz, U., "Prediction of CO₂ Corrosion of Carbon Steel."CORROSION/93, paper no.69. Houston, TX:NACE, 1993.

- [10] Gray, L., Anderson, B., Danysh, M., and Tremaine, R., "Mechanism of Carbon Steel Corrosion in Brines Containing Dissolved Carbon Dioxide at pH 4."CORROSION /89, paper no.464. Houston, TX:NACE, 1989.
- [11] Gray, L., Anderson, B., Danysh, M., and Trenaline, R., "Effect of pH and Temperature on the Mechanism of Carbon Steel Corrosion by Aqueous Carbon Dioxide."CORROSION/90, paper no.40. Houston, TX:NACE, 1990.
- [12] Nestic, S., Postlethwaite, J., and Olsen, S., "An Electrochemical Model for Prediction of Corrosion of Mild Steel in Aqueous Carbon Dioxide Solutions." Corrosion 52, 4(1996): p. 280-294.
- [13] Pots, B. F. M., "Mechanism Models for the Prediction of CO₂ Corrosion Rates Under Multi-Phase Flow Conditions."CORROSION/95, paper no.137. Houston, TX:NACE, 1995.
- [14] Videm, K., and Dugstad, A.1989, "Corrosion of Carbon Steel in an Aqueous Carbon Dioxide Environment Part 2: Film Formation," Materials Performance, 28 pp. 46.
- [15] Tomson, M. B., Rice, U., and Johnson, M. B., "How Ferrous Carbon Kinetics Impacts Oilfield Corrosion."International Symposium on Oilfield Chemistry, Anaheim CA, 1991, paper no.257. Anaheim, California:Society of Petroleum Engineers, 1991.
- [16] Dugstad, A., "Mechanism of Protective Film Formation During CO₂ Corrosion of Carbon Steel."CORROSION/ 98, paper no.31. Houston, TX:NACE, 1998.
- [17] Videm, K., and Dugstad, A., "Corrosion of Carbon Steel in an Aqueous Dioxide Environment." Materials Performance 28, (1989): p. 63.
- [18] Nestic, S., Nordsveen, M., Nyborg, R., "A Mechanistic Model for Carbon Dioxide Corrosion of Mild Steel in the Presence of Protective Iron Carbonate Films-Part 2: A Numerical Experiment." Corrosion 59, 6(2003): p. 489-497.

- [19] Crolet, J. L., and Bonis, M. R., "PH Measurements in Aqueous CO₂ Solutions Under High Pressure and Temperature." CORROSION 39, 2(1983): p. 39.
- [20] Barth, T."Organic and Inorganic Ions in Waters from Petroleum Reservoirs, Norwegian Continental Shelf: A Multivariate Statistical Analysis and Comparison with American Reservoir Formation Waters." Applied Geocemistry 6, (1991): p. 1-15.
- [21] Garber, J., Perkins, R., Jangama, V., and Alapati, R., "Calculation of Downhole pH and Delta pH in the Presence of CO₂ and Organic Acids."CORROSION/ 96, paper no.176. Houston, TX:NACE, 1996.
- [22] Bonis, M. R., and Crolet, J. L., "Basics of the Prediction of the Risk of CO₂ Corrosion in Oil and Gas Wells."CORROSION/89, Houston, TX:NACE, 1989.
- [23] Fajardo, V., Canto, C., Brown, B., and Nestic, S., "Effect of Organic Acids in CO₂ Corrosion."CORROSION/07, paper no.07319. Houston, TX:NACE, 2007.
- [24] Hedges, B., and McVeigh, L., "The Role of Acetate in CO₂ Corrosion: The Double Whammy."CORROSION/09, paper no.21. Houston, TX:NACE, 1999.
- [25] Crolet, J. L., and Bonis, M., "Why so Low Free Acetic Acid Thresholds in Sweet Corrosion at Low pCO₂?"CORROSION/05, paper no.5272. Houston, TX:NACE, 2005.
- [26] Crolet, J. L., Thevenot, N., and Dugstad, A., "Role of Free Acetic Acid an the CO₂ Corrosion of Steel."CORROSION, paper no.24. Houston, TX:NACE, 1999.
- [27] Gulbrandse, E., "Acetic Acid and Carbon Dioxide Corrosion of Carbon Steel Covered with Iron Carbonate."CORROSION/07, paper no.7322. Houston, TX:NACE, 2007.
- [28] Fajardo, V., Canto, C., Brown, B., and Nestic, S., "The Effect of Acetic Acid on the Integrity of Protective Iron Carbonate Layers in CO₂ Corrosion of Mild Steel."CORROSION/08, paper no.08333. Houston, TX:NACE, 2008.

- [29] Han, J., Yang, Y., Brown, B., and Nescic, S., "Electrochemical Investigation of Localized CO₂ Corrosion on Mild Steel."CORROSION/07, paper no.07323. Houston, TX:NACE, 2007.
- [30] Han, J., Yang, Y., Nescic, S., and Brown, B., "Roles of Passivation and Galvanic Effects in Localized CO₂ Corrosion of Mild Steel."CORROSION/08, paper no.8332. Houston, TX:NACE, 2008.
- [31] Perry, R.H., and Green, D., *Perry's Chemical Engineers' Handbook*. New York, NY: McGraw Hill, 1997, , Chap. 2, pp. 2-28 to 2-52.
- [32] Dean, J.A., *Lange's Handbook of Chemistry*. New York, NY: McGraw Hill, 1973, pp. p.1.15-p.8.48.
- [33] Nafday, O., and Nescic, S., "Iron Carbonate Scale Formation and CO₂ Corrosion in the Presence of Acetic Acid."CORROSION/05, paper no.5295. Houston, TX:NACE, 2005.
- [34] Bloss, D.F. *Crystallography and Crystal Chemistry an Introduction*.1st edition.United States:Holt, Rinehart and Winston, Inc, 1971, pp. 545.
- [35] West, A.R. *Solid State Chemistry and its Applications*.10th edition.Great Britain:John Wiley & Sons, 1998, pp. 734.
- [36] Blake, R., Hessevick, E., Zoltai, T., "Refinement of the Hematite Structure." *The American Mineralogist* 51, (1966): p. 123-129.
- [37] Graf, L. D."Crystallographic Tables for the Rhombohedral Carbonates." *The American Mineralogist* 46, 1283(1961): p. 1313.
- [38] Wechsler, B. A., Lindsley, D. H., and Prewitt, C. T., "Crystal Structure and Cation Distribution in Titanomagnetites (Fe_{3-x}Ti_xO₄)." *American Mineralogist* 69, (1984): p. 754-770.

- [39] Heuer, J. K., and Stubbins, J. F., "An XPS Characterization of FeCO₃ Films from CO₂ Corrosion." *Corrosion Science* 41, 7(1999): p. 1231-1243.
- [40] Silberberg, M.S. *Chemistry the Molecular Nature of Matter and Change*. 4th edition. Ohio, USA: McGraw Hill, 2006, pp. 1088.
- [41] Oberndorfer, M., Thayer, K., and Kastenbauer, M., "Application Limits of Stainless Steels in the Petroleum Industry." *Materials and Corrosion-Werkstoffe Und Korrosion* 55, 3(2004): p. 174-180.
- [42] Wang, J. Q., Atrens, A., Cousens, D. R., "Microstructure of X52 and X65 Pipeline Steels." *Journal of Materials Science* 34, 8(1999): p. 1721-1728.
- [43] Wang, J., and Atrens, A., "Microstructure and Grain Boundary Microanalysis of X70 Pipeline Steel." *Journal of Materials Science* 38, 2(2003): p. 323-330.
- [44] American Petroleum Institute, *Specification for Line Pipe*. Washington, USA: American Petroleum Institute, 2010, pp. 153.
- [45] Brooks, R.C. *Principles of the Heat Treatment of Plain Carbon and Low Alloy Steels*. 1st edition. Ohio, United States of America: ASM International, 1996, pp. 490.
- [46] ASTM International, *Annual Book of ASTM Standards: Wear and Erosion; Metal Corrosion*. Pennsylvania, USA: ASTM international, 2004, , Chap. G 3-89, G 59-97, G 102, pp. 42-50,-240-243, 446-452.
- [47] Sun Y. "Localized CO₂ Corrosion in Horizontal Wet Gas Flow." Doctor of Philosophy (PhD), Ohio University, 2003.
- [48] Watts, J.F., and Wolstenholme, J., *An Introduction to Surface Analysis by XPS and AES*. 1st edition. Chichester, England: Wiley, 2003, pp. 212.

[49] Chastain, J., and King, R.C.J., *Handbook of X-Ray Photoelectron Spectroscopy. A Reference Book of Standard Spectra for Identification and Interpretation of XPS Data* . Minnesota, United States of America: Physical Electronics Inc., 1995, , Chap. chapters 1 & 7, pp. 10-85, 219-290.

[50] O'Connor, D.J., Sexton, B.A., and Smart, C.R., *Surface Analysis Methods in Materials*. Germany: Springer, second edition, 2003, pp. 200.

APPENDIX I: CHARACTERIZATION OF THE X65 STEEL

Due to their ductility and hardness, carbon steels nominated as API 5L X# are typical alloys used in pipelines for oil and gas transportation. The designation X corresponds to strong grade pipelines followed by the specified yield strength of the pipe steel (measured in ksi). When manufacturing API 5L grade steel, the following parameters must be considered for reliable prediction of the material's performance: service temperature, service pressure, maximum stress level, water composition (*e.g.* chloride content), CO₂ and H₂S partial pressure, process contaminants (*e.g.* oxygen) and chemicals added to optimize the oil and gas flow in the pipeline [41]. Table 20 shows the chemical composition of some these alloys.

Table 20. Chemical composition of X52[42], X65^{§§} and X70[43] pipeline steel

	Mean Chemical composition [wt.%]										
	C	Si	Mn	P	S	Al	Cr	Ni	Mo	Nb	Ti
X52	0.16	0.31	1.32	0.017	0.006	0.03	0.01	0.01		0.02	
X65	0.14	0.25	1.18	0.012	0.003	0.033	0.15	0.38	0.16	0.027	0.002
X70	0.06	0.24	1.5	0.015	0.008	0.036	0.01	0.01	0.013	0.06	0.02

The major difference between the alloys, aside from the alloy elements, is their mechanical properties as shown in Table 21.

Table 21. Mechanical properties [44]

	Yield strength		Tensile strength	
	(ksi)	(MPa)	(ksi)	(MPa)
X52	52	358.52	66	455.05
X65	65	448.15	77	530.89
X70	70	482.63	82	565.37

^{§§} The chemical composition for X65 steel was done at the Laboratory Testing Inc. at Hatfield, PA

Each alloy undergoes a heat treatment to increase their strength and toughness with the metallurgical objective of achieving the finest possible grain size. The heat treatment is a hot thermo-mechanical process, followed by an accelerated cooling process. As the steel solidifies, it changes from austenite (γ) to ferrite (α). In this state, at just below the eutectoid temperature (723°C), the steel starts to nucleate and grow (Figure 58 and Figure 59). The final microstructure contains two phases, ferrite and cementite, organized in two micro-constituents, ferrite and pearlite. Pearlite is a lamellar mixture of ferrite and cementite.

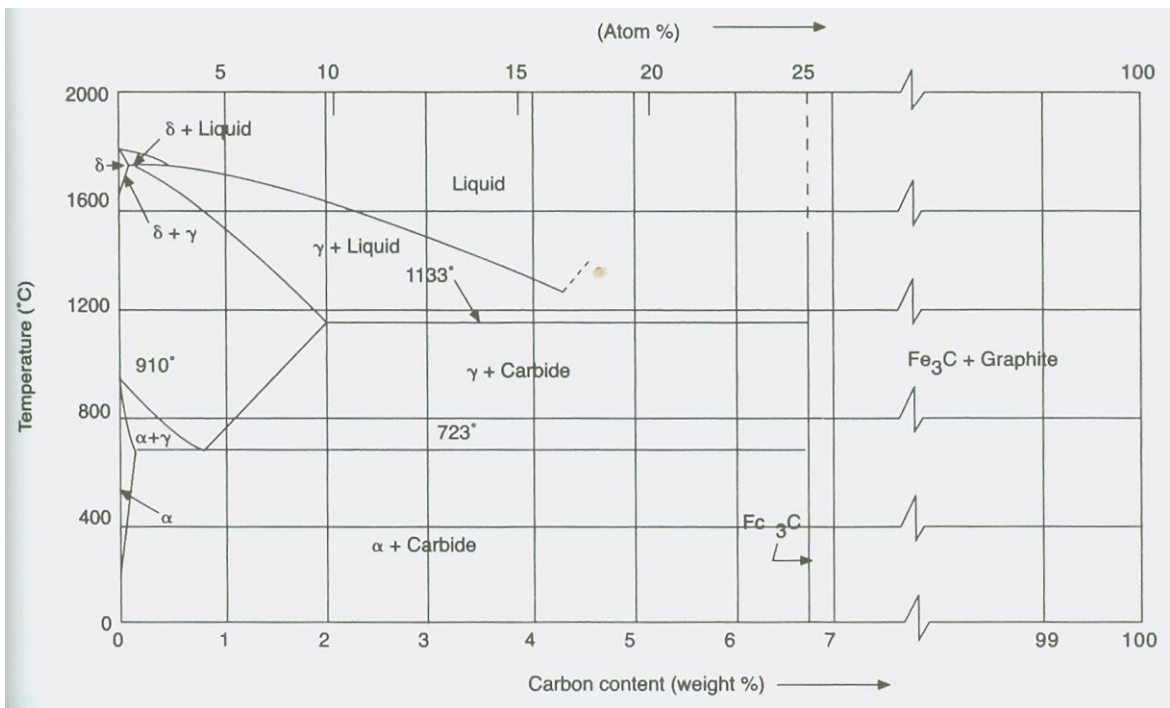


Figure 58. Iron-carbon phase diagram[45].

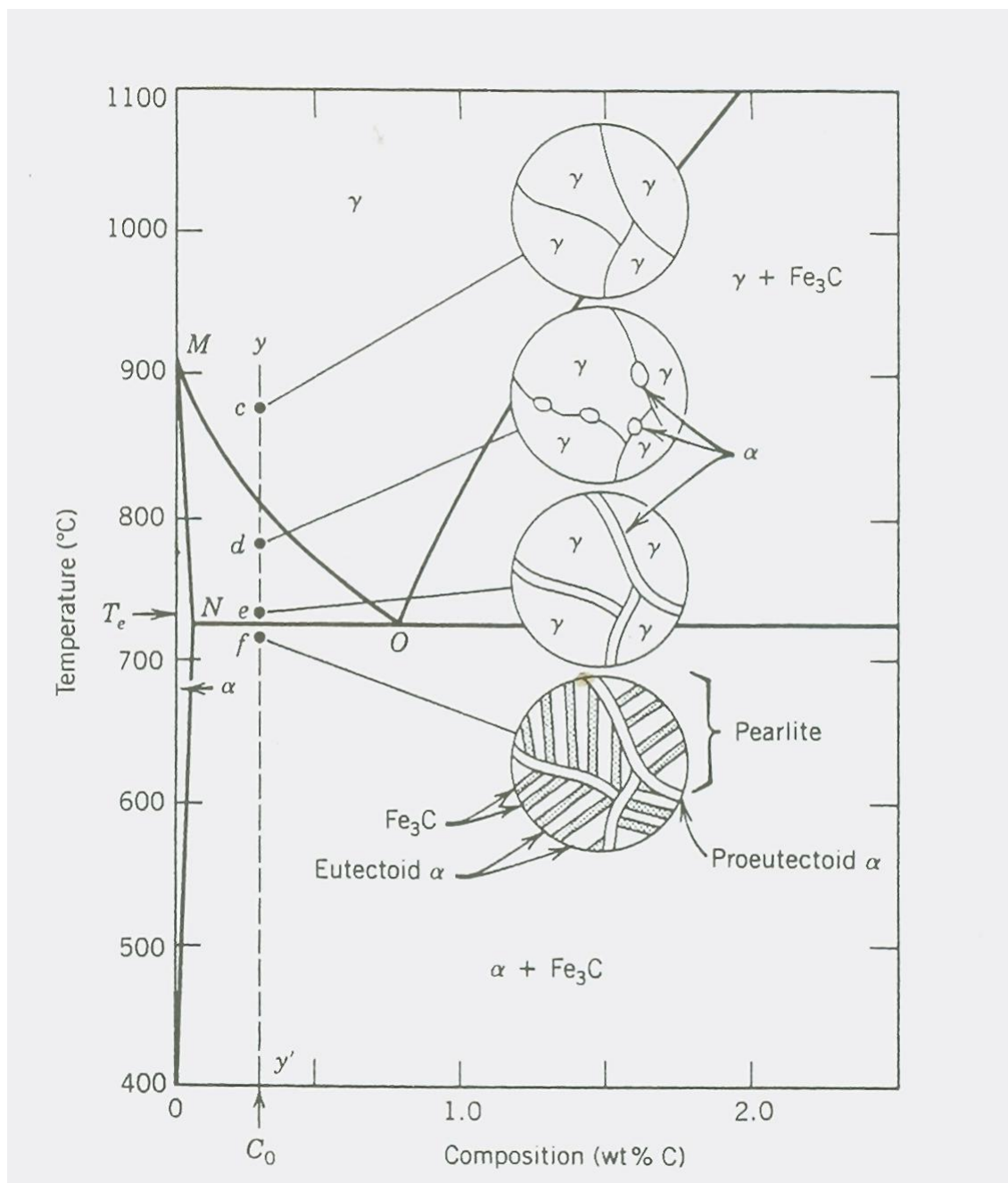


Figure 59. Depiction of the formation of proeutectoid or primary iron carbide from austenite upon cooling slowly a hypoeutectoid steel.

For the purpose of this study, X65 steel was used as a working electrode as it is one of the most common materials used in pipelines in the oilfield. This material meets the requirements of quality, low cost, and availability. X65 steel contains a minimum of 0.12wt.%C and, maximum of 0.16wt.%C making it a low carbon steel. According to the lever rule, the microstructural components in the equilibrium at 25°C for the X65 steel are ferrite-pearlite (as mentioned above). The percentages of the micro-constituents for the X65 steel are approximately 81% ferrite and 19% pearlite. The micrographic of the X65 steel etched with a 2% Nital solution shows a microstructure that corresponds to a proeutectoid of ferrite and pearlite (Figure 60).

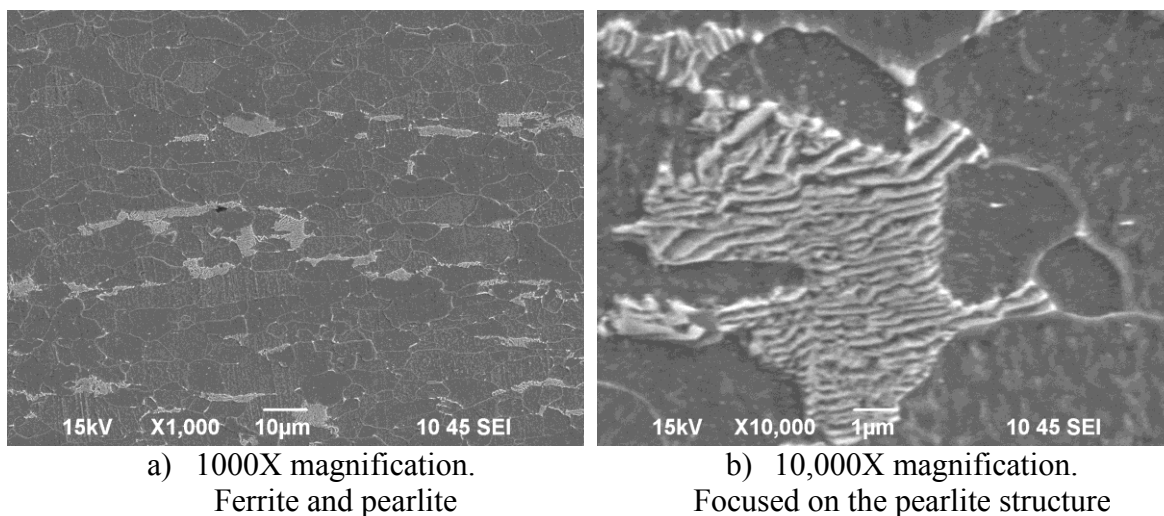


Figure 60. SEM image of the microstructure of X65 steel etched in 2% Nital solution.

APPENDIX II: CORROSION RATE DETERMINATION [46]

The corrosion rate of the steel can be experimentally determined using G 3-89, G3-59 and G3-121 of the ASTM standards, Vol.3 –Wear and Erosion; Metal Corrosion”. The ASTM standard G 3-89 describes the electrochemical measurements in corrosion studies based on current density-potential plots. In an electrochemical evaluation, a potential is applied to the working electrode and the perturbation in the current is recorded. In the resulting data, by convention, the current density is plotted on the abscissa, and the potential is plotted on the ordinate axis. Linear polarization plots are used for the determination of the polarization resistance (R_p). The R_p of a corroding electrode is the slope of a potential-current density plot at the corrosion potential (E_{corr}) in ohm-cm²:

$$\left[\frac{d(\Delta E)}{di} \right]_{\Delta E=0} = R_p \dots\dots\dots \text{Eq. (1)}$$

where ΔE is the potential difference of carbon steel ($E - E_{corr}$), and i is the current density (A/m²). The corrosion current density (i_{corr}) is related to the polarization resistance by the Stern-Geary coefficient (B) which relates the anodic and cathodic Tafel slopes (b_a and b_c respectively). The units of the Tafel slopes are V:

$$B = \frac{b_a b_c}{2.303(b_a + b_c)} \dots\dots\dots \text{Eq. (2)}$$

$$B = i_{corr} \cdot R_p \dots\dots\dots \text{Eq. (3)}$$

$$i_{corr} = \frac{B}{R_p} \dots\dots\dots \text{Eq. (4)}$$

The corrosion rate in millimeter per year (mm/y) can be determined from Eq. (5):

$$CR = 3.27 \times 10^{-3} \frac{i_{corr} EW}{\rho} \dots\dots\dots \text{Eq. (5)}$$

where EW and ρ are the equivalent weight (g) and density (g/cm^3) of the corroding material.

Uncertainty of the corrosion rate measurement

In the series of tests performed in this project there was numerous parameters that contributed to the overall corrosion rate. Some of these are: the type of material, the surface preparation, the aqueous chemistry, temperature, pH, partial pressure of carbon dioxide, and corrosion products.

The corrosion rate was obtained by linear polarization resistance (LPR). The accurateness measurement of LPR is directly affected by the applied potential, applied current, temperature and surface area of the working electrode. Following a propagation of error analysis for LPR measurements of the corrosion rate as presented by Sun [47] it has been found than the major source of uncertainty are the potential measurements. They lead to approximately $\pm 30\%$ error in the CR measurements.

Small changes in other parameters such as: the type of material, the surface preparation, the aqueous chemistry, pH, partial pressure of carbon dioxide, and effect of corrosion products may make the error in the CR measurements even larger, however this is hard to quantify directly.

APPENDIX III: SURFACE ANALYSIS

The characterization of the surface scale was performed using different analytical techniques, as shown in Table 22.

Table 22. Information provided from diverse analytical techniques

Technique	Information provided
Scanning electron microscope (SEM)	Provides the morphology of the scale formed on the solid surface.
Energy-dispersive X-ray spectroscopy (EDS or EDX)	Gives a semi-quantitative elemental analysis of a particular region of the surface. The depth of the analysis is 1 μ m [48].
X-ray diffraction (XRD)	The information acquired by XRD are the crystallographic structure, chemical composition, and physical properties of the material by comparing diffraction data against the International Centre for Diffraction Data (ICDD). The depth of the analysis is between 2-3 μ m.
X-ray photoelectron spectroscopy (XPS)	Allows a quantitative elemental analysis and identification of the chemical states of a solid surface, providing a unique spectrum (binding energy) of each element present on the surface. The depth of the analysis is ~1nm [49].
Raman spectroscopy	Identifies the phases formed on the steel by focusing on a small area. The depth of the analysis is 2 μ m -3mm.
Transmission electron microscopy (TEM)	Provides an image of the internal microstructure and crystal structure of a sample down to the crystal lattice, providing the diffraction data. This data can be compared with the ICDD to determine the composition of the molecule or element [50].

A multi-pronged analytical approach is the combination of all of the above techniques to provide a more complete understanding of the metal's surface.